Statistical Models to Describe Nuclear Matter at High Temperatures and Densities

Dawit Solomon Worku

Thesis Presented for the Degree of
DOCTOR OF PHILOSOPHY
in the Department of Physics
UNIVERSITY OF CAPE TOWN
December 2011

Abstract

In order to understand nuclear matter at high temperatures and densities formed in heavy ion collisions, it is useful to use statistical-thermal models to analyze the final state. We apply different types of statistical distributions and discuss their effects.

We discuss the hadron resonance gas model and its extension to include the Hagedorn spectrum [1, 2, 3]. The Hagedorn temperature, T_H is determined from the number of hadronic resonances including all mesons and baryons. This leads to the result $T_H = 174 \pm 11$ MeV consistent with the critical and the chemical freeze-out temperatures at zero chemical potential. We apply this result to calculate the speed of sound and other thermodynamic quantities in the resonance hadron gas model for a wide range of baryon chemical potentials using the chemical freeze-out curve [4, 5]. We compare some of our results to those obtained previously [6, 7].

We have also made additions to THERMUS [8] by including charm and bottom hadrons from the particle data table [9]. Then, we analyze and discuss the hadronic abundances measured in proton-proton (p-p), gold-gold (Au-Au) and lead-lead (Pb-Pb) collisions at Relativistic Heavy-Ion Collider (RHIC) [10] and Large Hadron Collider (LHC) [11, 12, 13] experiments using THERMUS. The THERMUS results obtained with the 2002 particle data table and new particle data table (2008 particle data table) and their differences are discussed. In particular, the data from the RHIC experiment for Au-Au collisions at 130 GeV and 200 GeV [10] are discussed and analyzed. Similarly, using the preliminary particle yield results of p-p collisions at 0.9 TeV and 7 TeV as well as Pb-Pb collision at 2.76 TeV [11, 12, 13] are presented and the thermodynamic parameters are obtained from the fit are discussed.

At last we discuss and apply the Tsallis distribution that has been used recently to fit the transverse momentum distributions of identified particles by the Solenoidal Tracker At RHIC (STAR) [14] and the Pioneering High Energy Nuclear Interaction eXperiment (PHENIX) [15] collaborations at the RHIC and by the A Large-Ion Collider Experiment (ALICE) [11] and Compact Muon Solenoid (CMS) [16] collaborations at the LHC. Theoretical issues are clarified concerning the thermodynamic consistency of the Tsallis distribution in the particular case of relativistic quantum distributions. Furthermore, an improved form is proposed for describing the transverse momentum distribution and fits are presented together with estimates of the parameter q, the temperature T and the fireball radius R[17, 18].

Finally, a part of the original results discussed in this thesis has been published before in [19, 17, 18].

Contents

1 Introduction 11

1.1 Historical Overview 11

1.2 Relativistic Heavy-Ion Collisions 13

1.2.1 Quarks 14

1.2.2 Hadrons 15

1.2.3 The QCD Phase Diagram 16

1.3 Thesis Scope 18

2 Thermodynamic quantities in the Extended Hadron Resonance Gas Model 20

2.1 Hagedorn's Conjecture 20

2.2 Motivation 24

2.3 The Hadron Resonance Gas Model and its Extension 25

2.4 Expression of thermodynamic quantities in EHRGM 27

2.4.1 Particle density and pressure 27

2.4.2 Energy and entropy densities and specific heat 28

2.5 Speed of Sound in relativistic fluid dynamics 29

2.5.1 The speed of sound at finite T and μ_B 34

2.6 Results using HRGM and EHRGM 42

2.7 Summary 52

3 Extensions of THERMUS 53

3.1 Review of THERMUS 53

3.2 The Statistical Formalism 55

3.3 Extended THERMUS Particle Set 58

3.4 How to use The Extended THERMUS? 61
3.5 Results and Discussions 62
3.5.1 Thermodynamic Parameters Analysis 63
3.6 Summary 70

4 Non-extensive Statistical Distribution 72
4.1 Theory of Non-extensive Statistics 73
4.2 Tsallis Distribution for Particle Multiplicities. 78
4.3 Thermodynamic Consistency 80
4.3.1 Quantum Statistics Form 82
4.3.2 Boltzmann Statistics Form 89
4.4 Tsallis Distribution and its Application 92
4.4.1 The Analytic Form of Transverse Momentum Spectrum 94
4.4.2 Transverse Momentum Spectrum Expansion in (q-1) . 95
4.4.3 Tsallis Fit Details 97

5 Conclusions 114

A Hadron mass spectrum data table 117

B Energy Density for a Hadron Gas 120

C Derivation of Non-extensive Formalisms 123
C.1 Tsallis Entropy 123
C.2 q-Exponential and q-Logarithm Functions 124

References 137

List of Figures

1.1 Sketch of the QCD phase diagram showing the critical point for the case of light and heavy quarks, a state of deconfined quarks and gluons may exist within neutron stars in the form of a color superconducting state, this figure taken from [20, 21]. 17

2.1 Cumulative number of hadronic resonances as a function of m. Again the hadronic data are made up of all resonances, including baryons, mesons and also heavy resonances made up of charm and bottom quarks, the list of hadron masses with their mass spectrum are given in the Appendix A. 22

2.2 Cumulative number of hadronic resonances as a function of m. The hadron data are included up to 2.0 GeV, including baryons and mesons from the fits of different authors, our fit is also shown here (dashed line). 25

2.3 (a) The energy density, ε, and pressure, P, in units of T^4 calculated using the HRGM as a function of the temperature T at $\mu_B = \mu_S = 0$ GeV. (b) The energy density, ε, and pressure, P, in units of T^4 for EHRGM as a function of the temperature scaled by the Hagedorn temperature T_H. 43

2.4 (a) The entropy density, s, in units of T^3 and interaction measure, $(\varepsilon - 3P)/T^4$ in units of T^4 calculated using the HRGM as a function of the temperature T at $\mu_B = \mu_S = 0$ GeV. (b) The entropy density, s, in units of T^3 and interaction measure, $(\varepsilon - 3P)/T^4$ in units of T^4 for EHRGM as a function of the temperature scaled by the Hagedorn temperature T_H 44

2.5 (a) The energy density TC_v/ε in units of ε calculated using the HRGM as a function of the temperature T at $\mu_B = \mu_S = 0$ GeV. (b) TC_v/ε in units of ε for EHRGM as a function of the temperature scaled by the Hagedorn temperature T_H 45
2.6 (a) The energy density, ε, and pressure, P, in units of T^4 calculated using the HRGM as a function of the temperature T for various μ_B and $\mu_S = 0$ GeV. (b) Energy density, ε, and pressure, P, in units of T^4 for EHRGM as a function of the temperature scaled by the Hagedorn temperature T_H 46
2.7 (a) The entropy, s, in units of T^3 and interaction measure, $(\varepsilon - 3P)/T^4$, calculated using the HRGM as a function of the T for various μ_B and $\mu_S = 0$ GeV. (b) The entropy, s, in units of T^3 and interaction measure, $(\varepsilon - 3P)/T^4$, using EHRGM as a function of the T. 46
2.8 (a) TC_v/ε calculated using the HRGM as a function of the temperature T for various value of μ_B and with $\mu_S = 0$ GeV. (b) TC_v/ε for the EHRGM as a function of the temperature scaled by the Hagedorn temperature T_H. 47
2.9 (a) The energy density, ε, and pressure, P, in units of T^4 calculated using the HRGM as a function of the temperature T for various value of μ_B and μ_S. (b) Energy density, ε, and pressure, P, in units of T^4 for EHRGM as a function of the temperature scaled by the Hagedorn temperature T_H 48
2.10 (a) The entropy density, s, in units of T^3 and variation measure, $(\varepsilon - 3P)/T^4$ calculated using the HRGM as a function of the temperature T for various μ_B and μ_S. (b) The entropy density, s, in units of T^3 and interaction measure, $(\varepsilon - 3P)/T^4$ in units of T^4 for EHRGM as a function of the temperature scaled by the Hagedorn temperature T_H 49
2.11 (a) TC_v/ε in units of ε calculated using the HRGM as a function of the temperature T for various μ_B and μ_S. (b) TC_v/ε in units of ε for EHRGM as a function of the temperature scaled by the Hagedorn temperature T_H 50

2.12 (a) Squared speed of sound $C_s^2(T, \mu)$ calculated using the HRGM as a function of the T with $\mu_B = \mu_S = 0$ GeV, for various value of μ_B but $\mu_S = 0$ GeV. (b) $C_s^2(T, \mu)$ in EHRGM with resonance mass truncated at $m < 2$ GeV. 50
2.13 (a) Squared speed of sound $C_s^2(T, \mu)$ calculated using the HRGM as a function of the T, for various value of μ_B and μ_S. (b) $C_s^2(T, \mu)$ in EHRGM with resonance mass truncated at $m <$ 2 GeV. 51

3.1 The number of states for hadron particle data table arranged in terms of their masses, included are baryons (red) and mesons (blue) with u, d and s quarks up to 2.6 GeV, $N(2600)^+$ `$THERMUS/particles/PartList_PPB2002.txt` [22]. 58
3.2 The number of states for particle data table arranged in terms of their masses. This is the updated THERMUS particle data table, it includes the c and b quarks up to 11.019 GeV, $\Upsilon(11020)^0$ `$THERMUS/extended_particles/PartList_PPB2008_CB.txt` (blue: mesons, red: baryons). 59
3.3 Logarithm of the number of states for particle data table which is found in `$THERMUS/particles/PartList_PPB2002.txt` [22] in terms of their masses. 60
3.4 Logarithm of the number of states for particle data tables which is found in `$THERMUS/extended_particles/PartList_PPB2008_CB.txt` in terms of their masses. 60
3.5 Figure (a) and (b) showing the comparison between rapidity densities in the combined fit and rapidity densities measured by STAR [10] for central Au-Au collision at 130 GeV and the corresponding thermal fit parameters are given for both particle data tables. Similarly, the comparison between rapidity densities in the combined fit and rapidity densities in terms of the residuals are presented for both particle data tables. . . . 64

3.6 Figure (a) and (b) showing the comparison between rapidity densities in the combined fit and rapidity densities measured by STAR [10] for central Au-Au collision at 200 GeV and the corresponding thermal fit parameters are given for both particle data tables. Similarly, the comparison between rapidity densities in the combined fit and rapidity densities in terms of the residuals are presented for both particle data tables. . . . 65
3.7 Particle yield results using the two particle data tables for the rapidity densities of the preliminary measured results from ALICE [11, 12, 13] for central p-p collision at 900 GeV. The thermal fit parameters are listed in Table 3.1. 67
3.8 Particle yield results for the two particle data tables for the rapidity densities of the preliminary results by ALICE [11, 12, 13] for central p-p collision at 7 TeV. The fit results were obtained from THERMUS 2002 and 2008 particle data tables. The thermal fit parameters are listed in Table 3.2. 68
3.9 Particle yield results using two particle data tables for the rapidity densities from ALICE in central Pb-Pb collision at 2.76 TeV [12, 13]. 69

4.1 $S_q(\{P_i\})$ for $W = 2$ and typical values of q (numbers on curves). 77
4.2 Comparison between the Boltzmann and Tsallis-B distribution as a function of the energy E, keeping the Tsallis parameter q fixed, for various values of the temperature T. The chemical potential is kept equal to one in all curves, the units are arbitrary. 80
4.3 Comparison between the Fermi-Dirac and Tsallis-FD distributions (A), Bose-Einstein and Tsallis-BE distributions (B) as a function of the energy E, keeping the Tsallis parameter q fixed, for various values of the temperature T. The chemical potential is kept equal to one in all curves, the units are arbitrary. 81

4.4 The calculated value of q, and temperature T in Au-Au collision at 200 GeV, for different hadron species. 98

4.5 The calculated values of the radius, R in Au-Au collision at 200 GeV for different hadron species. 99

4.6 The particle yield at mid-rapidity, dN/dy and the average transverse momentum, $\langle p_T \rangle$ for different hadron species. The results have been compared with STAR result [23]. 100

4.7 Comparison between the measured transverse momentum distribution for π^+ and π^-, K^+ and K^- as well as p and $\bar{p}$ measured by the STAR collaboration [23] in Au-Au collision at 200 GeV and the Tsallis-B distribution. The full and broken lines are fits using the parameterization Eq. (4.93) to the data with the parameters listed in table 4.1. 101

4.8 The calculated values of q and T in p-p collisions at 7 TeV and 900 GeV results for different hadron species. 102

4.9 The calculated value of the radius, R in p-p collisions at 900 GeV and 7 TeV, for different hadron species. 103

4.10 The particle yield at mid-rapidity, dN/dy and the average transverse momentum, $\langle p_T \rangle$ for different hadron species. 104

4.11 Comparison between the measured transverse momentum distribution for K^0_S and Λ as measured by the CMS collaboration [16] in p-p collision and the Tsallis-B distribution. The full and broken lines are fit using the parameterization Eq. (4.93) to the 7 TeV data while the dashed line is fit to the 0.9 TeV data with the parameters listed in Table 4.2. 104

4.12 Comparison between the measured transverse momentum distribution for Ξ^- as measured by the CMS collaboration [16] in p-p collision and the Tsallis-B distribution. The full line is a fit using the parameterization Eq. (4.93) to the 7 TeV data while the dashed line is a fit to the 0.9 TeV data with the parameters listed in Table 4.2. 105

4.13 Comparison between the measured transverse momentum distribution for π^+, K^+, p, π^-, K^- and $\bar{p}$ as measured by the ALICE collaboration [11] in p-p collision and the Tsallis-B distribution. The full line is a fit using the parameterization Eq. (4.93) to the 0.9 TeV data with the parameters listed in Table 4.2. 106

4.14 The calculated values for q and the temperature, T in Pb-Pb collision at 2.76 TeV results with different hadron species. . . 107

4.15 The calculated values for the radius, R in Pb-Pb collision at 2.76 TeV results with different hadron species. 108

4.16 The particle yield at mid-rapidity, dN/dy and the average transverse momentum, $\langle p_T \rangle$ with different hadron species. . . . 108

4.17 Comparison between the measured transverse momentum distribution for π^+ and π^- (left figure), K^+ and K^- (right figure) as measured by the ALICE collaboration [12] in Pb-Pb collision and the Tsallis-B distribution. The full and broken lines are a fit using the parameterization Eq. (4.93) to the 2.76 TeV data with the parameters listed in Table 4.3. 109

4.18 Comparison between the measured transverse momentum distribution for p and $\bar{p}$ as measured by the ALICE collaboration [12] in Pb-Pb collision and the Tsallis-B distribution. The full and broken lines are a fit using the parameterization Eq. (4.93) to the 2.76 TeV data with the parameters listed in Table 4.3. 109

4.19 Comparison between the measured transverse momentum distribution for $(K^+ + K^-)/2$ and K_s^0, p and Λ as measured by the ALICE collaboration [12] in Pb-Pb collision and the Tsallis-B distribution. The full and broken lines are a fit using the parameterization Eq. (4.93) to the 2.76 TeV data with the parameters listed in Table 4.3. 110

List of Tables

1.1 Properties of quarks. The charge is in units of the magnitude of the charge of an electron, 1.6×10^{-19} coulomb, spin is in units of $\hbar$. The top quark mass is deduced from experimental measurements of its decay dynamics (F - Flavor, M - Mass, Q - Electric Charge, B - Baryon number, I_3 - Isospin Spin, S - Strangeness, C - Charm, b - beauty and T - Top) [24]. 14

2.1 The result for the parameters c, m_0 and T_H using Eq. (2.1) and the hadron resonances listed in appendix A. 25

3.1 The predicted thermal fit parameters for p-p collision at 900 GeV on ALICE [11, 12, 13]. The fit results were obtained from both THERMUS particle data tables (where THERMUS 2002 particle data table, Fit (2002) and THERMUS 2008 particle data table, Fit (2008)). 68

3.2 The predicted thermal fit parameters for p-p collision at 7 TeV on ALICE [11, 12, 13]. The fit results were obtained from the two particle data tables. 69

3.3 The predicted thermal fit parameters for Pb-Pb collision at 2.76 TeV on ALICE [12, 13]. The fit results were obtained from both THERMUS particle data tables. 70

4.1 The calculated values of T and q for different hadron species measured by the STAR [23] in Au-Au collision at 200 GeV using the Tsallis-B form for the momentum distribution. . . . 98

4.2 The calculated values of the T and q for different hadron species measured by the ALICE [11] and CMS collaborations [16] in p-p collisions at 900 GeV and 7 TeV using the Tsallis-B form for the momentum distribution. 102
4.3 Fitted values of the T and q for different hadron species measured by the ALICE [11, 12, 13] in Pb-Pb collision at 2.76 TeV using the Tsallis-B form for the momentum distribution. . . . 107
4.4 The calculated values of χ^2/ndf with the Tsallis-B distribution for different hadron species in Au-Au collision at 200 GeV measured by the STAR collaboration [14]. 112
4.5 The comparison between the calculated values of χ^2/ndf using the Tsallis-B distribution with the CMS and ALICE collaborations result for p-p collisions at 900 and 7000 GeV as well Pb-Pb collision at 2.76 TeV [11, 13, 16] for strange and non-strange particles. 113

Chapter 1

Introduction

1.1 Historical Overview

The study of relativistic heavy ion collisions combines nuclear physics with elementary particle physics. High-energy nuclear collisions provide a way of analyzing the properties of hot and dense hadronic matter in terms of elementary interactions. The theory behind strong interactions, namely *Quantum Chromodynamics* (QCD), enables us to understand how hadronic matter will turn into a plasma of deconfined quarks and gluons at high density. The ultimate goal of the continuous experimental and theoretical efforts is to search for the phase transition from hadronic matter to a Quark-Gluon Plasma (QGP) [25, 26]. The central objective of the experimental program in heavy ion collisions at high energies is to reproduce matter as it would have been just after the birth of the universe.

In the last 30 years, nuclear collision energies have increased from a few MeV/nucleon for fixed targets to the current collider energies with world wide collaborations. As the energy of the collision is increased, the relevant degrees of freedom change. At the lowest collision energies, the nucleus remains unchanged or is broken up into light nuclear fragments. As the thresholds for particle production are passed in many stages, some of the energy of the system may go into producing new particles, such as pions or kaons. At higher collision energies, the relevant degrees of freedom are expected to be quarks and gluons rather than hadrons [1], forming the QGP [26].

The modern developments in heavy ion collisions are accomplished with beam energies of 10 – 158 GeV/nucleon at fixed-target facilities: e.g. the Alternating Gradient Synchrotron (AGS) at Brookhaven National Laboratory (BNL) and the Super Proton Synchrotron (SPS) at the European Center for Nuclear Research (CERN). Both the AGS and the SPS accelerate protons and several types of ions onto fixed targets of heavy nuclei [27].

The LHC is the world's largest particle accelerator. It is expected to answer some of the most fundamental questions in particle physics, high energy physics and astro-physics; it is advancing the understanding of the deepest laws of nature. In a collider, both collision partners, the "projectile" and "target" are accelerated, leading to much higher energies than those possible at fixed-target facilities. The RHIC at BNL and the LHC at CERN produce Au-Au and Pb-Pb collisions at energies up to 200 GeV/nucleon and 5500 GeV/nucleon respectively in the center of mass frame. These high energies make it possible to increase the production of rare particles that are not accessible at lower energy facilities [28].

The experiments at the RHIC consist of four interaction positions, namely STAR, PHENIX, PHOBOS and BRAHMS (Broad RAnge Hadron Magnetic Spectrometers Experiment at RHIC), and many physicists are involved in setting up the experiment and analyzing the data. At the LHC, both protons and lead ions start their acceleration chain using Linacs which then feed into the Proton Synchrotron (PS) and the SPS before being transferred to the LHC rings. The LHC rings are 27 km in circumference. There are four interaction positions at the LHC, which are, ALICE, ATLAS (A Toroidal LHC ApparatuS), CMS and LHCb (Large Hadron Collider beauty). The ALICE experiment is dedicated to relativistic heavy ion collision studies. CMS and ATLAS are designed to perform high precision studies in p-p col-

---

[1] Hadron is a generic name of a class of particles which interact strongly with one another.

lisions but also perform heavy ion experiments. The LHCb specializes in b-physics (beauty quark physics) experiments, particularly aimed at measuring the parameters of CP violation in the interactions of b-hadrons (heavy particles containing a bottom quark).

For our purpose, we will not go into detail here about the acceleration process or particle detectors. This has been discussed in [27, 29]. This thesis concentrates fully on the statistical models which are used for the hadrons without discussing in detail the phenomenological aspect of these collisions. In section 1.2, we introduce some of the important concepts of the interactions in heavy ion collisions. Moreover, heavy ion experiments now are at energies approaching those of fundamental interactions in particle physics.

1.2 Relativistic Heavy-Ion Collisions

In most cases, the collected data for heavy ion collisions show that the hadronic matter at *chemical freeze-out* (i.e., the moment when inelastic collisions stop) is well characterized by equilibrium distributions [30, 31, 32, 33, 34, 35].

RHIC collides two beams of gold ions traveling at nearly the speed of light. The collision "melts" the protons and neutrons and, for a brief instant, liberates their constituent quarks and gluons. Just after the collision, thousands more particles are formed as the system cools off. These particles provide a clue as to what occurred inside the collision zone.

By utilizing high-energy nuclear collisions, it is possible to study nuclear matter under conditions of very high temperatures and densities. The most common form of nuclear matter, under terrestrial conditions, is found in the atomic nucleus, which consists of protons and neutrons bound together by the strong nuclear force. If nuclear matter is heated up to temperatures comparable to the rest mass of the pion, it becomes a mixture of nucleons, pions, and various other particles, collectively denoted hadrons. Under these circumstances, nuclear matter is referred to as hadronic matter [26].

1.2.1 Quarks

Quarks are the basic constituents of elementary particles. Theoretical models built on the quark concept have been very successful in understanding and predicting many phenomena in the physics of elementary particles [28].

It was plausible that the charge cloud which constitutes the proton is a probability distribution of some smaller, perhaps point like constituents [36]. Subsequent high energy, deep inelastic scattering experiments of electrons on protons, leading to meson production, revealed form factors corresponding to point like constituents of the proton. These proton constituents, first referred to as partons, are now understood to include the constituent quarks of the proton. The properties of quarks are shown in table 1.1.

Table 1.1: Properties of quarks. The charge is in units of the magnitude of the charge of an electron, 1.6×10^{-19} coulomb, spin is in units of $\hbar$. The top quark mass is deduced from experimental measurements of its decay dynamics (F - Flavor, M - Mass, Q - Electric Charge, B - Baryon number, I_3 - Isospin Spin, S - Strangeness, C - Charm, b - beauty and T - Top) [24].

F	M, GeV/c^2	Q	B	Spin	I_3	S	C	b	T
u	$0.0015 - 0.004$	$+2/3$	$+1/3$	$1/2$	$1/2$	0	0	0	0
d	$0.004 - 0.008$	$-1/3$	$+1/3$	$1/2$	$1/2$	0	0	0	0
c	$1.15 - 1.35$	$+2/3$	$+1/3$	$1/2$	0	0	$+1$	0	0
s	$0.080 - 0.130$	$-1/3$	$+1/3$	$1/2$	0	-1	0	0	0
t	174.3 ± 5.1	$+2/3$	$+1/3$	$1/2$	0	0	0	0	$+1$
b	$4.1 - 4.4$	$-1/3$	$+1/3$	$1/2$	0	0	0	$+1$	0

The proton, neutron, and pion are composed of two kinds (or "flavors") of quarks. A third, more massive quark is a constituent of "strange" particles, including the K mesons and hyperons such as the Λ^0. These are known as the up quark (u), the down quark (d), and the strange quark (s). Baryons are composed of three quarks, for example the proton (uud), neutron (udd), Λ^0 (uds), and Ξ^- (dss). Antiparticles such as antiprotons are formed by the antiquarks of those forming the particle, for example, the antiproton ($\bar{u}\bar{d}\bar{d}$). Mesons are composed of a quark-antiquark pair, such as the π^+ ($u\bar{d}$), π^- ($d\bar{u}$), K^+ ($u\bar{s}$), and K^- ($\bar{u}s$) [36, 37].

A problem arose when the structure of observed baryons required two or, in some cases, three quarks of the same flavor in the same quantum state, a situation forbidden for spin-1/2 particles by the Pauli exclusion principle. In order to accommodate this contradiction, a new quantum number, labeled color, was introduced; the idea is that each quark is red, green, or blue (and the antiquarks, antired, and so forth). The color quantum number then breaks the degeneracy and allows up to three quarks of the same flavor to occupy a single quantum state [38].

According to QCD, hadrons must be colorless; for example, baryons must consist of a red, a green, and a blue quark, and mesons of a quark-antiquark pair of the same color (for example, a red quark and an anti-red antiquark).

1.2.2 Hadrons

Hadrons are categorized in two classes called baryons and mesons. Baryons have half-integer spin, obey Fermi-Dirac statistics, and are fermions. Mesons have zero or integer spin, obey Bose-Einstein statistics, and are known as bosons. The electric charges of baryons and mesons are either zero or an integer times the charge on the electron. Masses of the known mesons and baryons cover a wide range, extending from the π meson, with a mass approximately one-seventh that of the proton, to values of the order of 10 times the proton mass [39].

Hadrons have excited states known as resonances. Each ground state hadron may have several excited states; several hundreds of resonances have been observed in particle physics experiments. Resonances decay extremely quickly with time via the strong nuclear force. In other phases of QCD matter the hadrons may disappear. For example, at very high temperature and high pressure, unless there are sufficiently many flavors of quarks, the theory of QCD predicts that quarks and gluons will no longer be confined within hadrons because the strength of the strong interaction diminishes with energy. This property, which is known as asymptotic freedom, has been experimentally confirmed in the energy range between 1 GeV and 7 TeV [40]. All free hadrons except the proton and antiproton are unstable.

1.2.3 The QCD Phase Diagram

According to the standard model, the evolution of the early universe included a QGP phase at a very early stage (a few tens of microseconds after the Big Bang) before it cooled down and the quarks and gluons hadronised into ordinary nuclear matter [20].

The phase diagram of quark matter is not well understood, either experimentally or theoretically but rather there are different models. A commonly conjectured form of the phase diagram is shown in the Fig. 1.1. The relevant thermodynamic quantities are the quark chemical potential μ and the temperature T. Higher μ means a stronger bias favoring quarks over antiquarks. At low temperatures there are no antiquarks, and then higher μ means a higher density of quarks.

Now, imagine starting at the bottom left corner of the phase diagram as shown in Fig. 1.1, where $\mu = T = 0$. If we heat up the system without introducing any preference for quarks over antiquarks, this corresponds to moving vertically upwards along the T axis. At first, quarks are still confined and we create a gas of hadrons (pions and kaons, mostly). Then around critical temperature, T_c in the range of $(160 - 180)$ MeV, there is a crossover to the QGP: thermal fluctuations break up the pions, and we find a gas of quarks,

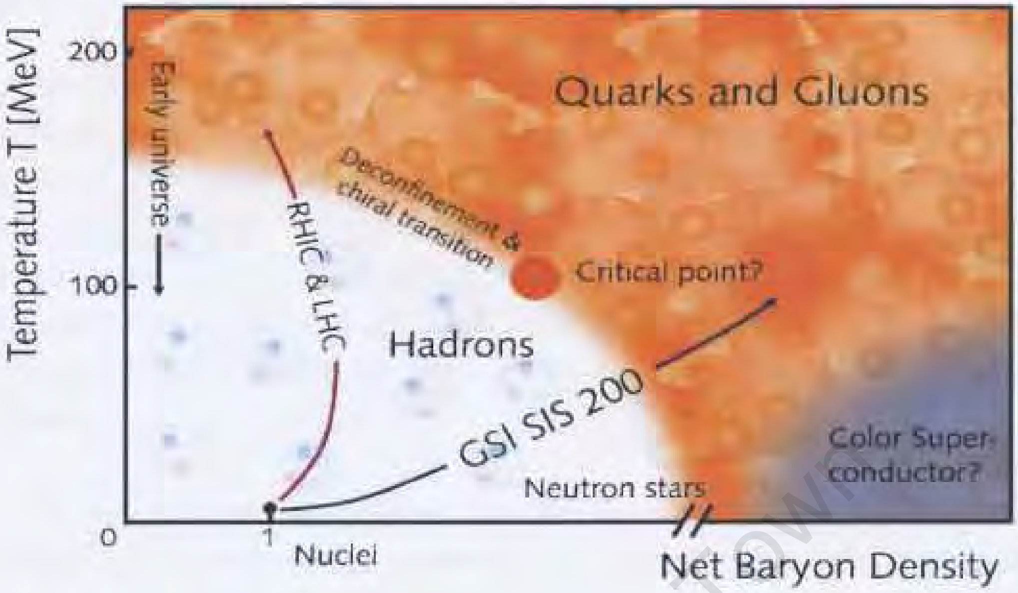

Figure 1.1: Sketch of the QCD phase diagram showing the critical point for the case of light and heavy quarks, a state of deconfined quarks and gluons may exist within neutron stars in the form of a color superconducting state, this figure taken from [20, 21]

antiquarks, and gluons [20, 21, 39].

In the Fig. 1.1, there are two lines, namely "RHIC & LHC" and "GSI (Gesellschaft für Schwerionenforschung) SIS (heavy ion synchrotron) 200" describing the experiments that collide heavy ion nuclei, they rise up from the nuclei to go to the QGP region. Furthermore, between the two lines and across the freeze-out curve show nuclear/quark matter transition marked by "Critical point?", is the conjectured boundary between confined and unconfined phases. It is also believed to be a boundary between phases where chiral symmetry is broken (low temperature and density) and phases where it is unbroken (high temperature and density)[20].

1.3 Thesis Scope

In this thesis, we will focus mainly on the use of statistical thermal models for the hadron particle multiplicities in elementary and relativistic heavy ion collisions. We used the statistical thermal models, i.e., hadron resonance gas model, extended hadron resonance gas model and non-extensive Tsallis statistical models. These models have been implemented, analyzed and discussed for the results of SPS, AGS, GSI, RHIC and LHC experiments in [11, 14, 15, 16, 30, 34, 41, 42, 43]. For this thesis the units are listed in the footnote [2].

In chapter 2, we mainly discuss the Hagedorn spectrum and analyze the results. The Hagedorn temperature, T_H, is determined from the number of hadronic resonances including all mesons and baryons. This leads to a stable result $T_H = 174 \pm 11$ MeV consistent with the critical and the chemical freeze-out temperatures at zero chemical potential [19]. We used this result to calculate the speed of sound and other thermodynamic quantities in the hadronic resonance gas model for a wide range of baryon chemical potentials following the chemical freeze-out curve. We compare some of our results to those obtained previously in other papers [6, 7].

In chapter 3 discuss the results from the extension of the THERMUS code [8] by including charm, c and bottom, b quarks in the particle data table. THERMUS uses the statistical thermal model to analyze experimental results. The statistical thermal model assumes that at freeze-out all hadrons are in the hadron gas. In chapter 3, we mention and state the statistical formalism using the statistical thermal model and explain how to use and implement THERMUS with the 2008 particle data table; and compare some of the results with those literature [22]. Furthermore, we study particle yields and particle ratios as a function of the collision energy by assuming that particle production takes place along the freeze-out curve.

---

[2] Our units are $\hbar = c = k = 1$, where $\hbar$, c and k are the Planck constant divided by 2π, the speed of light and Boltzmann constant respectively. The metric tensor is defined by $g^{\mu\nu}$ = diag(+1, −1, −1, −1).

In chapter 4 we discuss the most promising new development which uses the non-extensive statistical model. This model was first proposed by C. Tsallis, and is called the Tsallis distribution [44]. It is a three decade-old non-extensive generalization of standard statistical distribution. It has been used recently to fit the transverse momentum distributions for identified particles by the STAR [14] and PHENIX [15] collaborations at RHIC and by the ALICE [11] and CMS [16] collaborations at the LHC. We clarify the theoretical background for non-extensive statistics and show its thermodynamical consistency. In addition, using the Tsallis distribution, we extract thermal fit parameters using experimental results from high-energy elementary particle collisions [23, 45] and heavy ion collisions [11, 12, 16].

In particular the Tsallis distribution fits are used to determine particle yields at mid rapidity, average transverse momentum and parameters of the system at thermal freeze-out, such as the freeze-out temperature. We also discuss the Tsallis distribution in the particular case of relativistic high energy transverse momentum distributions. An improved form of parametrization is proposed for describing the transverse momentum distribution. The fits are presented together with estimates of the parameter q, the temperature T and the radius factor R that comes from the volume factor V are presented in chapter 4 [17, 18]. Finally, Chapter 5 makes concluding remarks.

Chapter 2

Thermodynamic quantities in the Extended Hadron Resonance Gas Model

2.1 Hagedorn's Conjecture

In 1965 Hagedorn [1, 2, 3] proposed that the number of hadronic resonances increases exponentially with the mass, m of the resonances. The hypothesis was based on the observation that at some point a further increase of energy in p-p and p-p collisions no longer raises the temperature of the formed fireball, but results in more and more particles being produced. Thus, there is a maximum temperature that a hadronic system can achieve. The Statistical Bootstrap Model [1] predicted that asymptotic behavior. The idea, was debated strongly at a time when it was first proposed. However, it has since been widely accepted and discussed by many authors [46, 47, 48, 49, 50, 51, 52, 53, 54, 55, 56]. The concept was based on the assumption that the observed increase in the number of hadronic resonances would continue towards higher and higher masses as more experimental data became available [57]. The exponential increase determines the value of the Hagedorn temperature, T_H. Recent papers [6, 7, 58, 59, 60, 61] have used the latest results from the Particle Data Group [57] to revisit the original analysis of Hagedorn model and to update the value of T_H. This resulted in a widespread of the possible T_H values, with large variations as to whether one considers mesons or baryons with values ranging from $T_H = 141$ MeV to $T_H = 340$ MeV depending on the parametrization used and on the set of hadrons (mesons or baryons). Thus, there exists uncertainty as to the value of the Hagedorn temperature which have two origins:

- Sparse information about hadronic resonances above 2 GeV and,
- The analytical form of the Hagedorn spectrum, especially the factor multiplying the exponential.

The first item will probably take longer time to be resolved satisfactorily due to the width of resonances and also due to their large number of decay products making it difficult to identify them. Splitting the spectrum into baryons and mesons further decreases the quality of the fits to the mass dependence of the mass spectrum. We therefore propose to stick to the original analysis of Hagedorn and consider a sum over all resonances, baryons, mesons, strange, non-strange, charm, bottom etc. Using a simple parametrization of the hadron mass spectrum, we show how to estimate the total spectral weight of these states. The overview of hadron masses and their spectrum is shown in a tabular form for hadron masses up to 2 GeV in Appendix A. This is the state that is produced at the LHC, namely, a hadronic ensembles containing all possible resonances. The result is shown in Fig. 2.1 and leads to a good determination of T_H because the range of mass (m) is reasonably large extending up to 2 GeV before reaching a plateau presumably due to the sparsity of hadronic resonances above this value. Details about the parametrization used will be presented below.

The Hagedorn temperature naturally leads to the notion that hadronic matter cannot exceed a limiting temperature and increasing the beam energy in p-p and proton-antiproton (p-$\bar{p}$) collisions result in more and more hadronic resonances being produced without a corresponding increase in the temperature of the final (freeze-out) state. This is the situation observed at the highest energies at the LHC [11, 12]. It was suggested [47] that the

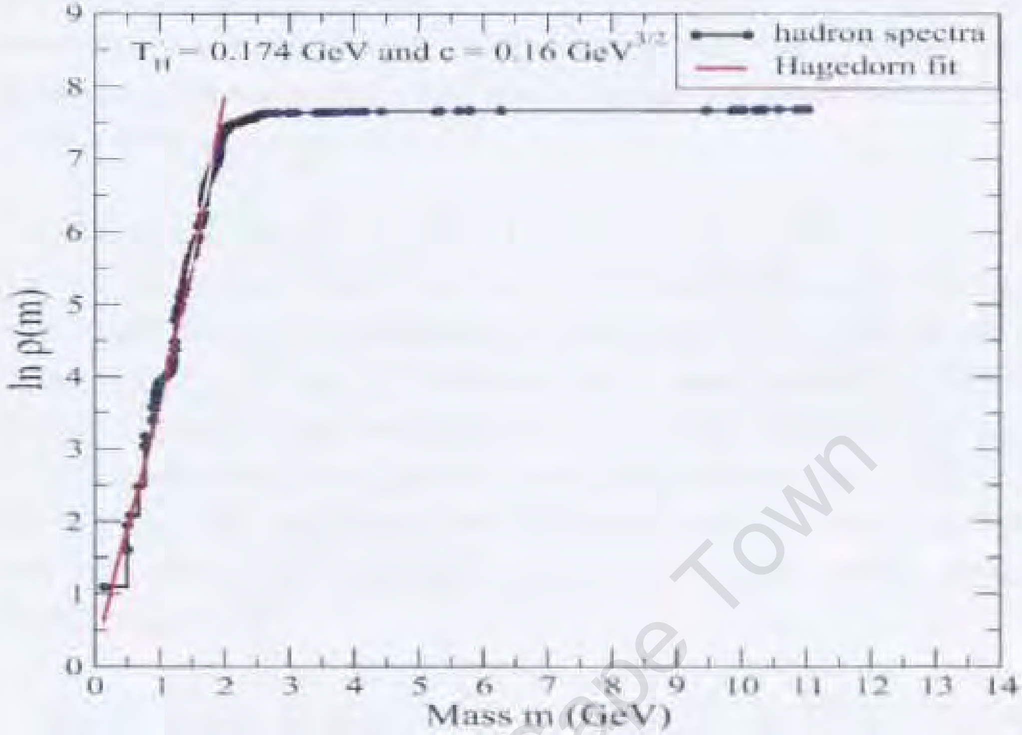

Figure 2.1: Cumulative number of hadronic resonances as a function of m. Again the hadronic data are made up of all resonances, including baryons, mesons and also heavy resonances made up of charm and bottom quarks, the list of hadron masses with their mass spectrum are given in the Appendix A.

Hagedorn temperature is connected to the existence of a different phase in which quarks and gluons are no longer confined. At present, the Hagedorn temperature is often understood as the temperature of the phase transition from a QGP to hadrons.

Recent analysis [6, 62] investigated the hadron resonance gas model [5, 63, 64] and show the stability of various thermodynamic quantities in heavy ion collisions when the Hagedorn spectrum is used in full, (i.e., without a cutoff on the number of resonances beyond a certain mass.). In particular, the authors explored the addition of the hadron resonance gas model including an exponentially large number of undiscovered resonances which are naturally included in the Hagedorn model. Their results showed that the hadron resonance gas model gave different results for thermodynamic quantities such as the energy density, pressure and speed of sound, but the overall chemical analysis was reasonably stable.

Furthermore, the use of so-called Hagedorn States [1] (HS), based on the exponentially increasing spectrum, close to the critical temperature (T_c) can explain fast chemical equilibration by HS regeneration [66] and provide a unique method to compare lattice results for T_c using thermal fits. The HS provide a lower χ^2 than thermal fits without HS [65]. These authors estimated the effects by extending the hadron mass spectrum beyond 3 GeV for $T_H = 200$ MeV and assume that high mass excited K^* states produce only kaon while producing multiple number of pions thus further reducing the K^+/π^+ ratio [62].

In this chapter, we extend previous work of [67, 68, 69] by including explicit expressions for the relevant thermodynamic quantities for non-zero chemical potentials. In particular, the speed of sound, C_s can be considered as a sensitive indicator of the critical behavior in strongly interacting matter [55]. The results show a sharp dip of C_s in the critical region, which is an indication that thermodynamics in the vicinity of confinement is indeed driven by the higher excited hadronic states.

The outline of this chapter is as follows. In section 2.2 start with motivation, and in section 2.3, we present the influence of the Hagedorn spectrum on the hadronic yields to find the thermodynamic parameters and explain the basic concepts used in this chapter. In section 2.4, we derive the number, energy and entropy densities and in section 2.5 discuss the derivation of speed of sound using relativistic fluid dynamics, in addition to that, expressed in Hadron Resonance Gas Model (HRGM) in more detail manner. In section 2.6, we show the results using HRGM and its Extension of Hadron Resonance

---

[1] Hagedorn states provide extra degrees of freedom that can contribute to fast chemical equilibration times for a hadron gas [65].

Gas Model (EHRGM) for particular thermodynamic quantities and discuss the dependence of squared speed of sound, C_s^2 on temperature and chemical potentials, then compare thermodynamic quantities, like energy density, entropy density and specific heat for both models, i.e., HRGM and EHRGM.

2.2 Motivation

The particle data table contains hundreds of hadronic resonances [57] including the well-known stable hadrons (under strong interaction) like nucleons, pions, hyperons (Ω, Σ, Ξ), kaons e.t.c. In our calculations we used a list of hadronic resonances including in total 250 baryons and antibaryons, in total 348 mesons and antimesons, i.e, the antiparticle of mesons (counted without considering their isospin and spin degeneracies). Most of the hadronic resonances decay quickly via strong interactions before reaching the detector. The mass of a decaying particle is equal to the total energy of the products measured in its rest frame.

The basic idea of this chapter is to add resonances to the hadron gas using the Hagedorn model for the spectrum. Using the hadronic data we show the relationship between the number of hadronic resonances and the mass in Fig. 2.1 where we took hadrons with masses up to 11.019 GeV. The density of states, ρ_h [46] obtained this way has been fitted using the following equation:

$$\rho_h(m) = \frac{c}{(m^2 + m_0^2)^{5/4}} \exp\left(\frac{m}{T_H}\right). \tag{2.1}$$

where c is a normalization constant and m_0 is a particular defined mass constant are given in table 2.1. In this model, m_0 is usually fixed at 0.5 GeV; the same approach is used by the authors in [6, 7]. According to S. Chatterjiee [6] stated that in Eq. (2.1) used $m_0 = 0.5$ GeV and variations in m_0 have been explored and discussed in [6, 7]. Note that $m_0 \to \infty$, the pre-exponential factor becomes constant. Hence, choosing proper m_0 will improve the quality of fit.

Table 2.1: The result for the parameters c, m_0 and T_H using Eq. (2.1) and the hadron resonances listed in appendix A.

Parameter	Value
$c\ (GeV)^{3/2}$	0.16 ± 0.02
$m_0\ (GeV)$	0.5
$T_H\ (GeV)$	0.174 ± 0.011

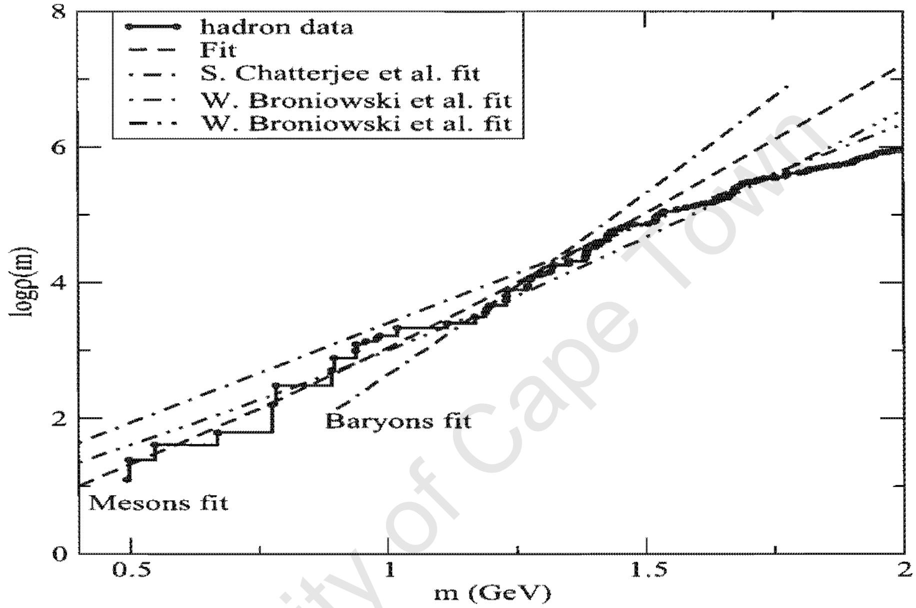

Figure 2.2: Cumulative number of hadronic resonances as a function of m. The hadron data are included up to 2.0 GeV, including baryons and mesons from the fits of different authors, our fit is also shown here (dashed line).

2.3 The Hadron Resonance Gas Model and its Extension

The Hadron Resonance Gas Model (HRGM) turned out to be very successful in describing particle abundances produced in heavy ion collisions. It was also used to estimate QCD transport coefficients in [66]. Thermodynamic quantities calculated in lattice QCD [70] agree well with the HRGM occurs only below T_H if the masses of the hadrons in the model are tuned appropriately to match the large quark mass used in lattice calculations [71, 72, 73]. The thermodynamic properties of the HRGM can be determined from the partition function

$$\begin{aligned} \ln Z(V,T,\mu) &= \int dm\, [\rho_M(m) \ln Z_b(m,V,T,\mu) \\ &+ \rho_B(m) \ln Z_f(m,V,T,\mu)], \end{aligned} \tag{2.2}$$

where the gas is contained in a volume V; and has a temperature T and chemical potential μ, (chemical potential, μ defined as the combination of charge, baryon and strange numbers). Z_b and Z_f are the partition functions for an ideal gas of bosons and fermions respectively with mass m, $\rho_M(m)$ and $\rho_B(m)$ are the spectral density of mesons and baryons. By using Eq. 2.2, one can compute the number density, n, energy density ε, entropy density s, pressure P, speed of sound C_s and specific heat C_v.

Hadronic properties enter these models via $\rho(m)$ (where $\rho(m)$ is the total density of mesons and baryons). The HRGM model takes the observed spectrum of hadrons up to some cutoff mass Λ.

$$\rho(m) = \rho_M(m) + \rho_B(m) = \sum_i^{m_i \leq \Lambda} g_i \delta(m - m_i), \tag{2.3}$$

where m_i are the masses of the known hadrons and g_i the corresponding degeneracy factor. In order to explore the stability of results obtained using the HRGM, one takes the observed spectrum of states up to a certain cutoff of mass Λ and above this one includes an exponentially rising density of hadron states, which is defined in Eq. 2.1. This defines the EHRGM. The density of states in this model is given by

$$\rho(m) = \sum_i^{m_i \leq \Lambda} g_i \delta(m - m_i) + \frac{c}{(m^2 + m_0^2)^{5/4}} \exp\left(\frac{m}{T_H}\right) \theta(m - \Lambda). \tag{2.4}$$

where the parameters c and T_H are fitted to data on the cumulative distribution of the sets of hadrons, h. Typically this model uses $m_0 = 0.5$ GeV, it is adopted from references [6, 7]. The parameters are determined from the hadronic spectrum with masses up to 2 GeV as shown in Fig. 2.1 and 2.2. The results for c and T_H are given in Table 2.1.

2.4 Expression of thermodynamic quantities in EHRGM

The basic quantity required to compute the chemical composition of hadron yields measured in heavy ion collisions is the partition function $Z(T, V, \mu)$. We are considering here the Boltzmann distribution for simplicity in order to present some of the results in a compact form. For a single particle, in the grand canonical ensemble, the partition function is expressed by [11, 12]

$$\ln Z = \sum_{i=1}^{m_i<\Lambda} \frac{gVTm_i^2}{2\pi^2} K_2\left(\frac{m_i}{T}\right) \exp\left(\frac{\mu_i}{T}\right), \tag{2.5}$$

where K_2 is modified Bessel function and $\mu_i = S_i\mu_S + B_i\mu_B + Q_i\mu_Q$. The meson and baryon mass distribution are taken to be given by (2.4).

2.4.1 Particle density and pressure

The particle number density (total number density) is often denoted by a lower-case letter n, then it is expressed by

$$\begin{aligned} n(T, \mu_B, \mu_S, \mu_Q) &= \frac{T}{2\pi^2} \sum_{i=1}^{m_i<\Lambda} \exp\left(\frac{\mu_i}{T}\right) \left[g_i m_i^2 K_2\left(\frac{m_i}{T}\right) \right. + \\ & \left. c\int_{m=\Lambda}^{\infty} \frac{m^2}{(m^2+m_0^2)^{5/4}} \exp\left(\frac{m}{T_H}\right) K_2\left(\frac{m}{T}\right) dm \right] \end{aligned} \tag{2.6}$$

Very often, it is considered to an isospin symmetric system, where $\mu_Q = 0.0$ GeV. The pressure is expressed by

$$P(T, \mu_B, \mu_S, \mu_Q) = T\frac{\partial \ln Z}{\partial V}, \tag{2.7}$$

where the pressure can also expressed in terms of the number density times temperature, i.e., $P = nT$; this is correct only for Boltzmann distribution.

2.4.2 Energy and entropy densities and specific heat

The energy density using Boltzmann distribution which consists of mesons or baryons can be expressed as

$$\varepsilon(T, \mu_B, \mu_S, \mu_Q) = \frac{T^2}{V}\frac{\partial}{\partial T}\ln Z + \sum_i \frac{\mu_i}{V}\frac{\partial}{\partial \mu_i} T \ln Z. \tag{2.8}$$

The energy density using the Hagedorn spectrum is given by

$$\varepsilon(T, \mu_B, \mu_S, \mu_Q) = \sum_{i=1}^{m<\Lambda} \left[\frac{T^2}{2\pi^2} \exp\left(\frac{\mu_i}{T}\right) \left(g_i m_i^2 \left[3K_2\left(\frac{m_i}{T}\right) + \frac{m_i}{T} K_1\left(\frac{m_i}{T}\right) \right] + A_1 \right) \right], \tag{2.9}$$

where

$$A_1 = c \int_m^\infty \frac{m^2}{(m^2 + m_0^2)^{5/4}} \exp\left(\frac{m}{T_H}\right) \left[3K_2\left(\frac{m}{T}\right) + \frac{m}{T} K_1\left(\frac{m}{T}\right) \right] dm.$$

The entropy density, s and the specific heat C_v can be computed using the following relation

$$s(T, \mu_B, \mu_S, \mu_Q) = \frac{\varepsilon + P - n_S\mu_S - n_B\mu_B - n_Q\mu_Q}{T}, \tag{2.10}$$

where n_S, n_B and n_Q are the net number densities for strange, baryonic and charge particles respectively

$$n_{S(B)} \equiv \frac{T}{V}\frac{\partial \ln Z}{\partial \mu_{S(B)}}, \tag{2.11}$$

and the specific heat capacity C_V is the quantity of heat needed to raise the temperature of a system by one unit of temperature at fixed volume, it reads

$$C_V(T, \mu_B, \mu_S, \mu_Q) = T\left(\frac{\partial S}{\partial T}\right)_V = \left(\frac{\partial E}{\partial T}\right)_{N,V}. \tag{2.12}$$

The detailed derivation for the thermodynamic quantities using HRGM is given in the appendix B.

2.5 Speed of Sound in relativistic fluid dynamics

In the local rest frame, the energy-momentum tensor of an ideal gas has the form

$$T^{\mu\nu} = \begin{bmatrix} \varepsilon & 0 & 0 & 0 \\ 0 & P & 0 & 0 \\ 0 & 0 & P & 0 \\ 0 & 0 & 0 & P \end{bmatrix}.$$

It is straightforward to find an expression for $T^{\mu\nu}$ in any frame of reference [74]. To do so, we use the fluid 4-velocity u^μ. In the local rest frame, $u^0 = 1$, $u^i = 0$,(where the letters i and j take the values $1, 2, 3$. corresponding to the spatial coordinates). The energy-momentum tensor considered here does not take account dissipative effects (viscosity and thermal conduction), therefore the equations relate to an ideal fluid. The expression for $T^{\mu\nu}$ which gives the above energy-momentum matrix tensor with these values of u^μ is

$$T^{\mu\nu} = wu^\mu u^\nu - Pg^{\mu\nu}, \tag{2.13}$$

where $w = \varepsilon + P$ is the enthalpy per unit volume. Hence, this is the required expression for the energy-momentum tensor. The components $T^{\mu\nu}$ in three-dimensional form are

$$\begin{aligned} T^{ij} &= \frac{wv^i v^j}{c^2(1 - v^2/c^2)} + P\delta^{ij}, \\ T^{0i} &= \frac{wv^i}{c(1 - v^2/c^2)}, \quad T^{00} = \frac{w}{1 - v^2/c^2} - P = \frac{\varepsilon + Pv^2/c^2}{1 - v^2/c^2}. \end{aligned} \tag{2.14}$$

The continuity equations of ideal relativistic fluid dynamics are contained in

$$\partial_\mu T^{\mu\nu} = 0, \tag{2.15}$$

and

$$\partial_\mu N^\mu_B = 0, \tag{2.16}$$

which express the local laws of conservation of energy-momentum and baryon number but the particle number is not conserved, only quantum numbers like baryon number, electric charge and strangeness are conserved, so Eq. (2.16) should refer to baryon number conservation.

To derive an equation for the conservation of particle number (the equation of continuity), we use the particle flux 4-vector n^μ_B. Its time component is the number density of particles, and the three spatial components form the three-dimensional particle flux vector. The vector n^μ_B must be proportional to the 4-velocity u^μ, so that

$$n^\mu_B = n_B u^\mu, \tag{2.17}$$

where n_B is a scalar and just the baryon number density of particles in the rest frame. The equation of continuity is obtained by simply equating to zero the 4-divergence of the flux vector:

$$\partial_\mu (n_B u^\mu) = 0. \tag{2.18}$$

Let us now return to Eq. (2.13). Differentiating the expression given in Eq. (2.13), we obtain

$$\partial_\nu T^\nu_\mu = u_\mu \partial_\nu (w u^\nu) + w u^\nu \partial_\nu u_\mu - \partial_\mu P = 0. \tag{2.19}$$

We multiply this equation by u^μ, i.e. project it on the direction of the 4-velocity. Since in this space-time derivative decomposition $D \equiv u^\mu \partial_\mu$ is the convective time derivative and $\bigtriangledown^\mu \equiv \bigtriangledown^{\mu\nu}\partial_\nu$ is the gradient operator. The projection onto the 3-space $\bigtriangledown^{\mu\nu} \equiv g^{\mu\nu} - u^\mu u^\nu \equiv \bigtriangledown^{\nu\mu}$ is orthogonal to u^μ, that is, $\bigtriangledown^{\mu\nu} u_\nu = 0$ and u^μ is the hydrodynamical 4-velocity of the net charge and is to be normalized such that $u^\mu u_\mu = 1$ and therefore $u^\mu \partial_\nu u_\mu = 0$ [75].

Thus, we find

$$\partial_\nu(wu^\nu) - u^\nu\partial_\nu P = 0. \tag{2.20}$$

With the identity $wu^\nu = nu^\nu(w/n)$ and the equation of continuity Eq. (2.18), we obtain

$$n_B u^\nu\left[\partial_\nu\left(\frac{w}{n_B}\right) - \frac{1}{n_B}\partial_\nu P\right] = 0.$$

By the thermodynamic relation

$$d(w/n_B) = Td(s/n_B) + (1/n_B)dP. \tag{2.21}$$

where T is the temperature and s the entropy per unit proper volume, the expression in square brackets is $T\partial_\nu(s/n_B) = 0$. Without the factor $n_B T$, we have

$$u^\nu\partial_\nu(s/n_B) \equiv d(s/n_B)/d\sigma = 0, \tag{2.22}$$

which states that the flow is adiabatic and the differentiation given by $d/d\sigma$ describes for the lines of the fluid element concerned. Therefore, their ratio of s and n_B unchanged, this implies that

$$\boxed{d\left(\frac{s}{n_B}\right) = 0}. \tag{2.23}$$

By the equation of continuity Eq. (2.18), Eq. (2.22) can also be written as the vanishing of the 4-divergence of the entropy flux su^μ:

$$\partial_\mu(su^\mu) = 0. \tag{2.24}$$

We now project the energy-momentum tensor on a direction perpendicular to u^μ. For the 4-velocity components we have $u^\mu = (\gamma, \gamma\mathbf{v})$, $u_\mu = (\gamma, -\gamma\mathbf{v})$ where $\gamma = 1/\sqrt{1-v^2}$. This produces the combination

$$\partial_\nu T^\nu_\mu - u_\mu u^\nu\partial_\lambda T^\lambda_\nu = 0;$$

the expression on the left gives zero identically on scalar multiplication by

u^μ. A simple calculation leads to the equation

$$w u^\nu \partial_\nu u_\mu = \partial_\mu P - u_\mu u^\nu \partial_\nu P. \tag{2.25}$$

The three spatial components of this equation are the relativistic generalization of Euler's equation; the time component is implied by the other three. When $s/n_B =$ constant, Eq. (2.21) gives

$$\partial_\mu P = n_B \partial_\mu \left(\frac{w}{n_B}\right),$$

and Eq. (2.25) becomes

$$u^\nu \partial_\nu \left(\frac{w}{n_B} u_\mu\right) = \partial_\mu \left(\frac{w}{n_B}\right). \tag{2.26}$$

If the flow is also steady, with all quantities independent of time, the spatial components of Eq. (2.26) give

$$\gamma(\mathbf{v}.\vec{\nabla})(\gamma w \mathbf{v}/n_B) + \vec{\nabla}(w/n_B) = 0.$$

Scalar multiplication by $\mathbf{v}$ readily leads to the result $(\mathbf{v}.\vec{\nabla})(\gamma w/n_B) = 0$. It follows that along any streamline

$$\gamma w/n_B = \texttt{constant.} \tag{2.27}$$

This is the relativistic generalization of Bernoulli's equation. Without assuming that the isentropic flow[2] is steady, we can easily see that the Eqs. (2.26) have solutions in the form

$$w u_\mu / n_B = -\partial_\mu \psi, \tag{2.28}$$

where ψ is a function of coordinates and time; these are the relativistic analogue of potential flow in a non-relativistic fluid dynamics. To verify this,

---

[2] An isentropic flow is a flow that is both adiabatic and reversible. That is, no heat is added to the flow, and no energy transformations occur due to friction or dissipative effects [76].

we note that, from the symmetry of the derivatives $\partial_\mu(\partial_\nu\psi)$ in μ and ν,

$$\partial_\nu(wu_\mu/n_B) = \partial_\mu(wu_\nu/n_B); \tag{2.29}$$

scalar multiplication by u^ν and expansions of the derivative on the right does in fact bring us back to Eq. (2.26). The spatial and time components of Eq. (2.28) give

$$\gamma w\mathbf{v}/n_B = \overrightarrow{\nabla}\,\psi, \qquad \gamma w/n_B + \partial\psi/\partial t = 0.$$

Let us consider the propagation of sound in a substance having a relativistic equation of state (i.e. one in which the pressure is comparable to the energy density, including the rest energy). The equations of fluid dynamics for the sound waves can be linearized; it is convenient to start from the equations of motion in the original form of $T^{\mu\nu}$. Substituting the expressions Eq. (2.14) for the components of the energy-momentum tensor and retaining only quantities of the same order of smallness as the wave amplitude, we obtain the equations

$$\partial\varepsilon'/\partial t = -w\,\overrightarrow{\nabla}.\mathbf{v}, \qquad w\partial\mathbf{v}/\partial t = -\overrightarrow{\nabla}P', \tag{2.30}$$

where the prime denotes the variable parts of quantities. Eliminating $\mathbf{v}$, we find $\partial^2\varepsilon'/\partial t^2 = \Delta P'$ (where $\Delta = \overrightarrow{\nabla}.\overrightarrow{\nabla} = \overrightarrow{\nabla}^2$). Finally, putting the relation given by $\varepsilon' = (\partial\varepsilon/\partial P)_{ad}P'$, we obtain the wave equation for P', i.e.,

$$\left[\frac{\partial\varepsilon}{\partial P}\right]_{ad}\frac{\partial^2 P'}{\partial t^2} = \Delta P', \tag{2.31}$$

with the velocity of sound,

$$C_s = \sqrt{(\partial P/\partial\varepsilon)_{ad}}; \tag{2.32}$$

the suffix *ad* signifies that the derivative is taken for an adiabatic process, which is for constant s/n_B. Moreover, this formula with the ultra-relativistic equation of state $P = \frac{1}{3}\varepsilon$ leads to the velocity of sound being $C_s = 1/\sqrt{3}$. The relation for the speed of sound given in Eq. (2.32) leads us to proceed to the next sections to solve and analyze it using HRGM and EHRGM for pressure and energy density.

2.5.1 The speed of sound at finite T and μ_B

In hydrodynamic models, the speed of sound plays an important role in the evolution of a system and is an ingredient in the understanding of the effects of a phase transition [67, 68, 69, 77]. It is well-known [74] that the speed of sound has to be calculated at constant entropy per baryon particle density (s/n_B) [3], which is given in section 2.5. This makes the calculation more complicated than the one at zero chemical potential where it is sufficient to keep the temperature fixed. In our extension we take the condition in Eq. (2.32) into account for non-zero baryon and strangeness chemical potentials, imposing overall strangeness zero. The squared speed is thus calculated starting from [74]

$$C_s^2(T,\mu) = \left(\frac{\partial P}{\partial \varepsilon}\right)_{s/n_B}, \tag{2.33}$$

where s/n_B is the entropy per baryon density which is kept fixed and C_s^2 similar to Eq. (2.32), hence C_s^2 depends on T, μ_B and μ_S, this can be rewritten as

$$C_s^2(T,\mu) = \frac{\left(\frac{\partial P}{\partial T}\right) + \left(\frac{\partial P}{\partial \mu_S}\right)\left(\frac{d\mu_S}{dT}\right) + \left(\frac{\partial P}{\partial \mu_B}\right)\left(\frac{d\mu_B}{dT}\right)}{\left(\frac{\partial \varepsilon}{\partial T}\right) + \left(\frac{\partial \varepsilon}{\partial \mu_S}\right)\left(\frac{d\mu_S}{dT}\right) + \left(\frac{\partial \varepsilon}{\partial \mu_B}\right)\left(\frac{d\mu_B}{dT}\right)}, \tag{2.34}$$

where the derivatives $\frac{d\mu_B}{dT}$ and $\frac{d\mu_S}{dT}$ can be evaluated using two conditions. The first condition comes from keeping the ratio (s/n_B) constant. From the derivative one obtains

$$d\left(\frac{s}{n_B}\right) = 0, \tag{2.35}$$

which implies

$$n_B ds = s dn_B. \tag{2.36}$$

---

[3] particle number is not conserved but the ratio of entropy per baryon density should be constant

In terms of T, μ_B and μ_S this equation can be written as

$$n_B\left(\frac{\partial s}{\partial T}\right)dT + n_B\left(\frac{\partial s}{\partial \mu_B}\right)d\mu_B + n_B\left(\frac{\partial s}{\partial \mu_S}\right)d\mu_S = s\left(\frac{\partial n_B}{\partial T}\right)dT + s\left(\frac{\partial n_B}{\partial \mu_B}\right)d\mu_B + s\left(\frac{\partial n_B}{\partial \mu_S}\right)d\mu_S \quad (2.37)$$

divide the above expression by dT on both sides, so that it becomes

$$n_B\left(\frac{\partial s}{\partial T}\right) + n_B\left(\frac{\partial s}{\partial \mu_B}\right)\left(\frac{d\mu_B}{dT}\right) + n_B\left(\frac{\partial s}{\partial \mu_S}\right)\left(\frac{d\mu_S}{dT}\right) = s\left(\frac{\partial n_B}{\partial T}\right) + s\left(\frac{\partial n_B}{\partial \mu_B}\right)\left(\frac{d\mu_B}{dT}\right) + s\left(\frac{\partial n_B}{\partial \mu_S}\right)\left(\frac{d\mu_S}{dT}\right) \quad (2.38)$$

Rearranging the above expression in order to write $\frac{d\mu_B}{dT}$ in terms of $\frac{d\mu_S}{dT}$ one obtains

$$\left[n_B\left(\frac{\partial s}{\partial \mu_B}\right) - s\left(\frac{\partial n_B}{\partial \mu_B}\right)\right]\left(\frac{d\mu_B}{dT}\right) = s\left(\frac{\partial n_B}{\partial T}\right) - n_B\left(\frac{\partial s}{\partial T}\right) - \left[n_B\left(\frac{\partial s}{\partial \mu_S}\right) - s\left(\frac{\partial n_B}{\partial \mu_S}\right)\right]\left(\frac{d\mu_S}{dT}\right) \quad (2.39)$$

Defining

$$A = n_B\left(\frac{\partial s}{\partial T}\right) - s\left(\frac{\partial n_B}{\partial T}\right), \quad (2.40)$$

$$B = n_B\left(\frac{\partial s}{\partial \mu_B}\right) - s\left(\frac{\partial n_B}{\partial \mu_B}\right), \quad (2.41)$$

$$C = n_B\left(\frac{\partial s}{\partial \mu_S}\right) - s\left(\frac{\partial n_B}{\partial \mu_S}\right). \quad (2.42)$$

The final expression for condition one is

$$\frac{d\mu_B}{dT} = -\frac{1}{B}\left[A + C\frac{d\mu_S}{dT}\right]. \quad (2.43)$$

The second condition comes from overall strangeness neutrality, which is

$$n_S = n_{\bar{S}} \quad (2.44)$$

where n_S and $n_{\bar{S}}$ are the strange and antistrange particle densities. Similarly the derivative of equation Eq. (4.3) should thus satisfy

$$d(n_S) = d(n_{\bar{S}}) \tag{2.45}$$

this implies that Eq. (2.45) can be expressed as

$$\begin{aligned} &\left(\frac{\partial n_S}{\partial T}\right) + \left(\frac{\partial n_S}{\partial \mu_B}\right)\left(\frac{d\mu_B}{dT}\right) + \left(\frac{\partial n_S}{\partial \mu_S}\right)\left(\frac{d\mu_S}{dT}\right) \\ &= \left(\frac{\partial n_{\bar{S}}}{\partial T}\right) + \left(\frac{\partial n_{\bar{S}}}{\partial \mu_B}\right)\left(\frac{d\mu_B}{dT}\right) + \left(\frac{\partial n_{\bar{S}}}{\partial \mu_S}\right)\left(\frac{d\mu_S}{dT}\right). \end{aligned} \tag{2.46}$$

We can apply the same method as above to write $\frac{d\mu_B}{dT}$ in terms of $\frac{d\mu_S}{dT}$ for the above relation

$$\begin{aligned} &\left[\left(\frac{\partial n_S}{\partial \mu_B}\right) - \left(\frac{\partial n_{\bar{S}}}{\partial \mu_B}\right)\right]\left(\frac{d\mu_B}{dT}\right) \\ &= \left(\frac{\partial n_{\bar{S}}}{\partial T}\right) - \left(\frac{\partial n_S}{\partial T}\right) - \left[\left(\frac{\partial n_S}{\partial \mu_S}\right) - \left(\frac{\partial n_{\bar{S}}}{\partial \mu_S}\right)\right]\left(\frac{d\mu_S}{dT}\right), \end{aligned} \tag{2.47}$$

we define $L = n_S$, which represents the strangeness density for baryons and mesons

$$L = n_S^B + n_S^M,$$

and $R = n_{\bar{S}}$, the antistrangeness density for baryons and mesons

$$R = n_S^{\bar{B}} + n_S^{\bar{M}}.$$

Define now

$$E = \frac{\partial L}{\partial \mu_B} - \frac{\partial R}{\partial \mu_B}, \tag{2.48}$$

$$F = \frac{\partial L}{\partial \mu_S} - \frac{\partial R}{\partial \mu_S}, \tag{2.49}$$

$$D = \frac{\partial L}{\partial T} - \frac{\partial R}{\partial T}. \tag{2.50}$$

Hence, the final expression for condition two becomes

$$\frac{d\mu_B}{dT} = -\frac{1}{E}\left[D + F\frac{d\mu_S}{dT}\right]. \tag{2.51}$$

Finally, by equating Eq. (2.43) and Eq. (2.51) we find

$$\frac{d\mu_S}{dT} = \frac{AE - BD}{BF - CE}, \tag{2.52}$$

and

$$\frac{d\mu_B}{dT} = \frac{CD - AF}{BF - CE}, \tag{2.53}$$

therefore, by plugging the relations of $\frac{d\mu_B}{dT}$ and $\frac{d\mu_S}{dT}$ that is used in the Eq. (2.33), so that we can find the explicit value of C_s^2 as a function of T, μ_B and μ_S. In the next subsection we will derive the more general form of speed of sound that involves all the chemical potentials which are baryons, strangeness, charge, charm and bottom quantum numbers will be considered.

A More General Form of Speed of Sound

In this section calculate the speed of sound by involving all the chemical potentials (i.e., μ_B, μ_S, μ_Q, μ_C and μ_b) for hadrons, which is given by

$$C_s^2(T, \mu) = \frac{R_1}{R_2}, \tag{2.54}$$

where

$$\begin{aligned} R_1 &= \left(\frac{\partial P}{\partial T}\right) + \left(\frac{\partial P}{\partial \mu_B}\right)\left(\frac{d\mu_B}{dT}\right) \\ &+ \left(\frac{\partial P}{\partial \mu_S}\right)\left(\frac{d\mu_S}{dT}\right) + \left(\frac{\partial P}{\partial \mu_Q}\right)\left(\frac{d\mu_Q}{dT}\right) \\ &+ \left(\frac{\partial P}{\partial \mu_C}\right)\left(\frac{d\mu_C}{dT}\right) + \left(\frac{\partial P}{\partial \mu_b}\right)\left(\frac{d\mu_b}{dT}\right) \end{aligned} \tag{2.55}$$

and

$$\begin{aligned} R_2 &= \left(\frac{\partial \varepsilon}{\partial T}\right) + \left(\frac{\partial \varepsilon}{\partial \mu_B}\right)\left(\frac{d\mu_B}{dT}\right) \\ &+ \left(\frac{\partial \varepsilon}{\partial \mu_S}\right)\left(\frac{d\mu_S}{dT}\right) + \left(\frac{\partial \varepsilon}{\partial \mu_Q}\right)\left(\frac{d\mu_Q}{dT}\right) \\ &+ \left(\frac{\partial \varepsilon}{\partial \mu_C}\right)\left(\frac{d\mu_C}{dT}\right) + \left(\frac{\partial \varepsilon}{\partial \mu_b}\right)\left(\frac{d\mu_b}{dT}\right), \end{aligned} \tag{2.56}$$

where C and b stands for charm and bottom quantum numbers respectively. We will a follow similar approach for the derivation of C_s^2 to the one given in section 2.5.1. Hence, all chemical conservation relations can be written as

$$\begin{aligned} n_B &= n_{\bar{B}} + \texttt{constant}, \\ n_S &= n_{\bar{S}}, \\ n_Q &= n_{\bar{Q}} + \texttt{constant}, \\ n_C &= n_{\bar{C}}, \\ n_b &= n_{\bar{b}}, \end{aligned} \tag{2.57}$$

where the conservation of the number of baryon n_B, strangeness n_S, charge n_Q, charm n_C and bottom n_b densities respectively. Hence, its derivatives becomes

$$d(n_B) = d(n_{\bar{B}}), \tag{2.58a}$$

$$d(n_S) = d(n_{\bar{S}}), \tag{2.58b}$$

$$d(n_Q) = d(n_{\bar{Q}}), \tag{2.58c}$$

$$d(n_C) = d(n_{\bar{C}}), \tag{2.58d}$$

$$d(n_b) = d(n_{\bar{b}}), \tag{2.58e}$$

it is also possible to write Eq. (2.58a), in this way

$$d(n_B) = \frac{\partial n_B}{\partial T}dT + \frac{\partial n_B}{\partial \mu_B}d\mu_B + \frac{\partial n_B}{\partial \mu_S}d\mu_S + \frac{\partial n_B}{\partial \mu_Q}d\mu_Q + \frac{\partial n_B}{\partial \mu_C}d\mu_C + \frac{\partial n_B}{\partial \mu_b}d\mu_b \tag{2.59}$$

and

$$d(n_{\bar{B}}) = \frac{\partial n_{\bar{B}}}{\partial T}dT + \frac{\partial n_{\bar{B}}}{\partial \mu_B}d\mu_B + \frac{\partial n_{\bar{B}}}{\partial \mu_S}d\mu_S + \frac{\partial n_{\bar{B}}}{\partial \mu_Q}d\mu_Q + \frac{\partial n_{\bar{B}}}{\partial \mu_C}d\mu_C + \frac{\partial n_{\bar{B}}}{\partial \mu_b}d\mu_b \quad (2.60)$$

by combining Eq. (2.59) and (2.60) into Eq. (2.58a) and divide both sides by dT, we obtain

$$\begin{aligned}
&\frac{\partial n_B}{\partial T} + \frac{\partial n_B}{\partial \mu_B}\frac{d\mu_B}{dT} + \frac{\partial n_B}{\partial \mu_S}\frac{d\mu_S}{dT} + \frac{\partial n_B}{\partial \mu_Q}\frac{d\mu_Q}{dT} + \frac{\partial n_B}{\partial \mu_C}\frac{d\mu_C}{dT} + \frac{\partial n_B}{\partial \mu_b}\frac{d\mu_b}{dT} = \\
&\frac{\partial n_{\bar{B}}}{\partial T} + \frac{\partial n_{\bar{B}}}{\partial \mu_B}\frac{d\mu_B}{dT} + \frac{\partial n_{\bar{B}}}{\partial \mu_S}\frac{d\mu_S}{dT} + \frac{\partial n_{\bar{B}}}{\partial \mu_Q}\frac{d\mu_Q}{dT} + \frac{\partial n_{\bar{B}}}{\partial \mu_C}\frac{d\mu_C}{dT} + \frac{\partial n_{\bar{B}}}{\partial \mu_b}\frac{d\mu_b}{dT} \qquad (2.61)
\end{aligned}$$

rearranging to yield,

$$a_1\frac{d\mu_B}{dT} + a_2\frac{d\mu_S}{dT} + a_3\frac{d\mu_Q}{dT} + a_4\frac{d\mu_C}{dT} + a_5\frac{d\mu_b}{dT} = a_0 \qquad (2.62)$$

where

$$a_0 = -\left[\frac{\partial n_B}{\partial T} - \frac{\partial n_{\bar{B}}}{\partial T}\right], \quad a_1 = \frac{\partial n_B}{\partial \mu_B} - \frac{\partial n_{\bar{B}}}{\partial \mu_B}, \quad a_2 = \frac{\partial n_B}{\partial \mu_S} - \frac{\partial n_{\bar{B}}}{\partial \mu_S}, \quad a_3 = \frac{\partial n_B}{\partial \mu_Q} - \frac{\partial n_{\bar{B}}}{\partial \mu_Q}.$$

and

$$a_4 = \frac{\partial n_B}{\partial \mu_C} - \frac{\partial n_{\bar{B}}}{\partial \mu_C}, \quad a_5 = \frac{\partial n_B}{\partial \mu_b} - \frac{\partial n_{\bar{B}}}{\partial \mu_b}.$$

We applied a similar approach to the other Eqs. in (2.58b), (2.58c), (2.58d) and (2.58e). Hence, we obtain

$$b_1\frac{d\mu_B}{dT} + b_2\frac{d\mu_S}{dT} + b_3\frac{d\mu_Q}{dT} + b_4\frac{d\mu_C}{dT} + b_5\frac{d\mu_b}{dT} = b_0. \qquad (2.63a)$$

$$c_1\frac{d\mu_B}{dT} + c_2\frac{d\mu_S}{dT} + c_3\frac{d\mu_Q}{dT} + c_4\frac{d\mu_C}{dT} + c_5\frac{d\mu_b}{dT} = c_0, \qquad (2.63b)$$

$$d_1\frac{d\mu_B}{dT} + d_2\frac{d\mu_S}{dT} + d_3\frac{d\mu_Q}{dT} + d_4\frac{d\mu_C}{dT} + d_5\frac{d\mu_b}{dT} = d_0, \qquad (2.63c)$$

$$e_1\frac{d\mu_B}{dT} + e_2\frac{d\mu_S}{dT} + e_3\frac{d\mu_Q}{dT} + e_4\frac{d\mu_C}{dT} + e_5\frac{d\mu_b}{dT} = e_0. \qquad (2.63d)$$

where

$$b_0 = -\left[\frac{\partial n_S}{\partial T} - \frac{\partial n_{\bar{S}}}{\partial T}\right], \quad b_1 = \frac{\partial n_S}{\partial \mu_B} - \frac{\partial n_{\bar{S}}}{\partial \mu_B}, \quad b_2 = \frac{\partial n_S}{\partial \mu_S} - \frac{\partial n_{\bar{S}}}{\partial \mu_S}, \quad b_3 = \frac{\partial n_S}{\partial \mu_Q} - \frac{\partial n_{\bar{S}}}{\partial \mu_Q},$$

$$c_0 = -\left[\frac{\partial n_Q}{\partial T} - \frac{\partial n_{\bar{Q}}}{\partial T}\right], \quad b_4 = \frac{\partial n_S}{\partial \mu_C} - \frac{\partial n_{\bar{S}}}{\partial \mu_C}, \quad b_5 = \frac{\partial n_S}{\partial \mu_b} - \frac{\partial n_{\bar{S}}}{\partial \mu_b}, \quad c_1 = \frac{\partial n_Q}{\partial \mu_B} - \frac{\partial n_{\bar{Q}}}{\partial \mu_B}.$$

$$d_0 = -\left[\frac{\partial n_C}{\partial T} - \frac{\partial n_{\bar{C}}}{\partial T}\right], \quad c_2 = \frac{\partial n_Q}{\partial \mu_S} - \frac{\partial n_{\bar{Q}}}{\partial \mu_S}, \quad c_3 = \frac{\partial n_Q}{\partial \mu_Q} - \frac{\partial n_{\bar{Q}}}{\partial \mu_Q}, \quad c_4 = \frac{\partial n_Q}{\partial \mu_C} - \frac{\partial n_{\bar{Q}}}{\partial \mu_C}.$$

$$e_0 = -\left[\frac{\partial n_b}{\partial T} - \frac{\partial n_{\bar{b}}}{\partial T}\right], \quad c_5 = \frac{\partial n_Q}{\partial \mu_b} - \frac{\partial n_{\bar{Q}}}{\partial \mu_b}, \quad d_1 = \frac{\partial n_C}{\partial \mu_B} - \frac{\partial n_{\bar{C}}}{\partial \mu_B}, \quad d_2 = \frac{\partial n_C}{\partial \mu_S} - \frac{\partial n_{\bar{C}}}{\partial \mu_S},$$

$$d_3 = \frac{\partial n_C}{\partial \mu_Q} - \frac{\partial n_{\bar{C}}}{\partial \mu_Q}, \quad d_4 = \frac{\partial n_C}{\partial \mu_C} - \frac{\partial n_{\bar{C}}}{\partial \mu_C}, \quad d_5 = \frac{\partial n_C}{\partial \mu_b} - \frac{\partial n_{\bar{C}}}{\partial \mu_b}, \quad e_1 = \frac{\partial n_b}{\partial \mu_B} - \frac{\partial n_{\bar{b}}}{\partial \mu_B},$$

$$e_2 = \frac{\partial n_b}{\partial \mu_S} - \frac{\partial n_{\bar{b}}}{\partial \mu_S}, \quad e_3 = \frac{\partial n_b}{\partial \mu_Q} - \frac{\partial n_{\bar{b}}}{\partial \mu_Q}, \quad e_4 = \frac{\partial n_b}{\partial \mu_C} - \frac{\partial n_{\bar{b}}}{\partial \mu_C}, \quad e_5 = \frac{\partial n_b}{\partial \mu_b} - \frac{\partial n_{\bar{b}}}{\partial \mu_b}.$$

and

$$\frac{\mu_B}{dT} = V, \quad \frac{\mu_S}{dT} = W, \quad \frac{\mu_Q}{dT} = X, \quad \frac{\mu_C}{dT} = Y, \quad \frac{\mu_b}{dT} = Z.$$

these imply that we can rewrite Eqs. (2.63a), (2.63b), (2.63c) and (2.63d) in a more general form of equation

$$\begin{aligned}
a_1V + a_2W + a_3X + a_4Y + a_5Z &= a_0, \\
b_1V + b_2W + b_3X + b_4Y + b_5Z &= b_0, \\
c_1V + c_2W + c_3X + c_4Y + c_5Z &= c_0, \\
d_1V + d_2W + d_3X + d_4Y + d_5Z &= d_0, \\
e_1V + e_2W + e_3X + e_4Y + e_5Z &= e_0.
\end{aligned}$$

The above equation can be represented in matrix form as

$$m\overrightarrow{x} = \overrightarrow{v} \tag{2.64}$$

which means, we write

$$\begin{bmatrix} a_1 & a_2 & a_3 & a_4 & a_5 \\ b_1 & a_2 & a_3 & a_4 & a_5 \\ c_1 & a_2 & a_3 & a_4 & a_5 \\ d_1 & a_2 & a_3 & a_4 & a_5 \\ e_1 & a_2 & a_3 & a_4 & a_5 \end{bmatrix} \begin{bmatrix} V \\ W \\ X \\ Y \\ Z \end{bmatrix} = \begin{bmatrix} a_0 \\ b_0 \\ c_0 \\ d_0 \\ e_0 \end{bmatrix},$$

where the 5 × 5 matrix m, $\overrightarrow{x}$ and $\overrightarrow{v}$ are given by

$$m = \begin{bmatrix} a_1 & a_2 & a_3 & a_4 & a_5 \\ b_1 & a_2 & a_3 & a_4 & a_5 \\ c_1 & a_2 & a_3 & a_4 & a_5 \\ d_1 & a_2 & a_3 & a_4 & a_5 \\ e_1 & a_2 & a_3 & a_4 & a_5 \end{bmatrix},$$

$$\overrightarrow{x} = \begin{bmatrix} V \\ W \\ X \\ Y \\ Z \end{bmatrix}$$

and

$$\vec{v} = \begin{bmatrix} a_0 \\ b_0 \\ c_0 \\ d_0 \\ e_0 \end{bmatrix}.$$

The solution of this matrix will lead us to solve the general form of the speed of sound for non-zero chemical potentials using the conservation laws.

2.6 Results using HRGM and EHRGM

There is not much difference between the HRGM and EHRGM models at low temperature, $T \ll T_H$ since the heavy resonances do not play an important role there. Alternatively, at high temperatures, $T \gg T_H$, it should agree with the results of the lattice simulations of QCD [78, 79, 80, 81]. In our case, we have determined the temperature and chemical potential (i.e., μ_B and μ_S) dependencies of the thermodynamics variable using the chemical freeze-out curve; these have been used and discussed in [5, 63, 64]. Based on these results, we have calculated the speed of sound.

For the thermodynamic quantities that are defined earlier, we will show graphically their temperature, T, and chemical potentials (i.e., μ_B and μ_S) dependences. For each thermodynamic quantity, we have set three conditions based on the presence of μ_B and μ_S, namely:

condition A: when both chemical potentials, μ_B and μ_S are zero, i.e.,

$$\mu_B = 0 \quad \text{and} \quad \mu_S = 0,$$

condition B: when μ_S is zero but μ_B is non-zero, i.e.,

$$\mu_B \neq 0 \quad \text{and} \quad \mu_S = 0,$$

condition C: when both chemical potentials, μ_B and μ_S are non-zero, i.e.,

$$\mu_B \neq 0 \quad \text{and} \quad \mu_S \neq 0.$$

The behavior of the thermodynamic quantities in condition A are shown in Fig. 2.3a and 2.4a using the HRGM, both have the same pattern as T increases. In this condition, the hadrons have no dependence on chemical potentials, hence the two quantities increase with temperature.

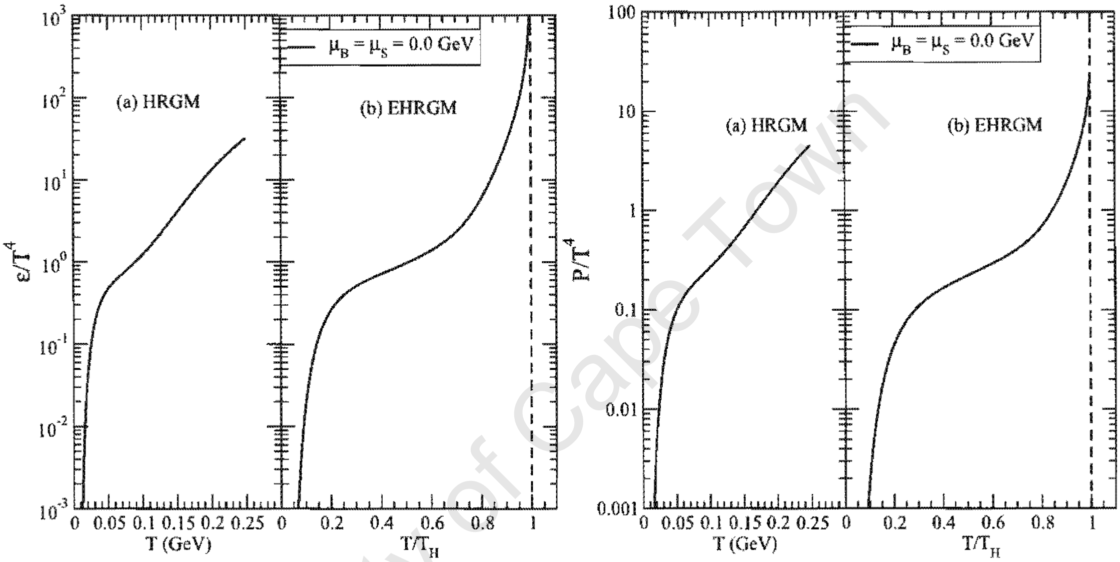

Figure 2.3: (a) The energy density, ε, and pressure, P, in units of T^4 calculated using the HRGM as a function of the temperature T at $\mu_B = \mu_S = 0$ GeV. (b) The energy density, ε, and pressure, P, in units of T^4 for EHRGM as a function of the temperature scaled by the Hagedorn temperature T_H.

Similarly, in Fig. 2.5a, the specific heat capacity is scaled by the temperature ε/T shows different temperature dependence from Fig. 2.3a and 2.4a, it starts decreasing as T increases for HRGM, this is because of the energy density, ε is bigger than TC_v. The shape of the graphs shown in Fig. 2.3b - 2.5b show a sudden change and start to increase rapidly at a particular T. Hence, this happens at the Hagedorn temperature, T_H. In a similar way, these results have been also presented in [6, 69] with few hadron resonance gases and the shape of graphs shown are similar to our model.

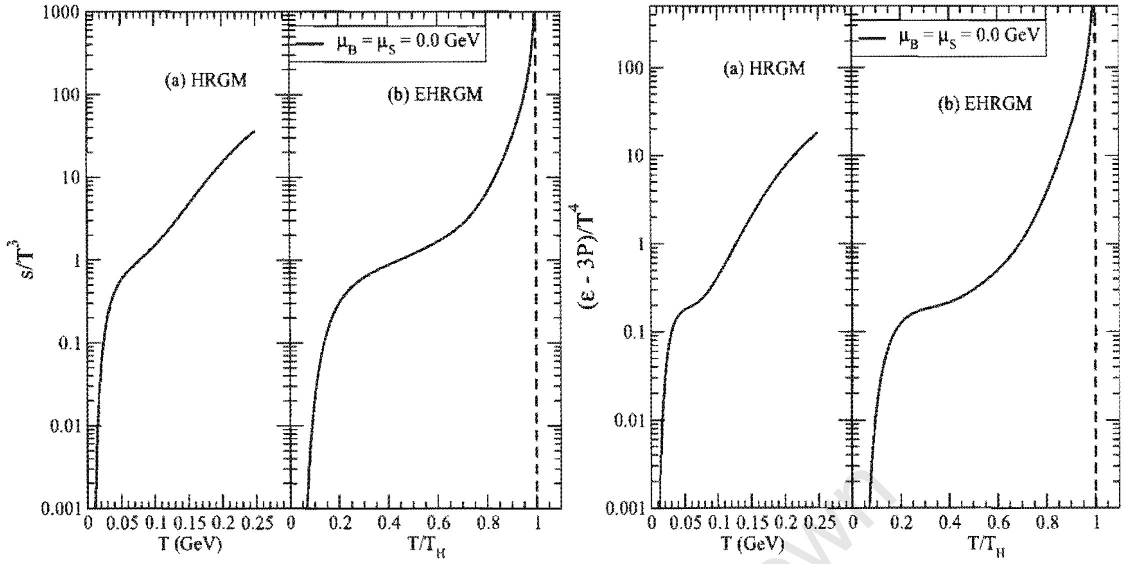

Figure 2.4: (a) The entropy density, s, in units of T^3 and interaction measure, $(\varepsilon - 3P)/T^4$ in units of T^4 calculated using the HRGM as a function of the temperature T at $\mu_B = \mu_S = 0$ GeV. (b) The entropy density, s, in units of T^3 and interaction measure, $(\varepsilon - 3P)/T^4$ in units of T^4 for EHRGM as a function of the temperature scaled by the Hagedorn temperature T_H .

In Ref [69] has been used this condition, in addition we have compared using the energy density behavior of the ideal resonance gas as shown in Fig. 2.3 with the results of ideal pion gas. From the Fig. 2.3b - 2.5b we observe that around $T/T_H \simeq 0.8$, resonances come significantly into play, so that $\varepsilon(T)$, $P(T)$, $s(T)$, $(\varepsilon(T) - 3P(T))$ and TC_V begin to increase until reach to T_H in these case the resonances provide the dominant part for the above-mentioned thermodynamic quantities.

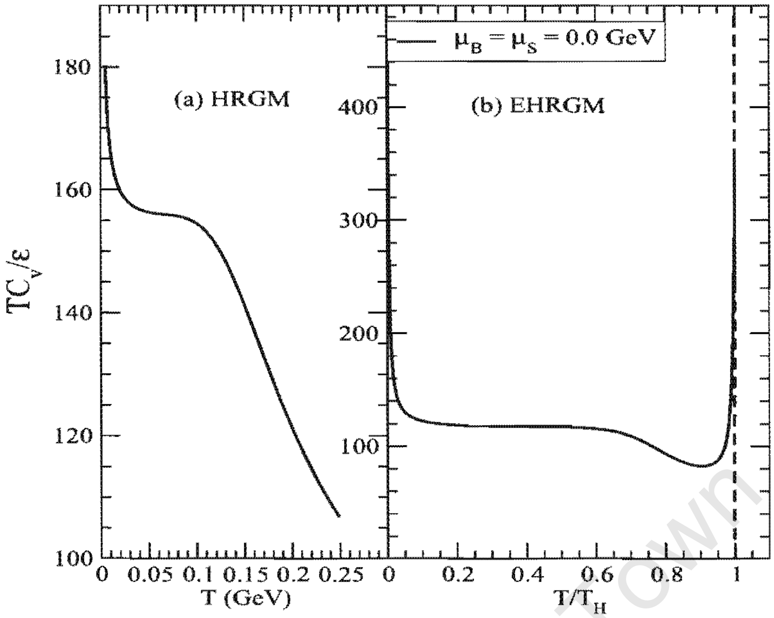

Figure 2.5: (a) The energy density TC_v/ε in units of ε calculated using the HRGM as a function of the temperature T at $\mu_B = \mu_S = 0$ GeV. (b) TC_v/ε in units of ε for EHRGM as a function of the temperature scaled by the Hagedorn temperature T_H .

With condition B, the strangeness conservation leads to zero strangeness density for all possible states of the matter produced in heavy ion collisions. Hence, with the HRGM, the behavior of graph for the thermodynamic quantities that are shown in Fig. 2.6a and 2.7a are similar to Fig. 2.3a and 2.5a, both have the same pattern as T increases, and become constant at higher temperature. Moreover, we observed that there are some changes on thermodynamic quantities compare to condition A and C; this shows that the two thermodynamic quantities increase for a finite number of temperature and baryon chemical potentials.

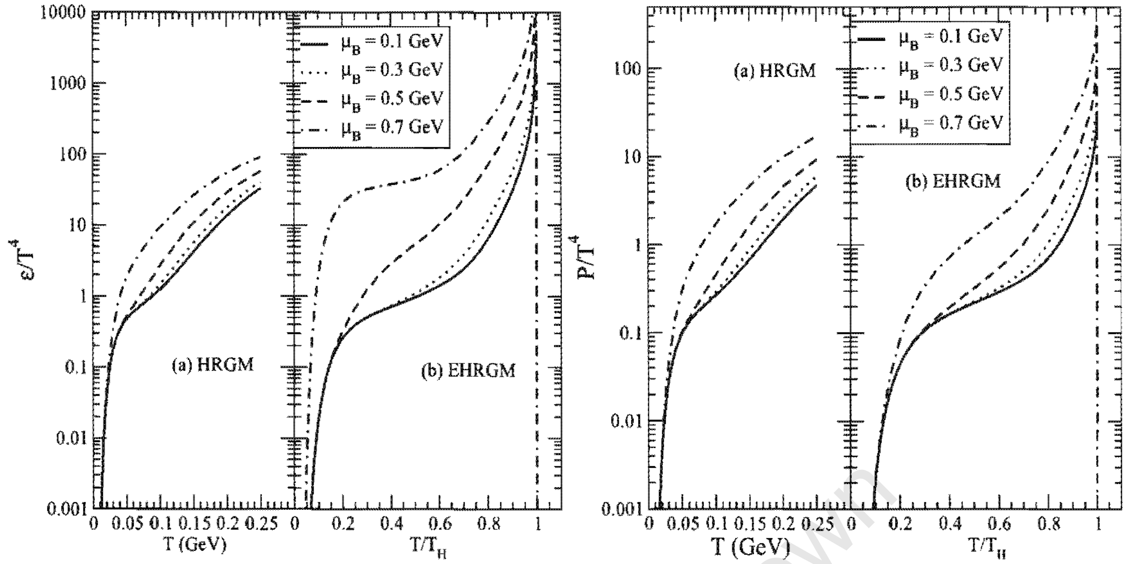

Figure 2.6: (a) The energy density, ε, and pressure, P, in units of T^4 calculated using the HRGM as a function of the temperature T for various μ_B and $\mu_S = 0$ GeV. (b) Energy density, ε, and pressure, P, in units of T^4 for EHRGM as a function of the temperature scaled by the Hagedorn temperature T_H .

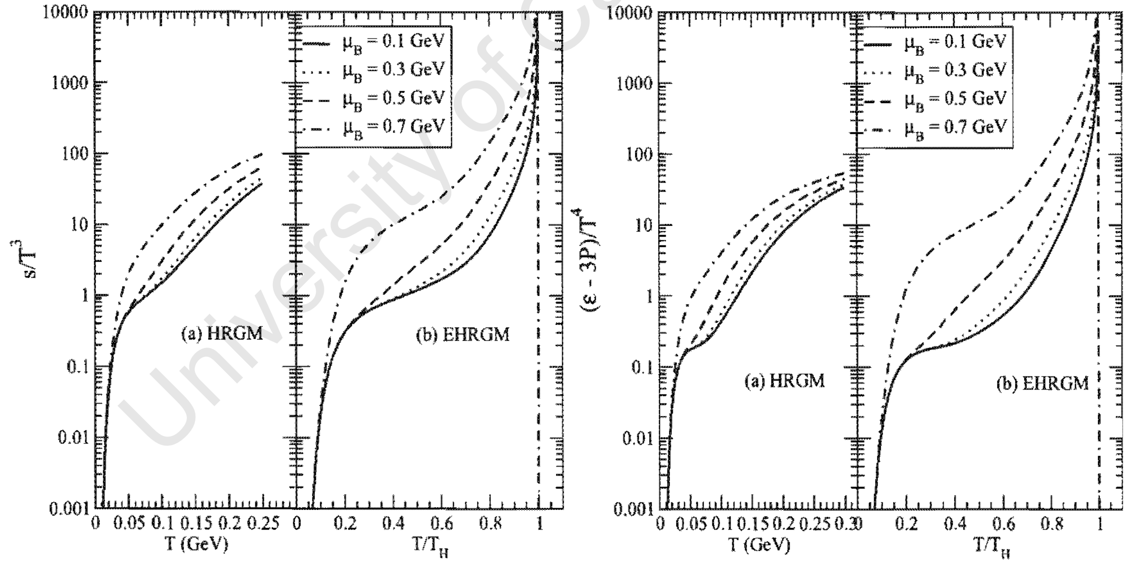

Figure 2.7: (a) The entropy, s, in units of T^3 and interaction measure, $(\varepsilon - 3P)/T^4$, calculated using the HRGM as a function of the T for various μ_B and $\mu_S = 0$ GeV. (b) The entropy, s, in units of T^3 and interaction measure, $(\varepsilon - 3P)/T^4$, using EHRGM as a function of the T.

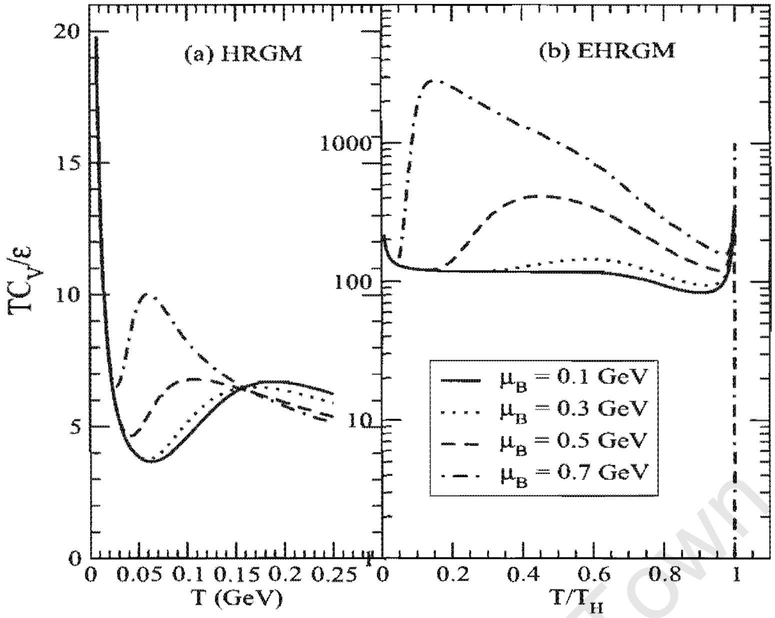

Figure 2.8: (a) TC_v/ε calculated using the HRGM as a function of the temperature T for various value of μ_B and with $\mu_S = 0$ GeV. (b) TC_v/ε for the EHRGM as a function of the temperature scaled by the Hagedorn temperature T_H.

Similarly, in Fig. 2.8a, the specific heat capacity is scaled by the temperature ε/T shows different from the two quantities, it starts decreasing as T increases for HRGM. However, the shape of the graphs shown in Fig. 2.6b - 2.8b) suggests that there is a sudden change and increments for the thermodynamic quantities even though T is fixed, this is also shown in Fig. 2.3b - 2.5b. This condition has been discussed in [77], using the energy density and pressure behavior of the hadronic gas as a function of the hadronic temperature and baryon chemical potential as shown in Fig. 2.6, where it is compared to that of the detonation transition from a supercooled quark-gluon plasma. Hence, these Fig. 2.6b - 2.8b lead us the existence of a sharp front separating the hadronic and quark-gluon plasma phases.

With condition C, using HRGM, the behavior of graph for the thermodynamic quantities that are shown in Fig. 2.9a and 2.10a are similar to Fig. 2.3a, 2.5a, 2.6a and 2.8a, both have the same pattern as T increases for finite value and then becomes constant even though T increases. Now, the hadrons are at nonzero chemical potentials, μ_B and μ_S, these show that the ε, P and s quantities increase for a finite temperature, baryon chemical potential and strangeness chemical potentials. Increasing μ_B made the thermodynamic quantities to raise more compare to condition A and B.

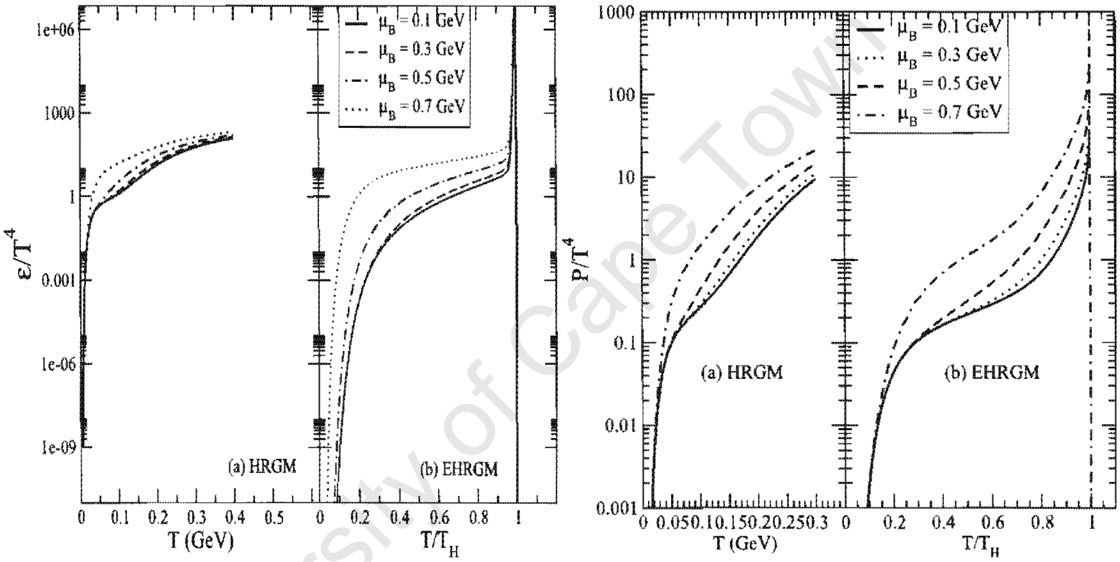

Figure 2.9: (a) The energy density, ε, and pressure, P, in units of T^4 calculated using the HRGM as a function of the temperature T for various value of μ_B and μ_S. (b) Energy density, ε, and pressure, P, in units of T^4 for EHRGM as a function of the temperature scaled by the Hagedorn temperature T_H .

Using HRGM as shown in Fig. 2.11a, the specific heat capacity decrease as T increases. However, the contribution from chemical potentials made to increase slightly at a higher chemical potentials. Moreover, the Fig. 2.9b - 2.11b have the same approach to Fig. 2.3b - 2.11b at a particular temperature.

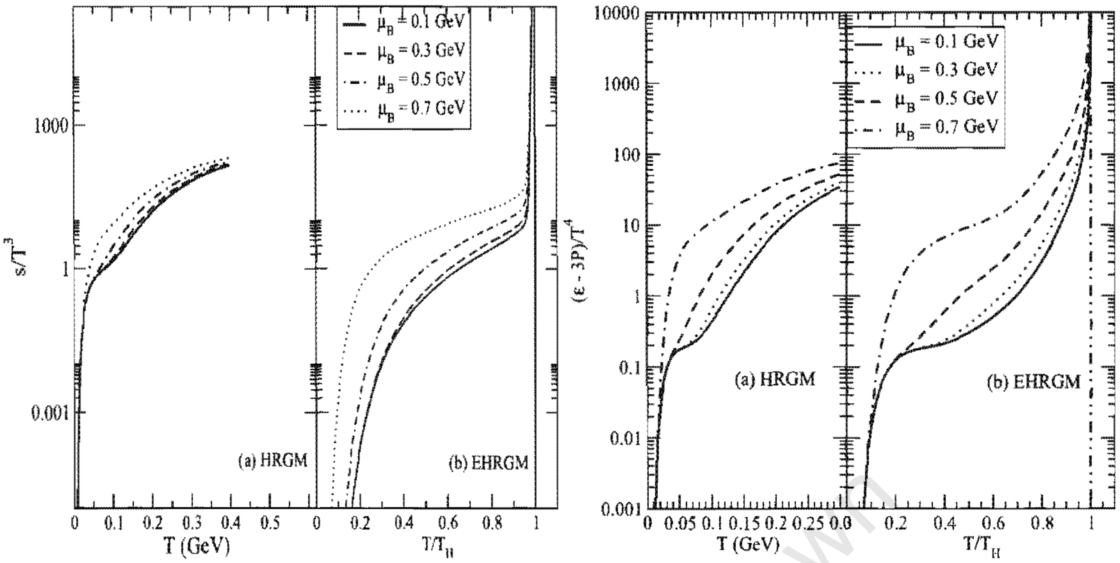

Figure 2.10: (a) The entropy density, s, in units of T^3 and variation measure, $(\varepsilon - 3P)/T^4$ calculated using the HRGM as a function of the temperature T for various μ_B and μ_S. (b) The entropy density, s, in units of T^3 and interaction measure, $(\varepsilon - 3P)/T^4$ in units of T^4 for EHRGM as a function of the temperature scaled by the Hagedorn temperature T_H .

The value of the squared speed of sound, C_s^2 remains well below the ideal-gas limit for massless particles $C_s^2 = 1/3$. The speed of sound is analyzed at the temperature range from 10 MeV to 250 MeV. The Fig. 2.12a; presents the result using HRGM for zero chemical potential. It is also compared this result with the EHRGM as shown in Fig. 2.12b. Similarly, the results in Fig. 2.12b and 2.13b show that when the transition point is crossed, in the case of full QCD, we expect as before that C_s^2 should vanish beside that C_s^2 is inversely proportional to the specific heat, C_v and this can lead to a divergence at the critical temperature T_H. Of course, due to finite volume effects, the velocity of sound will most likely not completely vanish at $T = T_H$.

The speed of sound versus the temperature results are presented in Fig. 2.12b and 2.13b, we evaluate $dP/d\varepsilon$ following [77] and first express P and ε in physical units, using EHRGM in Eq. 2.4. The temperature and chemical potential dependence of all the relevant thermodynamic quantities show unique behavior at the critical point, T_H specially for the speed of sound, there is

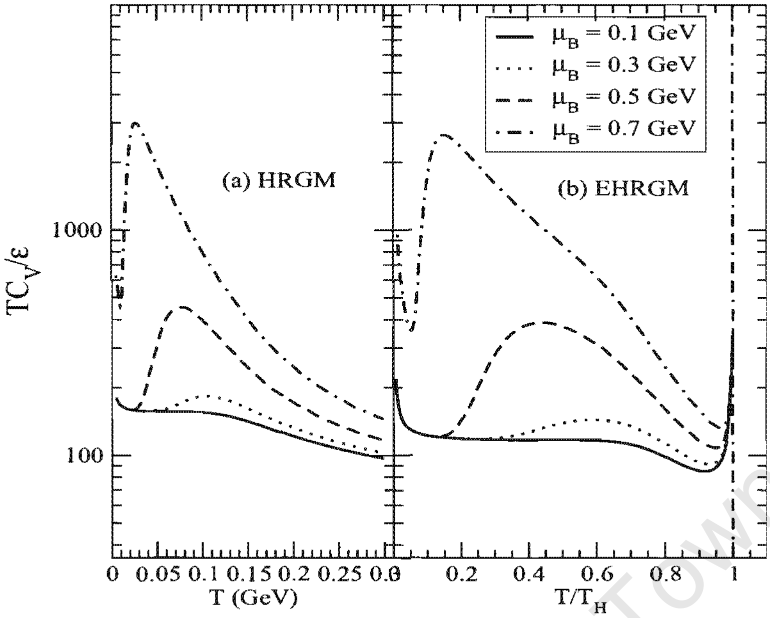

Figure 2.11: (a) TC_v/ε in units of ε calculated using the HRGM as a function of the temperature T for various μ_B and μ_S. (b) TC_v/ε in units of ε for EHRGM as a function of the temperature scaled by the Hagedorn temperature T_H .

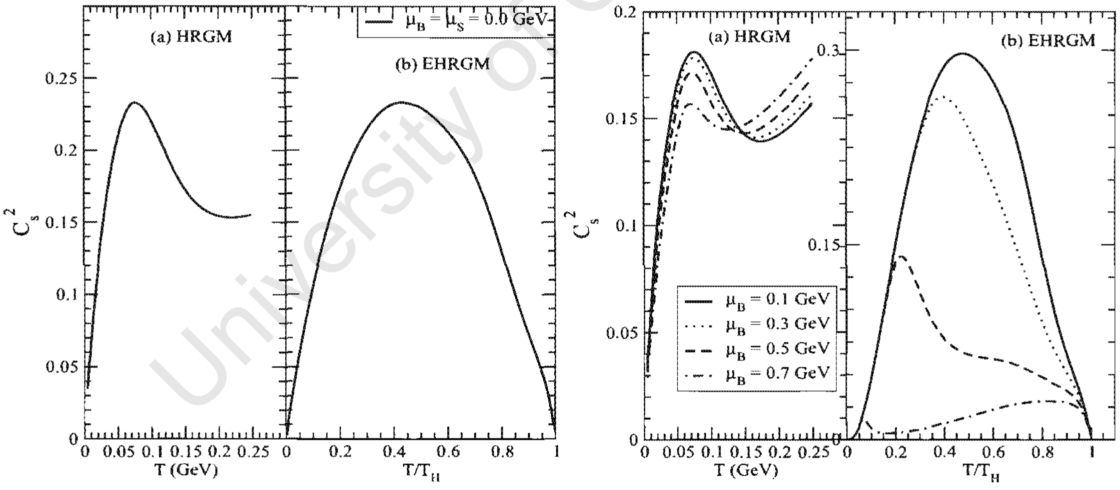

Figure 2.12: (a) Squared speed of sound $C_s^2(T,\mu)$ calculated using the HRGM as a function of the T with $\mu_B = \mu_S = 0$ GeV, for various value of μ_B but $\mu_S = 0$ GeV. (b) $C_s^2(T,\mu)$ in EHRGM with resonance mass truncated at $m < 2$ GeV.

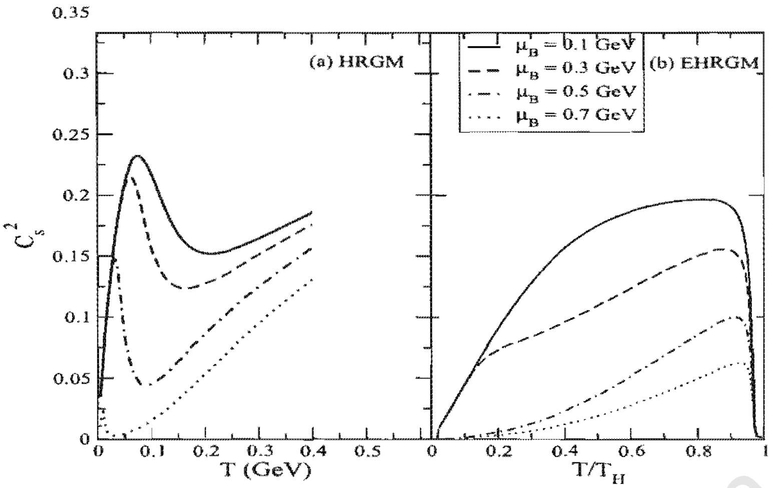

Figure 2.13: (a) Squared speed of sound $C_s^2(T,\mu)$ calculated using the HRGM as a function of the T, for various value of μ_B and μ_S. (b) $C_s^2(T,\mu)$ in EHRGM with resonance mass truncated at $m < 2$ GeV.

a pronounced dip as evidence for the phase transition in the system. Based on our calculations, the velocity of sound at $T = T_H$ is different from zero; it is expected to become zero but due to finite volume effects. The thermodynamic quantities using EHRGM as shown in Figs. 2.3b - 2.13b have singular point at T_H. However, the lattice QCD result [82] showed that at the critical temperature of QCD (say the crossover temperature), is the possible non-singular behavior in agreement with lattice calculations and this clearly favours HRGM as there is a minimum and the speed of sound never vanishes.

In general, the thermodynamic variables obtained using HRGM, are shown in Fig. 2.3a - 2.13a. At the T_H any sudden change of the value thermodynamic variables was not observed, but it showed smooth shape as the temperature goes beyond T_H. However, using the EHRGM one observe a different behavior than HRGM specially at the critical temperature T_H, as shown in Fig. 2.3b - 2.13b. This shows that if the system undergoes a first-order phase transition, both temperature and pressure remain constant as the hadronic matter is converted from hadron gas to a quark-gluon plasma; the energy and entropy density, however, change discontinuously. This leads to a new state of matter. The vertical dashed line in figures Fig. 2.3b - 2.13b are the result of the EHRGM that account for all mesonic and baryonic resonances.

2.7 Summary

We presented the HRGM, which is used to investigate the thermodynamic properties of hadrons, we further extend the HRGM by involving the Hagedorn spectrum, which is called EHRGM and then analyze the results. The Hagedorn temperature, T_H is determined from the number of hadronic resonances including all mesons and baryons. This leads to a stable result $T_H = 174 \pm 11$ MeV consistent with the critical and the chemical freeze-out temperatures at zero chemical potential [19]. Based on this result, we calculated the speed of sound and other thermodynamic quantities using HRGM and EHRGM for a wide range of baryon chemical potentials following the chemical freeze-out curve. Partly, the results that are presented in this chapter have been compared with other papers [6, 69].

Chapter 3

Extensions of THERMUS

This chapter describes additions to the THERMUS code [8] including charm and bottom hadrons. We briefly state the formalism using the statistical thermal model, explain how to implement THERMUS with the updated particle data table, compare results with reference [22], and present the study of particle yields of the Au-Au collision at 200 GeV [83, 84, 85, 86] and and particle ratios for various hadron species at LHC experiments (p-p collisions at 900 GeV and 7 TeV as well as Pb-Pb collision at 2.76 TeV) [11, 12, 13], for these energies THERMUS considers along the freeze-out curve [5, 63, 64].

3.1 Review of THERMUS

THERMUS is a package of C++ classes and functions allowing statistical thermal model analyzes. It is written by S. Wheaton [8] to be used within the ROOT [87] framework of analysis. The statistical thermal model assumes a hadron gas at chemical freeze-out.

There are other codes, e.g., the Statistical Hadronization with Resonances (SHARE) [88], which is also a collection of programs designed for the statistical thermal analysis of particle production in relativistic heavy ion collisions. With the input of intensive statistical parameters, it generates ratios of particle abundances. Another successful code is the Therminator: Ther-

THERMUS has three distinct thermal model formalisms. The first is grand-canonical ensemble, where baryon number (B), strangeness (S), charge (Q), charm (C) and bottom (b) are conserved on average. The next formalism is a strangeness-canonical ensemble in which strangeness is exactly conserved, while B, Q, C and b are treated grand-canonically, finally, a canonical ensemble in which B, S and Q are conserved exactly. Furthermore, it takes into account decay chains and detector efficiencies. These enable sensible fitting of model parameters to experimental data.

The source code of the THERMUS package is available in [8] and has been extended by S. Wheaton so that additional quantum numbers can be included in the code [1]; note that most of the additional particles are charm and bottom with the corresponding decay elements. It can treats charm and bottom grand-canonically. First, we will mention and state the statistical formalism for the extension of THERMUS, then proceed to explain how to use the 2008 particle data table and discuss the results and compare with previous results [22].

3.2 The Statistical Formalism

The hadron gas partition function contains all the thermodynamic information of the system. The choice of partition function depends on the statistical ensemble. Next, we shall use the grand-canonical ensemble in this chapter *and implement it with the 2008 particle data table in THERMUS.*

In the grand-canonical ensemble, there are several parameters to characterize the system. These are temperature, chemical potential, volume and non-equilibration factors. The hot dense matter produced in nucleus-nucleus collision is large enough to be described by the grand-canonical ensemble.

---

[1] The extended source code was written by S. Wheaton.

In the grand-canonical ensemble, energy and quantum numbers are conserved on average through the temperature, T and the chemical potentials, μ. The logarithm of the total partition function for a multi-component hadron gas of volume V and temperature T is given by

$$\ln Z^{GC}(T, V, \mu) = \sum_i \frac{g_i V}{(2\pi)^3} \int d^3p \ln\left(1 \pm e^{-\beta(E_i-\mu_i)}\right)^{\pm 1}. \qquad (3.1)$$

where g_i and μ_i are the degeneracy and chemical potential of hadron species i, $\beta \equiv 1/T$, while $E_i = \sqrt{p^2+m_i^2}$, with m_i being the particle mass. The plus sign refers to fermions and the minus sign to bosons.

In this ensemble, we considered the conservation of the quantum numbers i.e., B, S, Q, C and b. The chemical potential for hadron species i is given by

$$\mu_i = B_i\mu_B + S_i\mu_S + Q_i\mu_Q + C_i\mu_C + b_i\mu_b, \qquad (3.2)$$

where B_i, S_i, Q_i, C_i and b_i are the baryon, strangeness, charge, charm and bottom number, respectively, and μ_B, μ_S, μ_Q, μ_C and μ_b are the corresponding chemical potentials for the conserved quantum numbers. This ensemble is widely used in applications to heavy ion collisions [90, 96, 97, 98, 99, 100, 101, 102]. The fugacity for each of these chemical potentials is defined as $\lambda \equiv e^{\mu/T}$.

The density of hadron species i with quantum numbers B_i, S_i, Q_i, C_i and b_i, spin-isospin degeneracy factor g_i, and mass m_i, emitted directly from a fireball at temperature T is

$$n_i(T, \{\mu\}, \{\gamma\}) = g_i \int \frac{d^3p}{(2\pi)^3} \left[\gamma_T \lambda_T e^{\sqrt{m_i^2+p^2}/T} \pm 1\right]^{-1}, \qquad (3.3)$$

where

$$\{\mu\} = \{\mu_B, \mu_S, \mu_Q, \mu_C, \mu_b\}, \quad \{\gamma\} = \{\gamma_s, \gamma_c, \gamma_b\}, \quad \gamma_T = \gamma_s^{-|S_i|}\gamma_c^{-|C_i|}\gamma_b^{-|b_i|}.$$

The chemical potentials μ_S, μ_Q, μ_C and μ_b are typically constrained in applications of the model by the initial strangeness, baryon-to-charge ratio, charm and bottom.

3.3 Extended THERMUS Particle Set

As mentioned earlier, in the extended particle data table (2008 particle data table), the charm and bottom hadrons are included. Thus, we will make a comparison with the previous THERMUS particle data table (2002 particle data table). When we look at the number of states for the two particle data tables as shown in Figs. 3.1 and 3.2 respectively, we count how many resonances exist in the intervals (0, 0.2), (0.2, 0.4), (0.4, 0.6),...,(10.0, 11.1) GeV and then plot these numbers with respect to mass (the mass is defined as the center of the interval).

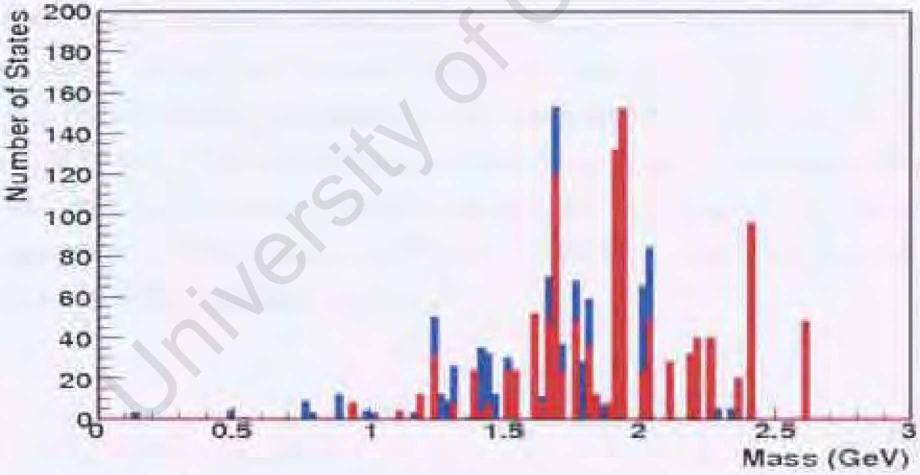

Figure 3.1: The number of states for hadron particle data table arranged in terms of their masses, included are baryons (red) and mesons (blue) with u, d and s quarks up to 2.6 GeV $N(2600)^+$ `$THERMUS/particles/PartList_PPB2002.txt` [22]

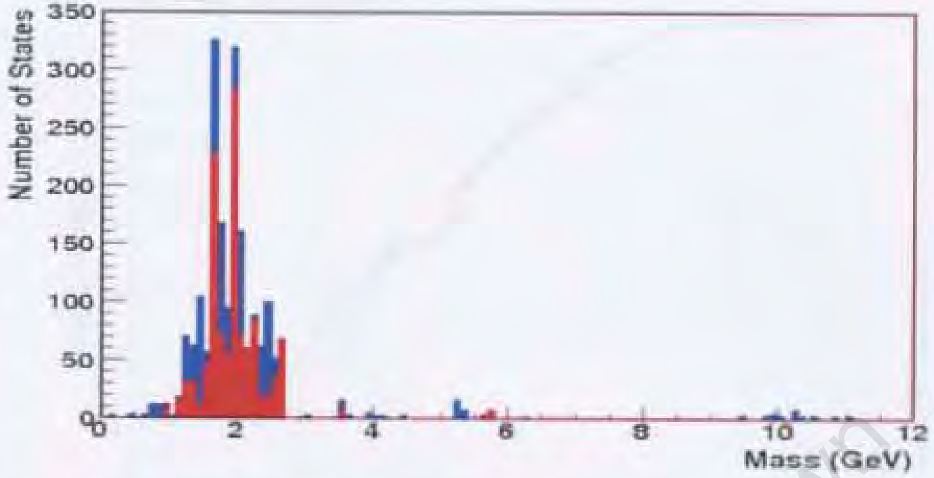

Figure 3.2: The number of states for particle data table arranged in terms of their masses. This is the updated THERMUS particle data table, it includes the c and b quarks up to 11.019 GeV, $\Upsilon(11020)^0$ `$THERMUS/extended_particles/PartList_PPB2008_CB.txt` (blue: mesons, red: baryons).

In addition to the first method, we presented in Figs. 3.1 and 3.2, to observe the difference between the two particle data tables and their number of states, also applied a second method to show their difference; that is, we add the number of resonances in the intervals (0, 0.2), (0, 0.4), (0, 0.6), ..., (0, 11.1) GeV. Then, plot these numbers versus mass (the mass is defined as the center or the upper value of the interval) as shown in Fig. 3.3 and 3.4 respectively. These plots are clearer to notice the difference from the first method as we presented in Fig. 3.1.

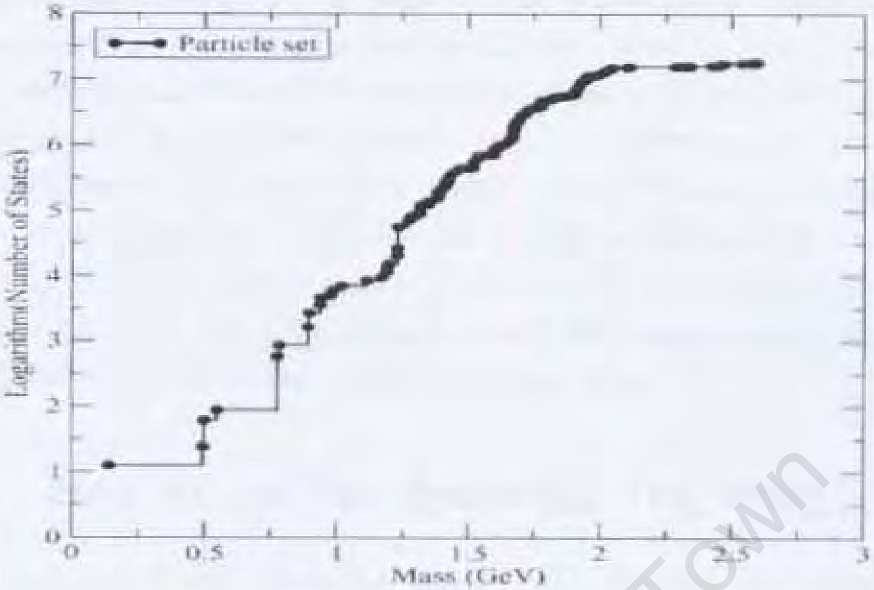

Figure 3.3: Logarithm of the number of states for particle data table which is found in `$THERMUS/particles/PartList_PPB2002.txt` [22] in terms of their masses.

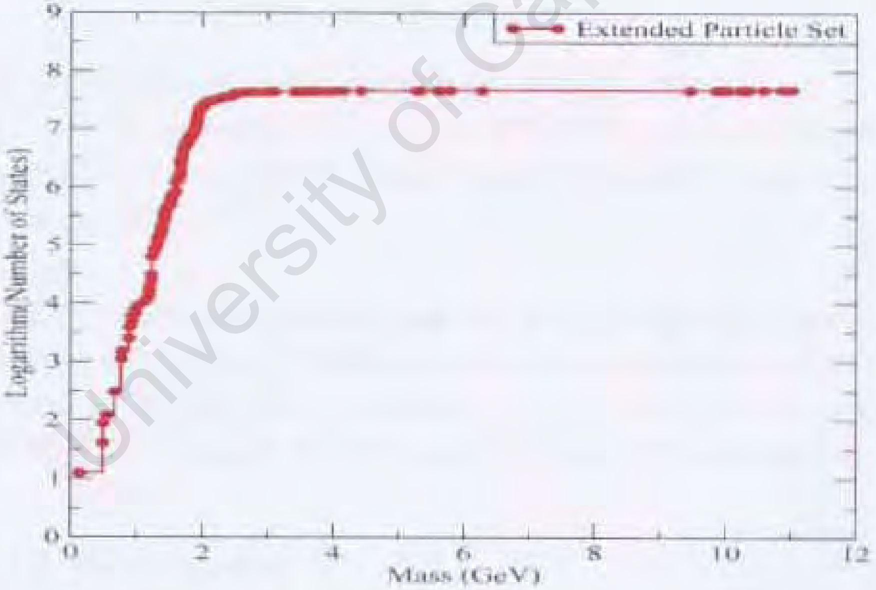

Figure 3.4: Logarithm of the number of states for particle data tables which is found in `$THERMUS/extended_particles/PartList_PPB2008_CB.txt` in terms of their masses.

From Figs. 3.2 and 3.4, the number of states and the corresponding logarithm increased from the previous particle data table. In Figs. 3.1 and 3.3, these changes come from the contributions of charm, bottom and newly included resonances in the 2008 particle data table. Furthermore, the empty gap as shown in Fig. 3.4 between 6 GeV - 9.5 GeV have not filled in by recent experiments. The responsible for this empty gap might be due to the detectors have seen those particles in order to fill in the empty gap. Based on these highlights, we will discuss the method to implement the extension of THERMUS based on the 2008 particle data table.

3.4 How to use The Extended THERMUS?

In this section, we will outline how to use THERMUS with the 2008 particle data table. Three distinct statistical ensembles are included in THERMUS, and the additional options to include quantum statistics, resonance width and excluded volume corrections are also available.

THERMUS has a default particle list which includes all mesons (up to the $\Upsilon(11020)^0$, previously, it was up to $K_4^*(2045)$) and baryons (up to the Ξ_b^0, previously, it was up to Ω^-) listed in the 2002 and 2008 Particle Physics Booklets [9, 104].

THERMUS has been tested using the 2008 particle data table and the decay files. The `TTMParticleSet` constructor now takes an additional argument `Bool_t CB_Included` which must be set to true. Here is the format with THERMUS a particular example of Ξ_b^- from 2008 particle data table:

```
root [1] TTMParticleSet
set("$/THERMUS/extended_particles/PartList_PPB$2008$_CB.txt",true)
root [2] set.InputDecays("$/THERMUS/extended_particles/",true)
root [3] TTMParticle *part = set.GetParticle(5232)
root [4] part->List()
```

```
********* LISTING FOR PARTICLE Xib- *********

 ID   = 5232   // Particle ID

 Deg. = 2      // degeneracy

 STAT = 1      // Fermi-Dirac statistics

 Mass      = 5.7924 GeV
 Width     = 0 GeV
 Threshold = 0 GeV

 Hard sphere radius = 0

 B =  1                             // B = Baryon
 S = -1             |S| = 1         // S = Strange
 Q = -1                             // S = Charge
 Charm  = 0         |C| = 0         // C = Charm
 Beauty = -1        |b| = 1         // b = Beauty
 Top    = 0         |T| = 0         // T = Top
           STABLE
**********************************************
```

The first line, `root [1]` loads the 2008 particle data table; the second line, `root [2]` loads the input decays of the 2008 particle data list. The third, `root [3]` and fourth, `root [4]` can get particles from the 2008 particle data table and lists the particle respectively [22]. The latest version of the THERMUS package with both particle data tables is found in this link: `http://www.phy.uct.ac.za/courses/staffwebsites/wheaton/THERMUS/SourceDownload.html`.

3.5 Results and Discussions

This section presents results based on the 2008 particle data table and makes comparisons with results obtained using the 2002 particle data table. Note that the 2008 particle data table has not yet been implemented to be used for the other two ensembles, (the canonical and strangeness-canonical ensembles). In this chapter, all calculations use the grand-canonical ensemble.

The emphasis of our investigation is to establish quantitatively the similarities and differences in the production and contributions of particles observed in the elementary and heavy ion collisions. In the following subsection using THERMUS, we will discuss and analyze hadron particle yields and ratios as well as obtain the corresponding thermodynamic parameters with both particle data tables based on THERMUS fit.

3.5.1 Thermodynamic Parameters Analysis

We analyze the RHIC [83, 84, 85, 86] and LHC [11, 12, 13] results using THERMUS, and compare the results for both particle data tables. THERMUS fits the experimental data in order to obtain the thermodynamic parameters.

We present results from the STAR experiment for Au-Au collisions at 130 and 200 GeV. The data has been used and analyzed previously in [105, 106, 10]. Our results using the STAR densities at mid-rapidity for various hadron species in the centrality region $(0-6\%)$ for Au-Au collisions at 130 GeV are shown in Fig. 3.5 (a) and (b). Similarly, the results at 200 GeV are shown in Fig. 3.6 (a) and (b). In these figures, the $K^{\pm}$, p, and $\bar{p}$ yields are given in [83, 84], while all other particles are derived from the measured values by *centrality interpolations* [2] described in reference [10] Section II A; these are $\pi^{\pm}$, ϕ, Λ, $\bar{\Lambda}$, Ξ^- and $\bar{\Xi}^+$.

Similarly, Fig. 3.6 (a) and (b) show STAR rapidity densities of various hadrons in Au-Au collisions at 200 GeV at centrality $(0-6)\%$ [10]. The experimentally measured values have been obtained from references [86, 107, 108]. The STAR data for p and $\bar{p}$ rapidity densities also include weak feeding from (multi-)strange hyperons [86]. The comparison between the model and STAR particle yields are presented in Figs. 3.5 and 3.6.

---

[2] Particle rapidity densities are sometimes measured in specific centrality windows which are different for various experiments. Hence, to perform an appropriate analysis of the full data set, one has to find a proper method in order to estimate rapidity densities for various hadronic species *in the same centrality* window.

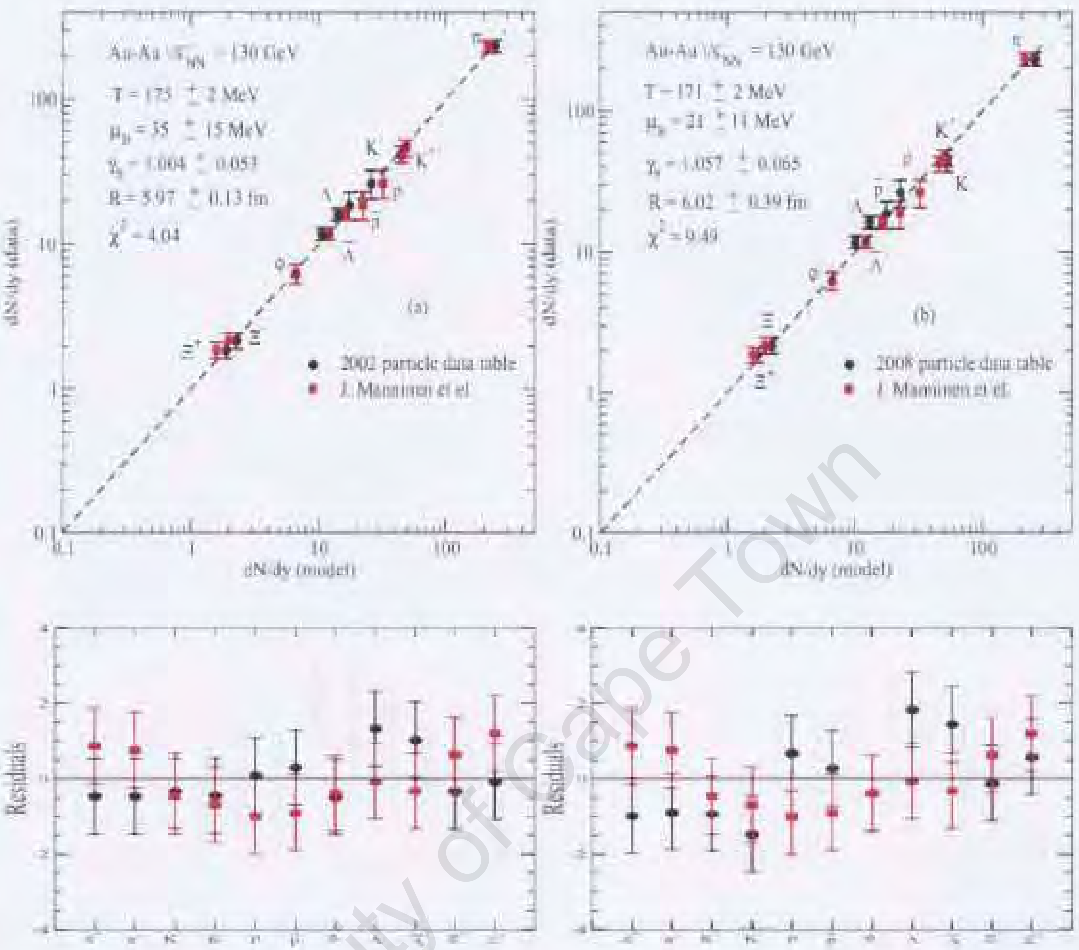

Figure 3.5: Figure (a) and (b) showing the comparison between rapidity densities in the combined fit and rapidity densities measured by STAR [10] for central Au-Au collision at 130 GeV and the corresponding thermal fit parameters are given for both particle data tables. Similarly, the comparison between rapidity densities in the combined fit and rapidity densities in terms of the residuals are presented for both particle data tables.

As presented in Fig. 3.5, THERMUS fits very well compared to [10]. However, the Λ's were underestimated by 16% compared to [10]. Similarly, Fig. 3.6 fits very well the STAR data [10] except φ's were underestimated by 18%. We have compared particle yields between the experimental and model fit values using the residual statistics [10].

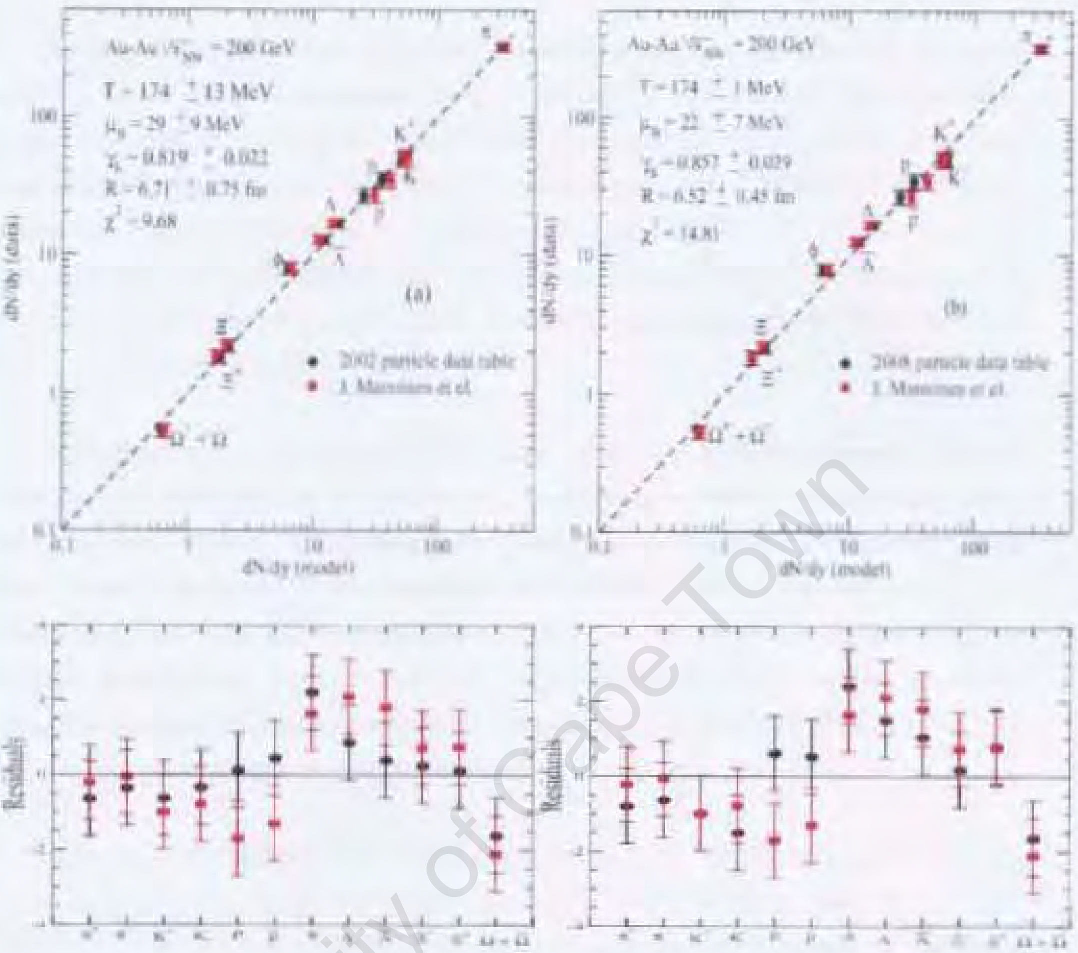

Figure 3.6: Figure (a) and (b) showing the comparison between rapidity densities in the combined fit and rapidity densities measured by STAR [10] for central Au-Au collision at 200 GeV and the corresponding thermal fit parameters are given for both particle data tables. Similarly, the comparison between rapidity densities in the combined fit and rapidity densities in terms of the residuals are presented for both particle data tables.

The residual is defined as the ratio between the difference in Experiment (E) and Model (M) value and the experimental error value (R), i.e.,

$$\texttt{Residual} = \frac{\texttt{E} - \texttt{M}}{\texttt{R}}. \tag{3.6}$$

Using Eq. (3.6), we compare the particle yield results for both particle data tables with the experimental results for Au-Au collisions at 130 GeV and 200 GeV. The results are presented in Figs. 3.5 and 3.6.

The available data from RHIC experiment for Au-Au collisions at 130 GeV and 200 GeV [10] were compared with THERMUS. The particle yields for various hadron species and the thermodynamic parameters are given for both particle data tables in Figs. 3.5 and 3.6. The Fits to STAR data at 130 and 200 GeV show almost no difference between the experiment and THERMUS. Furthermore, we have removed some hadron species (for exampleΛ's and ϕ) from the fits in order to obtain a best fit; and the resulting fit thermodynamic parameters were modified slightly within the errors of the parameters.

According to results in Figs. 3.5(b) and 3.6(b), the results obtained with the 2008 particle data table show smaller freeze-out temperatures than the 2002 particle data table. Clearly, this is caused by increasing the radius of the system, which then causes a decrease of the freeze-out temperature. Thus, the variation of the radius obtained from the fit contributes greatly to the difference between the two particle data tables. This also makes a contribution to changing the freeze-out temperature and other thermodynamic parameters. In addition, THERMUS best fit parameters at chemical freeze-out results are different from [10].

In general, the results presented in Figs. 3.5 and 3.6, THERMUS overestimates most of the particle yields and underestimates Λ and ϕ yields at 130 and 200 GeV; THERMUS fits the experimental particle yield very well. in addition, we presented the residual analysis for both particle data tables and compared with experimental values in Figs. 3.5 and 3.6. Most of our residual results are in the range -1 to 1 within the error bar; therefore, THERMUS results give a better fit to the RHIC experimental data than those explained in [10].

Based on the ALICE central rapidity densities for the p-p collisions at 900 GeV and 7 TeV [11, 12, 13] for different hadron species, the corresponding predicted values are shown in Figs. 3.7 and 3.8. Based on the results shown in the Figs. 3.7 and 3.8, we noticed that the thermal fit parameters were also different for both particle data tables. However, the predicted particle ratios show similar results for both particle data tables.

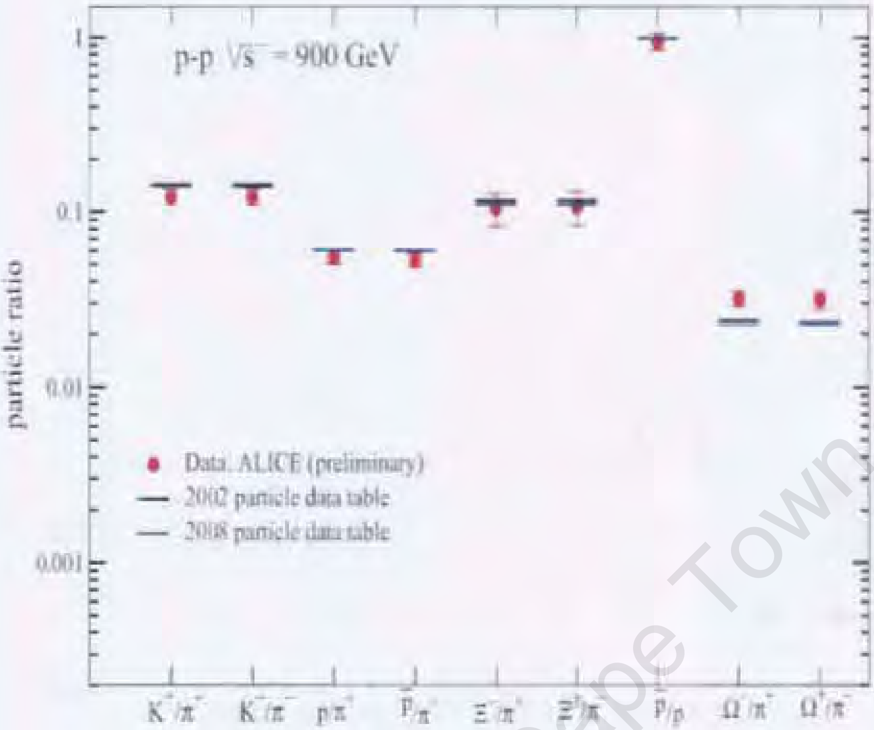

Figure 3.7: Particle yield results using the two particle data tables for the rapidity densities of the preliminary measured results from ALICE [11, 12, 13] for central p-p collision at 900 GeV. The thermal fit parameters are listed in Table 3.1.

Our results are presented in Figs. 3.7 and 3.8 for the particle ratios of the preliminary LHC results of the p-p collisions at 900 GeV and 7 TeV. The corresponding fitted thermodynamic parameters are listed in Tables 3.1 and 3.2. In conclusion, the thermal fit results from p-p collisions at 900 GeV and 7 TeV are in good agreement with THERMUS. The particles containing strangeness particles such as Ξ/π, Ω/π and Ω/Ξ were not fitted well compared to other particle ratios.

The particle yields for the preliminary measured results of the heavy ion experiment, Pb-Pb collision at 2.76 TeV [13] were calculated using THERMUS. The calculated particle ratios for different hadron species are presented in Fig. 3.9. Based on the results shown in Fig. 3.9, the thermal fit parameters were different for both particle data tables. However, the predicted particle yields are similar.

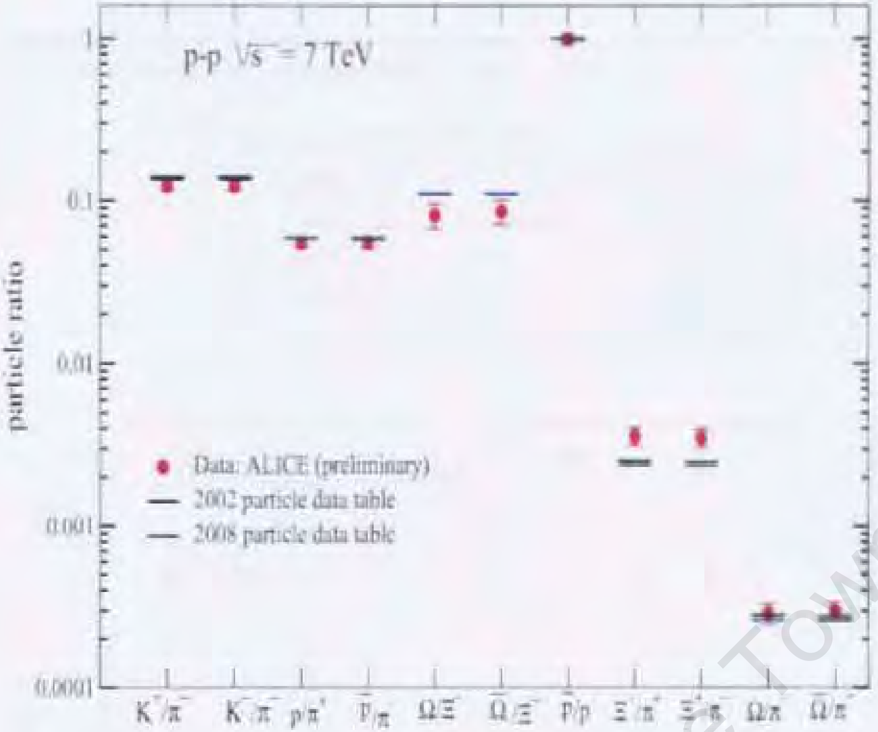

Figure 3.8: Particle yield results for the two particle data tables for the rapidity densities of the preliminary results by ALICE [11, 12, 13] for central p-p collision at 7 TeV. The fit results were obtained from THERMUS 2002 and 2008 particle data tables. The thermal fit parameters are listed in Table 3.2.

Table 3.1: The predicted thermal fit parameters for p-p collision at 900 GeV on ALICE [11, 12, 13]. The fit results were obtained from both THERMUS particle data tables (where THERMUS 2002 particle data table, Fit (2002) and THERMUS 2008 particle data table, Fit (2008)).

Parameters	Fit (2002)	Fit (2008)
T (GeV)	0.152 ± 0.002	0.154 ± 0.002
μ_B (GeV)	0.001 (fixed)	0.001 (fixed)
μ_S (GeV)	0.0	0.0
μ_Q (GeV)	0.0	0.0
γ_s	0.733 ± 0.041	0.707 ± 0.042

Similarly, using the preliminary particle yield results for Pb-Pb collision at 2.76 TeV [12, 13], we have presented our fit results in Fig. 3.9. The fitted thermodynamic parameters are listed in Table 3.3. In addition, the thermal fits are in good

Table 3.2: The predicted thermal fit parameters for p-p collision at 7 TeV on ALICE [11, 12, 13]. The fit results were obtained from the two particle data tables.

Parameters	Fit (2002)	Fit (2008)
T (GeV)	0.150 ± 0.002	0.152 ± 0.002
μ_B (GeV)	0.001 (fixed)	0.001 (fixed)
μ_S (GeV)	0.0	0.0
μ_Q (GeV)	0.0	0.0
γ_s	0.714 ± 0.023	0.697 ± 0.023

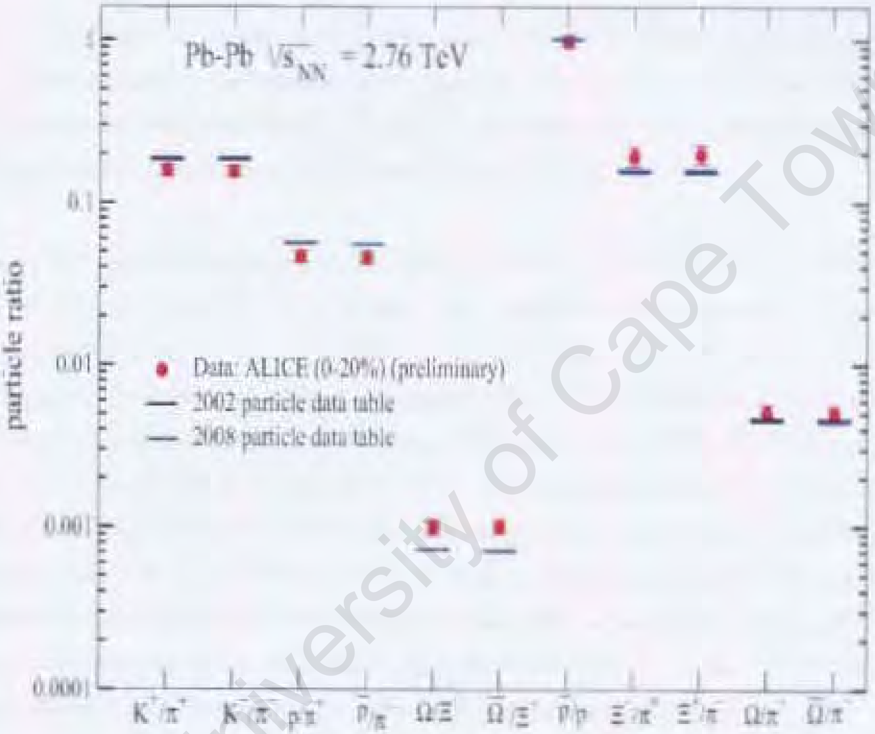

Figure 3.9: Particle yield results using two particle data tables for the rapidity densities from ALICE in central Pb-Pb collision at 2.76 TeV [12, 13].

agreement between the THERMUS and the preliminary results for all particles containing strangeness such as kaons and hyperons.

The recent experimental results at LHC for p-p collisions at 900 GeV and 7 TeV as well as Pb-Pb collision at 2.76 TeV [11, 12, 13] have been analyzed using

Table 3.3: The predicted thermal fit parameters for Pb-Pb collision at 2.76 TeV on ALICE [12, 13]. The fit results were obtained from both THERMUS particle data tables.

Parameters	Fit (2002)	Fit (2008)
T (GeV)	0.150 ± 0.001	0.152 ± 0.001
μ_B (GeV)	0.001 (fixed)	0.001 (fixed)
μ_S (GeV)	0.0	0.0
μ_Q (GeV)	0.0	0.0
γ_s	1.0 (fixed)	1.0 (fixed)

THERMUS. We have used preliminary results and analyzed the corresponding thermodynamic parameters from particle yield results. The fitted thermodynamic parameters are presented in Figs. 3.7, 3.8 and 3.9; the corresponding fitted thermodynamic parameters are given Tables 3.1, 3.2 and 3.3.

The thermal parameters obtained with the THERMUS fit to the experimental data for p-p and Pb-Pb collisions are stable in some ranges. In particular, the freeze-out temperature is between 150 MeV and 175 MeV while the beam energy changed over several orders of magnitude. This occurred over a wide range of energies, different collision systems and parameters. The freeze-out temperature, strangeness saturation factor, radius, baryon chemical potential and strangeness chemical potential have been well parameterized with small uncertainties. They have also been compared with [5, 109] as a function of energy. In many ways, this remarkable success in describing the data with a few simple statistical parameters can be viewed as an indication that the particles in these collisions were indeed produced in a thermally and chemically equilibrated system.

3.6 Summary

We have analyzed and discussed the hadron abundances measured in Au-Au, p-p and Pb-Pb collisions at RHIC and LHC experiments using THERMUS; our results for hadron abundances are in agreement with a thermally equilibrated system. The results were obtained with the 2002 and 2008 particle data tables and their differences have been explained in this chapter. In particular, the data from the RHIC experiment for Au-Au collisions at 130 GeV and 200 GeV have been discussed and analyzed. Similarly, using the preliminary particle ratios result in p-p collisions at 0.9 TeV and 7 TeV as well as Pb-Pb collision at 2.76 TeV, the particle yield predictions and thermodynamic parameters obtained from the fits have been presented.

THERMUS has also been used to describe the particle ratios using the two particle data tables. The 2008 particle data table can be used to perform more analysis of particle ratios for lighter and heavier hadron masses obtained from elementary and heavy ion collisions [9]. We have analyzed our results using the previous freeze-out curve parameters [5, 63, 64] for 2008 particle data table. Thus, THERMUS needs a new recalculation of the freeze-out curve in order to obtain a better thermal fit results than the present ones.

Chapter 4

Non-extensive Statistical Distribution

This chapter presents Tsallis thermodynamics [44, 110] using a non-extensive statistical distribution. It was first proposed in 1988 [44] by Tsallis who postulated a generalized form of the entropy. It discusses non-extensive quantum statistics in particular the generalization of the Bose-Einstein and Fermi-Dirac distributions by maximizing the entropy of the system for quantum distributions. The generalization to non-extensive statistics recovers the extensive, Boltzmann-Gibbs (BG) as a particular case.

In the next sections, we will discuss the theoretical background for non-extensive statistics with a mathematical derivation and show in detail the thermodynamic consistency. A particular form of the Tsallis distribution has been used recently to fit the transverse momentum distributions for identified particles by the STAR [14], PHENIX [15] at RHIC and by the ALICE [11, 13] and CMS [16] collaborations at the LHC. We have obtained the thermodynamic parameters using the experimental results from high energy elementary particle collisions [23, 45] and heavy ion collisions [11, 12, 16]. The Tsallis distribution has been used to extract the yields at mid-rapidity, average transverse momentum and thermodynamic parameters of the systems at the thermal freeze-out. An improved form of the Tsallis distribution in the particular case of relativistic quantum distributions is proposed for describing the transverse momentum distribution and fits are presented together with estimates of the parameter q and the temperature T [17, 18].

4.1 Theory of Non-extensive Statistics

There has been a growing tendency to use the non-extensive statistical formalism. From 1988 up to the present, numerous theories of statistical thermodynamics have been presented in the framework of the Tsallis formalism. It has been shown that this formalism is useful, because it provides a suitable theoretical tool to explain some of the experimental situations, where standard statistics seem to fail, the reasons are stated in detail in reference [110]. The postulated form of the generalized entropy is:

$$S_q \equiv \frac{1-\sum\limits_{i=1}^{W} P_i^q}{q-1}, \; (q \in \Re; \; \sum_{i=1}^{W} P_i = 1), \tag{4.1}$$

or, for continuum distributions

$$S_q \equiv \frac{1-\mathrm{Tr}\rho^q}{q-1}, \tag{4.2}$$

where q is a positive constant, P_i are the probabilities of microscopic states, and ρ the corresponding density operator. The parameter q is called non-extensivity parameter, entropic index or simply Tsallis parameter. It is a measure of the non-extensivity of the system of interest. There are continuous and discrete versions of this entropic index. The physical significance of q using Tsallis distribution. The true nature of the nonextensive parameter q in Tsallis statistics has not been fully understood yet by us. It is unclear under what circumstances, e.g. which class of nonextensive systems and under what physics situation, should Tsallis statistics be used for the statistical description. The understanding of the physical meaning of q has become crucially important in Tsallis statistics and its applications to the fields of high energy pysics. In this chapter, we discussed the properties of the nonextensive parameter q and the Tsallis distribution of the using thermodynamic consitency and deduce a mathematical expression of q based on the theory of the generalized Boltzmann equation. This new entropy formula recovers the usual BG entropy in the limit where q tends to 1 (the detailed derivation is found in appendix C.1). The reason that q is called the non-extensivity parameter is due to the following pseudo additivity rule; is given by

$$S_q(I+J) = S_q(I) + S_q(J) + (1-q)S_q(I)S_q(J), \tag{4.3}$$

where I and J are two independent systems in the sense that the system $I+J$ factorises into those of I and J. Since S_q is greater or equal to 0 for all values of q, we can say that $q<1$, $q=1$ and $q>1$ correspond to superextensivity (entropy of the whole system is greater than the sum of its parts or superadditive), extensivity (entropy is additive) and subextensivity (entropy of the whole system is smaller than the sum of its parts or subadditivity) respectively. Now, we want to prove Eq. (4.3). We start from the following definitions

$$S_q(I) = \frac{1-\sum\limits_i (P_i^I)^q}{q-1}, \tag{4.4}$$

and

$$S_q(J) = \frac{1-\sum\limits_j (P_j^J)^q}{q-1}, \tag{4.5}$$

by multiplying Eq. (4.4) and (4.5), we get

$$S_q(I)S_q(J) = \frac{1-\sum\limits_i (P_i^I)^q - \sum\limits_j (P_j^J)^q + \sum\limits_i (P_i^I)^q \sum\limits_j (P_j^J)^q}{(q-1)^2},$$

then, the next step is rearranging the above relation

$$\begin{aligned}(1-q)S_q(I)S_q(J) &= \frac{-1+\sum\limits_i (P_i^I)^q + \sum\limits_j (P_j^J)^q - \sum\limits_i (P_i^I)^q \sum\limits_j (P_j^J)^q}{q-1},\\ &= -\frac{1-\sum\limits_i (P_i^I)^q}{q-1} - \frac{1-\sum\limits_j (P_j^J)^q}{q-1} + \frac{1-\sum\limits_i (P_i^I)^q \sum\limits_j (P_j^J)^q}{q-1},\\ &= -S_q(I) - S_q(J) + S_q(I+J),\end{aligned} \tag{4.6}$$

where

$$S_q(I+J) = \frac{1 - \sum_i (P_i^I)^q \sum_j (P_j^J)^q}{q-1}.$$

Finally, by rearranging the last expression of Eq. (4.6) we obtain the pseudo additivity result found in Eq. (4.3). Another important property of probability is the following: suppose that the set of W possibilities is arbitrarily separated into two subsets having respectively W_L and W_M possibilities ($W_L + W_M = W$). The corresponding probabilities can be written as $P_1, P_2, ..., P_{W_L}$ and $P_{W_L+1}, ..., P_W$. Thus, it is straightforward to verify the additivity rule (Shannon additivity) by defining

$$P_L = \sum_{i=1}^{W_L} P_i, \tag{4.7}$$

and

$$P_M = \sum_{i=1+W_L}^{W} P_i, \tag{4.8}$$

so that Shannon additivity becomes

$$S_q(\{P_i\}) = S_q(P_L, P_M) + P_L^q S_q(\{P_i/P_L\}) + P_M^q S_q(\{P_i/P_M\}), \tag{4.9}$$

where the sets P_i/P_L and P_i/P_M are the conditional probabilities. Now, we want to prove Eq. (4.9). We start from Tsallis form of entropy

$$S_q(\{P_i\}) = \frac{1 - \sum_{i=1}^{W_L} P_i^q - \sum_{i=W_L+1}^{W} P_i^q}{q-1}, \tag{4.10}$$

we can express S_q in terms of conditional probabilities P_i/P_L which is

$$S_q(\{P_i/P_L\}) = \frac{1 - \sum_{i=1}^{W_L} \left(\frac{P_i}{P_L}\right)^q}{q-1}, \tag{4.11}$$

then by rearranging Eq. (4.11), we obtain

$$\sum_{i=1}^{W_L} P_i^q = P_L^q - (q-1) P_L^q S_q(\{P_i/P_L\}). \tag{4.12}$$

Similarly, S_q can be written in the following form

$$S_q(\{P_i/P_M\}) = \frac{1 - \sum\limits_{i=1+W_L}^{W} \left(\frac{P_i}{P_M}\right)^q}{q-1}. \tag{4.13}$$

Then by rearranging Eq. (4.13), we get

$$\sum_{i=1+W_L}^{W} P_i^q = P_L^q - (q-1)P_L^q S_q(\{P_i/P_M\}), \tag{4.14}$$

and substituting Eq. (4.12) and (4.14) into (4.10) to get

$$S_q(\{P_i\}) = \frac{1 - P_L^q - P_M^q}{q-1} + P_L^q S_q(\{P_i/P_L\}) + P_M^q S_q(\{P_i/P_M\}), \tag{4.15}$$

where

$$\frac{1 - P_L^q - P_M^q}{q-1} = S_q(\{P_L, P_M\}).$$

Hence Eq. (4.15) is the same as Eq. (4.9). Equation (4.9) is a property of Tsallis statistics. Since the probabilities P_i are numbers between zero and unity, we will have

$$P_i^q > P_i \quad \text{for } q < 1, \tag{4.16}$$

and

$$P_i^q < P_i \quad \text{for } q > 1. \tag{4.17}$$

Therefore, $q < 1$ and $q > 1$ will respectively give information about the rare and the frequent events. The other condition is for $S_q \geqslant 0$ for any arbitrary set P_i and for any value of q (positivity). This simple property lies at the heart of non-extensive statistics proposed by Tsallis [44]. Another interesting property is the following: the BG entropy, S, satisfies the following relation

$$-\left[\frac{d}{dq}\sum_{i=1}^{W} P_i^q\right]_{q=1} = -\sum_{i=1}^{W} P_i \ln P_i \equiv S. \tag{4.18}$$

F. Jackson [111] introduced in 1909 the following generalized differential operator which can be applied to an arbitrary function $f(x)$ as

$$D_q f(x) \equiv \frac{f(qx) - f(x)}{qx - x}, \tag{4.19}$$

which recovers the usual derivative in the limit q tends to 1. Sumiyoshi Abe [112] also showed that

$$-D_q \sum_{i=1}^{W} P_i^q = \frac{1 - \sum_{i=1}^{W} P_i^q}{q - 1} \equiv S_q. \tag{4.20}$$

Thus, as we can see from the Fig. 4.1 S_q has with regard to P_i, a definite concavity for all values of q: S_q is concave for $q > 0$ and convex for $q < 0$. Further mathematical relations about q-exponential and q-logarithm functions can be found in the appendix C.2.

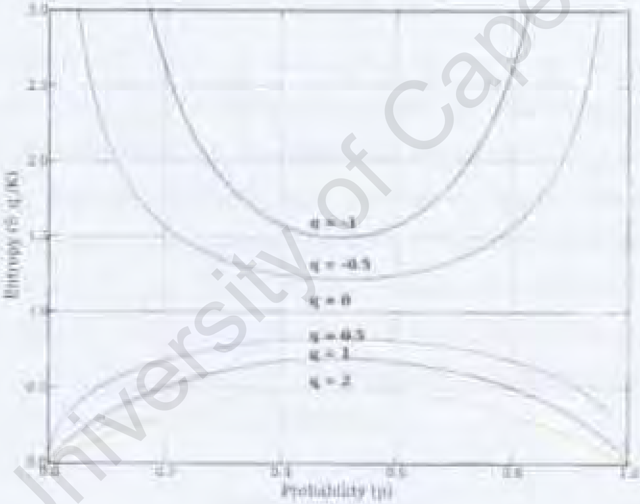

Figure 4.1: $S_q(\{P_i\})$ for $W = 2$ and typical values of q (numbers on curves).

4.2 Tsallis Distribution for Particle Multiplicities.

The standard Fermi-Dirac distribution is given by

$$n^{FD}(E) \equiv \frac{1}{1+\exp\left(\frac{E-\mu}{T}\right)}. \tag{4.21}$$

The Tsallis form has been proposed in the literature, some of these have been shown not to be thermodynamically consistent. In the following we use the Tsallis form of Fermi-Dirac distribution proposed in [113, 114, 115, 116, 117] which uses

$$n_T^{FD}(E) \equiv \frac{1}{1+\exp_q\left(\frac{E-\mu}{T}\right)}. \tag{4.22}$$

where the function $\exp_q(x)$, for $q > 1$ is defined as

$$\exp_q(x) \equiv \begin{cases} [1+(q-1)x]^{1/(q-1)} & \text{if} \quad x > 0 \\ [1+(1-q)x]^{1/(1-q)} & \text{if} \quad x \leq 0. \end{cases} \tag{4.23}$$

Eq. (4.23) was given in [113]. It was stated in the form of the generalized exponential function $\exp_q(x)$ in order to express the cut-off prescription, and the corresponding generalization of the canonical distribution in a compact form. For our present case, we only need the basic features of $\exp_q(x)$ already mentioned. A similar situation arose in the case of Tsallis' generalized exponential $\exp_q(x)$: this function was introduced as a compact and elegant notation for Tsallis' maximum entropy distributions. The extensive form of mathematical properties of $\exp_q(x)$ only occurred in the limit where $q \to 1$ reduces to the standard exponential (the detailed derivation is given in appendix C.1):

$$\lim_{q\to 1} \exp_q(x) \to \exp(x).$$

The form given in Eqs. (4.22) and (4.23) will be referred to as the Tsallis-FD distribution. The Bose-Einstein version (given below) will be referred to as the Tsallis-BE distribution [118]. It should be noted that variations of the above have been presented previously in the literature. These will not be considered in this thesis.

All forms of the Tsallis distribution introduce a new parameter q. In practice this parameter is always close to 1, e.g. in the results obtained by the ALICE and CMS collaborations typical values for the parameter q can be obtained from fits to the transverse momentum distribution for identified charged particles [11] and are in the range 1.1 to 1.2. The value of q should thus be considered as never being far from 1, deviating from it by 20% at most. An analysis of the composition of final state particles leads to a similar result [119] for the parameter q.

In the limit where $q \to 1$ the Tsallis form and standard statistical form coincide. Numerically the difference is small, as shown in Fig. (4.2, 4.3 (A) and (B)) for a value of $q = 1.1$.

The Boltzmann form leads to the result [120, 121]

$$n_T^B(E) = \left[1 + (q-1)\frac{E-\mu}{T}\right]^{-\frac{1}{q-1}}, \tag{4.24}$$

this is called Tsallis-B form. Note that we do not use the normalized q-probabilities which have been proposed in Ref. [121] since we use here mean occupation numbers which do not need to be normalized. In the limit where $q \to 1$ all distributions coincide with the standard statistical distributions:

$$\begin{aligned}
\lim_{q\to 1} n_T^B(E) &= n^B(E), && (4.25)\\
\lim_{q\to 1} n_T^{FD}(E) &= n^{FD}(E), && (4.26)\\
\lim_{q\to 1} n_T^{BE}(E) &= n^{BE}(E). && (4.27)
\end{aligned}$$

A derivation of the Tsallis distribution, based on the Boltzmann equation, has been given in Ref. [122]. A comparison between the n_T^{FD} and n^{FD} distributions is shown in Fig. 4.3 (A). For the Boltzmann form, the Tsallis distribution is always larger than the Boltzmann one if $q > 1$, as shown in Fig. (4.2).

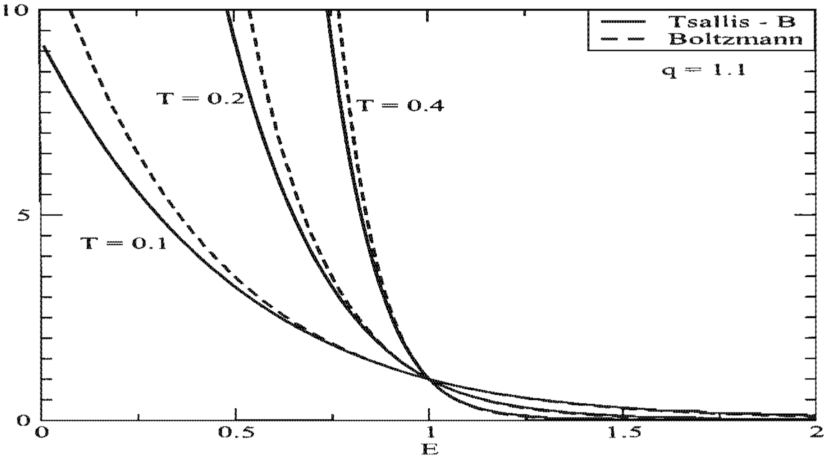

Figure 4.2: Comparison between the Boltzmann and Tsallis-B distribution as a function of the energy E, keeping the Tsallis parameter q fixed, for various values of the temperature T. The chemical potential is kept equal to one in all curves, the units are arbitrary.

Similary, one can compare the Bose-Einstein and Tsallis-BE distributions in Fig. 4.3 (B). Taking into account the large p_T results for particle production we will only consider this possibility in this chapter. As a consequence, in order to keep the particle yields the same, the Tsallis distribution always leads to smaller values of the freeze-out temperature for the same set of particle yields [119]. The Tsallis distribution for quantum statistics has been considered in Ref. [114, 115, 118, 123, 124].

4.3 Thermodynamic Consistency

The first and second laws of thermodynamics lead to the following two differential relations [125]

$$d\epsilon = Tds + \mu dn, \tag{4.28}$$

$$dP = sdT + nd\mu. \tag{4.29}$$

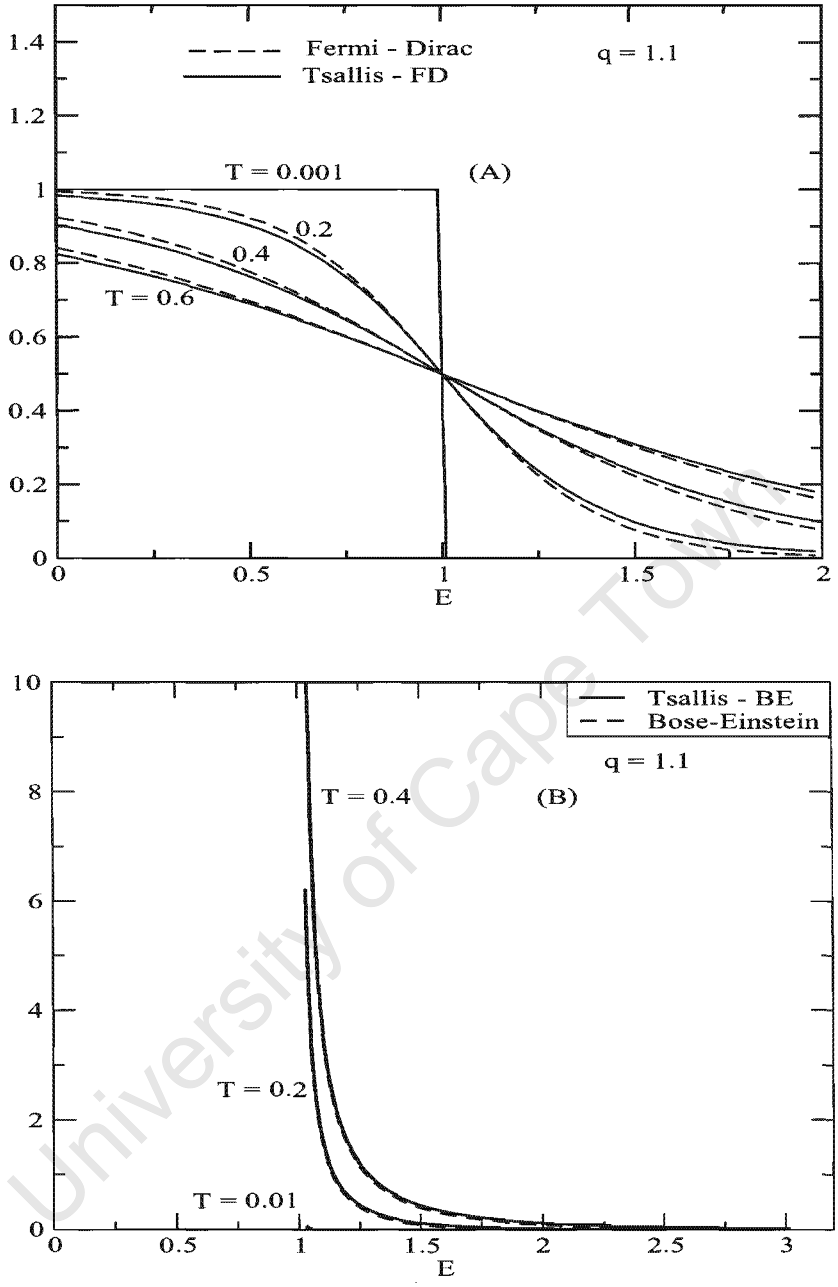

Figure 4.3: Comparison between the Fermi-Dirac and Tsallis-FD distributions (A), Bose-Einstein and Tsallis-BE distributions (B) as a function of the energy E, keeping the Tsallis parameter q fixed, for various values of the temperature T. The chemical potential is kept equal to one in all curves, the units are arbitrary.

where $\epsilon = E/V$, $s = S/V$ and $n = N/V$. Since these are total differentials, thermodynamic consistency requires that the following relations be satisfied

$$T = \left.\frac{\partial \epsilon}{\partial s}\right|_n , \tag{4.30}$$

$$\mu = \left.\frac{\partial \epsilon}{\partial n}\right|_s , \tag{4.31}$$

$$n = \left.\frac{\partial P}{\partial \mu}\right|_T , \tag{4.32}$$

$$s = \left.\frac{\partial P}{\partial T}\right|_\mu . \tag{4.33}$$

The pressure, energy density and entropy density are all given by corresponding integrals over Tsallis distributions and the derivatives have to reproduce the corresponding physical quantities. For completeness, in the next section, we derive Tsallis thermodynamics using the maximal entropy principle and discuss quantum q-statistics in particular Bose-Einstein and Fermi-Dirac distribution by maximizing the entropy of the system for quantum distributions. This follows partly the derivation of Ref. [113]. We will show that the consistency conditions given above are indeed obeyed by the Tsallis-FD and Tsallis-B distributions.

4.3.1 Quantum Statistics Form

The entropy in standard statistical mechanics for fermions is given in the large volume limit by:

$$S^{FD} = -gV \int \frac{d^3p}{(2\pi)^3} \left[n^{FD} \ln n^{FD} + (1 - n^{FD}) \ln(1 - n^{FD}) \right], \tag{4.34}$$

where g is the degeneracy factor and V the volume of the system. The volume of the system can be considered in terms of fireball radius, R

$$V = \frac{4\pi}{3} R^3. \tag{4.35}$$

For simplicity Eq. (4.34) refers to one particle species but can be easily generalized to many by summing over all of them. In the limit where momenta are quantized, it is given by:

$$S^{FD} = -g\sum_i \left[n_i \ln n_i + (1-n_i)\ln(1-n_i)\right], \tag{4.36}$$

For convenience we will work with the discrete form in the rest of this section. The large volume limit can be recovered with the standard replacement:

$$\sum_i \to V\int \frac{d^3p}{(2\pi)^3} \tag{4.37}$$

The generalization, using the Tsallis prescription, leads to [114, 115, 116]

$$S_T^{FD} = -g\sum_i \left[n_i^q \ln_q n_i + (1-n_i)^q \ln_q(1-n_i)\right], \tag{4.38}$$

where use has been made of the function

$$\ln_q(x) \equiv \frac{x^{1-q}-1}{1-q}, \tag{4.39}$$

often referred to as q-logarithm. It can be easily shown that in the limit where the Tsallis parameter q tends to 1 one has:

$$\lim_{q\to 1} \ln_q(x) = \ln(x). \tag{4.40}$$

The maximization of the entropy Eq. (4.38) will give the n_i's their Tsallis-type form. If we use the explicit form of the q-logarithms we obtain

$$S_T^{FD} = g\sum_i \left[\left(\frac{n_i - n_i^q}{q-1}\right) + \left(\frac{(1-n_i)-(1-n_i)^q}{q-1}\right)\right], \tag{4.41}$$

In a similar vein, the generalized form of the entropy for bosons is given by

$$S_T^{BE} = -g\sum_i \left[n_i^q \ln_q n_i - (1+n_i)^q \ln_q(1+n_i)\right], \tag{4.42}$$

by using a similar method, we can express Eq. (4.42) as

$$S_T^{BE} = g\sum_i \left[\left(\frac{n_i - n_i^q}{q-1}\right) - \left(\frac{(1+n_i)-(1+n_i)^q}{q-1}\right)\right], \tag{4.43}$$

In the limit $q \to 1$ Eqs. (4.38) and (4.42) reduce to the standard Fermi-Dirac and Bose-Einstein distributions. Further, as we shall presently explain, the formulation of a variational principle in terms of Eq. (4.41) allows to prove the general relation of thermodynamics. One of the relevant constraints is given by the average number of particles,

$$\sum_i n_i^q = N. \tag{4.44}$$

Notice the unusual power of q on the left-hand side. As it turns out, it is necessary to have this power of q since otherwise there is no thermodynamic consistency.

Likewise, the energy of the system gives a constraint,

$$\sum_i n_i^q E_i = E. \tag{4.45}$$

again, it is necessary to have the power q on the left-hand side as no thermodynamic consistency would be achieved without it. The maximization of the entropic measure Eq. (4.41) under the constraints Eq. (4.44) and (4.45) leads to the variational problem.

$$\frac{\delta}{\delta n_i}\left[S_T^{FD} + \alpha(N - \sum_i n_i^q) + \beta(E - \sum_i n_i^q E_i)\right] = 0, \tag{4.46}$$

where α and β are Lagrange multipliers associated, respectively, with the total number of particles and the total energy. Differentiating each expression in Eq. (4.46)

$$\frac{\delta}{\delta n_i}\left(S_T^{FD}\right) = \frac{q}{q-1}\left[\left(\frac{1-n_i}{n_i}\right)^{q-1} - 1\right] n_i^{q-1}, \tag{4.47}$$

$$\frac{\delta}{\delta n_i}\left(N - \sum_i n_i^q\right) = -q n_i^{q-1}, \tag{4.48}$$

and

$$\frac{\delta}{\delta n_i}\left(E - \sum_i n_i^q E_i\right) = -q E_i n_i^{q-1}, \tag{4.49}$$

then by substituting Eq. (4.47), (4.48) and (4.49) into (4.46), we obtain

$$qn_i^{q-1}\left\{\frac{1}{q-1}\left[-1+\left(\frac{1-n_i}{n_i}\right)^{q-1}\right]-\beta E_i-\alpha\right\}=0, \tag{4.50}$$

which can be rewritten as

$$\frac{1}{q-1}\left[-1+\left(\frac{1-n_i}{n_i}\right)^{q-1}\right]=\beta E_i+\alpha, \tag{4.51}$$

and, by rearranging Eq. (4.51), we get

$$\frac{1-n_i}{n_i}=\left[1+(q-1)(\beta E_i+\alpha)\right]^{\frac{1}{q-1}},$$

finally, we get the solution of generalized form of Fermi-Dirac distribution

$$\begin{aligned} n_i &= \frac{1}{\left[1+(q-1)(\beta E_i+\alpha)\right]^{\frac{1}{q-1}}+1}, \\ &= \frac{1}{\left[\exp_q(\alpha+\beta E_i)\right]+1}, \end{aligned} \tag{4.52}$$

which is the expression for the Tsallis-FD distribution referred to earlier in these papers [114, 115, 116].

Using a similar approach one can also determine the Tsallis-BE distribution [118]. Starting from the extremum of the entropy subject to two conditions:

$$\frac{\delta}{\delta n_i}\left[S_T^{BE}+\alpha(N-\sum_i n_i^q)+\beta(E-\sum_i n_i^q E_i)\right]=0, \tag{4.53}$$

which leads to

$$\frac{\delta}{\delta n_i}\left(S_T^{BE}\right)=\frac{q}{q-1}\left[\left(\frac{1+n_i}{n_i}\right)^{q-1}-1\right]n_i^{q-1}, \tag{4.54}$$

and by using Eqs. (4.54),(4.48) and (4.49) in (4.53),

$$\sum_i qn_i^{q-1}\left\{\frac{1}{q-1}\left[-1+\left(\frac{1+n_i}{n_i}\right)^{q-1}\right]-\beta E_i-\alpha\right\}=0. \tag{4.55}$$

By rearranging Eq. (4.55), one obtains the expression for the Tsallis-BE distribution [118],

$$
\begin{aligned}
n_i &= \frac{1}{\left[1+(q-1)(\beta E_i+\alpha)\right]^{\frac{1}{q-1}}-1}, \\
&= \frac{1}{\left[\exp_q((E_i-\mu)/T)\right]-1},
\end{aligned} \tag{4.56}
$$

where the usual identifications $\alpha = -\mu/T$ and $\beta = 1/T$ have been made. In the next section we review the derivation of the Tsallis distribution by emphasizing the quantum and Boltzmann statistical forms and show their thermodynamic consistency.

Proof of Thermodynamical Consistency

In order to use the above expressions it has to be shown that they satisfy the thermodynamic consistency conditions. To show this in detail we use the first law of thermodynamics [125]

$$
P = \frac{-E+TS+\mu N}{V}, \tag{4.57}
$$

and take the partial derivative with respect to μ in order to check for thermodynamic consistency, it leads to

$$
\begin{aligned}
\left.\frac{\partial P}{\partial \mu}\right|_T &= \frac{1}{V}\left[-\frac{\partial E}{\partial \mu}+T\frac{\partial S}{\partial \mu}+N+\mu\frac{\partial N}{\partial \mu}\right], \\
&= \frac{1}{V}\left[N+\sum_i\left(\mu-E_i-\frac{T}{q-1}\right)\frac{\partial n_i^q}{\partial \mu}+\frac{Tq(1-n_i)^{q-1}}{q-1}\frac{\partial n_i}{\partial \mu}\right], \\
&= \frac{1}{V}\left[N+\sum_i-\frac{T}{q-1}\left(1+\frac{(q-1)(E_i-\mu)}{T}\right)\frac{\partial n_i^q}{\partial \mu}+\frac{Tq(1-n_i)^{q-1}}{q-1}\frac{\partial n_i}{\partial \mu}\right], \\
&= \frac{1}{V}\left[N+\sum_i-\frac{T}{q-1}\left(1+(q-1)\frac{E_i-\mu}{T}\right)\frac{\partial n_i^q}{\partial \mu}\right. \\
&\quad \left.+\frac{Tq(1-n_i)^{q-1}}{q-1}\frac{\partial n_i}{\partial \mu}\right],
\end{aligned} \tag{4.58}
$$

then, by explicit calculation

$$
\frac{\partial n_i^q}{\partial \mu} = \frac{q n_i^{q+1}}{T}\left[1+(q-1)\frac{E_i-\mu}{T}\right]^{-1+\frac{1}{1-q}},
$$

$$\frac{\partial n_i}{\partial \mu} = \frac{n_i^2}{T}\left[1 + (q-1)\frac{E_i - \mu}{T}\right]^{-1+\frac{1}{1-q}},$$

and

$$(1 - n_i)^{q-1} = n_i^{q-1}\left[1 + \frac{(q-1)(E_i - \mu)}{T}\right].$$

Introducing this into Eq. (4.58), yields

$$\left.\frac{\partial P}{\partial \mu}\right|_T = n, \tag{4.59}$$

which proves the thermodynamical consistency Eq. (4.32).

We also calculate explicitly the relation in Eq. (4.30) can be rewritten as

$$\begin{aligned} \left.\frac{\partial E}{\partial S}\right|_n &= \frac{\frac{\partial E}{\partial T}dT + \frac{\partial E}{\partial \mu}d\mu}{\frac{\partial S}{\partial T}dT + \frac{\partial S}{\partial \mu}d\mu}, \\ &= \frac{\frac{\partial E}{\partial T} + \frac{\partial E}{\partial \mu}\frac{d\mu}{dT}}{\frac{\partial S}{\partial T} + \frac{\partial S}{\partial \mu}\frac{d\mu}{dT}}, \end{aligned} \tag{4.60}$$

since n is kept fixed one has the additional constraint

$$dn = \frac{\partial n}{\partial T}dT + \frac{\partial n}{\partial \mu}d\mu = 0,$$

leading to

$$\frac{d\mu}{dT} = -\frac{\frac{\partial n}{\partial T}}{\frac{\partial n}{\partial \mu}}. \tag{4.61}$$

Now, we rewrite Eq. (4.60) and (4.61) in terms of the following expressions

$$\frac{\partial E}{\partial T} = \sum_i qE_i n_i^{q-1}\frac{\partial n_i}{\partial T},$$

$$\frac{\partial E}{\partial \mu} = \sum_i qE_i n_i^{q-1}\frac{\partial n_i}{\partial \mu},$$

$$\frac{\partial S}{\partial T} = \sum_i q\left[\frac{-n_i^{q-1} + (1-n_i)^{q-1}}{q-1}\right]\frac{\partial n_i}{\partial T},$$

$$\frac{\partial S}{\partial \mu} = \sum_i q\left[\frac{-n_i^{q-1} + (1-n_i)^{q-1}}{q-1}\right]\frac{\partial n_i}{\partial \mu},$$

$$\frac{\partial n}{\partial T} = \frac{1}{V}\left[\sum_i q n_i^{q-1}\frac{\partial n_i}{\partial T}\right],$$

and

$$\frac{\partial n}{\partial \mu} = \frac{1}{V}\left[\sum_i q n_i^{q-1}\frac{\partial n_i}{\partial \mu}\right].$$

By introducing the above relations into Eq. (4.60), the numerator of Eq. (4.60) becomes

$$\begin{aligned}\frac{\partial E}{\partial T} &+ \frac{\partial E}{\partial \mu}\frac{d\mu}{dT} = \sum_i q E_i n_i^{q-1}\frac{\partial n_i}{\partial T} \\ & -\frac{\sum_{i,j} q^2 E_j\,(n_i n_j)^{q-1}\,\frac{\partial n_j}{\partial \mu}\frac{\partial n_i}{\partial T}}{\sum_j q n_j^{q-1}\frac{\partial n_j}{\partial \mu}}, \\ &= \frac{\sum_{i,j} q E_i\,(n_i n_j)^{q-1}\,C_{ij}}{\sum_j n_j^{q-1}\frac{\partial n_j}{\partial \mu}}. \end{aligned} \tag{4.62}$$

Where the abbreviation

$$C_{ij} \equiv (n_i n_j)^{q-1}\left[\frac{\partial n_i}{\partial T}\frac{\partial n_j}{\partial \mu} - \frac{\partial n_j}{\partial T}\frac{\partial n_i}{\partial \mu}\right], \tag{4.63}$$

has been introduced. One can rewrite the denominator part of Eq. (4.60) as

$$\begin{aligned}\frac{\partial S}{\partial T} + \frac{\partial S}{\partial \mu}\frac{d\mu}{dT} &= \frac{q\sum_{i,j}\left[-n_i^{q-1} + (1-n_i)^{q-1}\right] n_j^{q-1} C_{i,j}}{(q-1)\sum_j n_j^{q-1}\frac{\partial n_j}{\partial \mu}}, \\ &= \frac{q\sum_{i,j}(E_i-\mu)\,(n_i n_j)^{q-1}\,C_{i,j}}{T\sum_j n_j^{q-1}\frac{\partial n_j}{\partial \mu}}, \end{aligned} \tag{4.64}$$

where

$$\frac{-n_i^{q-1} + (1-n_i)^{q-1}}{q-1} = \frac{(E_i-\mu)}{T} n_i^{q-1},$$

hence, by substituting Eq. (4.62) and (4.64) in to (4.60), we find

$$\left.\frac{\partial E}{\partial S}\right|_n = T\frac{\sum\limits_{i,j} E_i C_{ij}}{\sum\limits_{i,j}(E_i - \mu)C_{ij}}, \tag{4.65}$$

since $\sum\limits_{i,j} C_{ij} = 0$, this finally leads to the desired result

$$\left.\frac{\partial E}{\partial S}\right|_n = T. \tag{4.66}$$

Hence thermodynamic consistency is satisfied.

4.3.2 Boltzmann Statistics Form

Due to its practical relevance and importance we devote a section to the Tsallis-B distribution. In this case the entropy is obtained from Eq. (4.33) by assuming the $n_i \ll 1$, this leads to

$$S_T^B \equiv g\sum_{i=1}^{W}\frac{(n_i - n_i^q)}{q-1} + n_i, \tag{4.67}$$

The n_i are given explicitly as

$$n_i = \left[1 + (q-1)\frac{E_i - \mu}{T}\right]^{\frac{1}{1-q}}, \tag{4.68}$$

where n_i denotes the number of particles in the ith energy level with energy E_i. The maximum of the above entropy is looked for under the constraints imposed by fixing the total number of particles N and the total energy of the system E, as given in Eq. (4.44) and (4.45). As in the previous section, it should satisfy thermodynamic consistency which is given in Eq. (4.30). The derivative of pressure w.r.t. μ becomes

$$
\begin{aligned}
\frac{\partial P}{\partial \mu} &= \frac{1}{V}\left[-\frac{\partial E}{\partial \mu} + T\frac{\partial S_q}{\partial \mu} + N + \mu\frac{\partial N}{\partial \mu}\right], \\
&= \frac{1}{V}\left[N + \sum_i \left(-(E_i-\mu) - \frac{T}{q-1}\right)\frac{\partial \overline{n}_i^q}{\partial \mu} + \frac{T}{q-1}\frac{\partial \overline{n}_i}{\partial \mu} + T\frac{\partial \overline{n}_i}{\partial \mu}\right], \\
&= \frac{1}{V}\left[N + \sum_i -\frac{T}{q-1}\left(1 + \frac{(q-1)(E_i-\mu)}{T}\right)\frac{\partial \overline{n}_i^q}{\partial \mu} + T\left(\frac{1}{q-1}+1\right)\frac{\partial \overline{n}_i}{\partial \mu}\right], \\
&= \frac{1}{V}\left[N + \sum_i -\frac{T\overline{n}_i^{1-q}}{q-1}\frac{\partial \overline{n}_i^q}{\partial \mu} + \frac{Tq}{q-1}\frac{\partial \overline{n}_i}{\partial \mu},\right], \qquad (4.69)
\end{aligned}
$$

now, by using

$$\frac{\partial n_i^q}{\partial \mu} = q n_i^{q-1}\frac{\partial n_i}{\partial \mu},$$

and

$$\frac{\partial n_i}{\partial \mu} = \frac{n_i^q}{T}.$$

By the above relations in Eq. (4.69), we recover Eq. (4.32).

We now calculate the expressions needed in Eqs. (4.60) and (4.61) in terms of

$$\frac{\partial S}{\partial T} = \sum_i \left[1 + \frac{1-qn_i^{q-1}}{q-1}\right]\frac{\partial n_i}{\partial T},$$

$$\frac{\partial S}{\partial \mu} = \sum_i \left[1 + \frac{1-qn_i^{q-1}}{q-1}\right]\frac{\partial n_i}{\partial \mu},$$

while the other partial derivatives are the same as previously. Then, by plugging the above relations into Eq. (4.60), then the numerator part of Eq. (4.60) become

$$\begin{aligned}\frac{\partial E}{\partial T}+\frac{\partial E}{\partial \mu}\frac{d\mu}{dT} &= \sum_i qE_i n_i^{q-1}\frac{\partial n_i}{\partial T} \\ &\quad -\frac{\displaystyle\sum_{i,j} q^2 E_j\left(n_i n_j\right)^{q-1}\frac{\partial n_j}{\partial \mu}\frac{\partial n_i}{\partial T}}{\displaystyle\sum_j q n_j^{q-1}\frac{\partial n_j}{\partial \mu}}, \\ &= \frac{\displaystyle\sum_{i,j} qE_i\left(n_i n_j\right)^{q-1} C_{i,j}}{\displaystyle\sum_j n_j^{q-1}\frac{\partial n_j}{\partial \mu}}. \qquad (4.70)\end{aligned}$$

Similarly, the denominator part of Eq. (4.60) can be written as

$$\begin{aligned}\frac{\partial S}{\partial T} + \frac{\partial S}{\partial \mu}\frac{d\mu}{dT} &= \sum_i\left[1+\frac{1-qn_i^{q-1}}{q-1}\right]\frac{\partial n_i}{\partial T} \\ &\quad -\frac{\displaystyle\sum_{i,j} n_i^{q-1}\left[1+\frac{1-qn_j^{q-1}}{q-1}\right]\frac{\partial n_j}{\partial \mu}\frac{\partial n_i}{\partial T}}{\displaystyle\sum_j n_j^{q-1}\frac{\partial n_j}{\partial \mu}}, \\ &= \frac{\displaystyle\sum_{i,j}\left[1+\frac{1-qn_i^{q-1}}{q-1}\right] n_j^{q-1} C_{i,j}}{\displaystyle\sum_j n_j^{q-1}\frac{\partial n_j}{\partial \mu}}, \\ &= \frac{\displaystyle\sum_{i,j}\frac{q(E_i-\mu)}{T}\left(n_i n_j\right)^{q-1} C_{i,j}}{\displaystyle\sum_j n_j^{q-1}\frac{\partial n_j}{\partial \mu}}, \qquad (4.71)\end{aligned}$$

where

$$1+\frac{1-qn_i^{q-1}}{q-1}=\frac{q(E_i-\mu)}{T}n_i^{q-1},$$

by combining the expressions in Eq. (4.70) and (4.71) into (4.60), we find as before

$$\left.\frac{\partial E}{\partial S}\right|_n = T. \qquad (4.72)$$

It has thus been shown that the definitions of temperature and pressure within the Tsallis formalism for non-extensive thermostatistics lead to expressions which satisfy consistency with the first law of thermodynamics.

4.4 Tsallis Distribution and its Application

The Tsallis distribution has gained prominence recently in high energy physics because of the very high quality fits of the transverse momentum distributions made by the STAR [14] and PHENIX collaborations [15] at the RHIC and by the ALICE [11, 12] and CMS collaborations [16] at the LHC.

The measured spectra cover only a limited range in transverse momentum and therefore an appropriately parameterized function is needed to extrapolate into the unmeasured p_T regions for the yield determination. The p_T coverage of the STAR, PHENIX, ALICE and CMS collaborations [11, 14, 15, 16] detectors for hadron particles is large enough that a function which accounts for both the power-law component of the spectra and the low p_T turnover becomes necessary to describe the data. A form that has been suggested is given by Eq. (4.73) [126], called Tsallis-Lévy distribution

$$\begin{aligned} \frac{1}{2\pi p_T}\frac{d^2N}{dydp_T} = \frac{dN}{dy}\frac{(n-1)(n-2)}{2\pi nC[nC+m_0(n-2)]} \\ \times\left(1+\frac{\sqrt{p_T^2+m_0^2}-m_0}{nC}\right)^{-n} \end{aligned} \tag{4.73}$$

where T, p_0, n, $\frac{dN}{dy}$, C, and m_0 are fitting parameters. For our calculations and analysis, we are not going to use Eq. (4.73).

We investigate in this chapter one version which we consider suited for describing results in high energy particle physics. Our main guiding criterium will be thermodynamic consistency which has not always been implemented correctly (see e.g. [113, 127, 128]). The explicit form which we use for the transverse momentum distribution in relativistic heavy ion collisions is:

$$\frac{d^2N}{dp_T\ dy} = \\ gV\frac{p_T m_T \cosh y}{(2\pi)^2}\left[1+(q-1)\frac{m_T\cosh y-\mu}{T}\right]^{q/(1-q)}, \tag{4.74}$$

where p_T, m_T, y, T, μ, V and $g = (2I+1)(2s+1)$ are: transverse momentum, transverse mass, rapidity, temperature, chemical potential, volume and spin-isospin degeneracy factor respectively. In the limit where the parameter $q \to 1$ it reproduces the standard Boltzmann distribution:

$$\lim_{q\to1}\frac{d^2N}{dp_T\ dy} = \\ gV\frac{p_T m_T \cosh y}{(2\pi)^2}\exp\left(-\frac{m_T\cosh y-\mu}{T}\right). \tag{4.75}$$

We distinguish Eq. (4.74) from the form used by the the STAR, PHENIX, ALICE and CMS collaborations [11, 14, 15, 16]. We will refer to Eq. (4.74) as the Tsallis-B parameterization. Note that in particular the extra power of q on the right hand side which differs from Eq. (4.73). The motivation for preferring Eq. (4.74) in this form is presented in detail in the next sections and hence derivation is given in the subsection 4.4.2. The parametrization given in Eq. (4.74) is close to the one used by STAR, PHENIX, ALICE and CMS. The analytic expression used in Refs. [11, 14, 15, 16] corresponds to identifying

$$n \to \frac{q}{q-1} \tag{4.76}$$

and

$$nC \to \frac{T}{q-1}. \tag{4.77}$$

The differences do not allow for the above identification to be made complete due to an additional factor of the transverse mass on the right-hand side and a shift in the transverse mass. They are close but not the same. In particular, no clear pattern emerges for the values of n and C while an interesting regularity is obtained for q, temperature, T and the fireball radius, R are presented in Figs. 4.4, 4.5, 4.8, 4.9, 4.14 and 4.15.

While the description of integrated particle yields is reasonably successful, more detailed descriptions, especially of the transverse and longitudinal momentum distributions call for additional dynamics. The transverse momentum distribution is often described by a combination of transverse flow and a thermodynamical statistical distribution. With the Tsallis distribution, this superposition is not used and a very good fit is obtained using the additional parameter q which describes the deviation from a Boltzmann distribution. Whether this is ultimately the correct description remains to be seen. This chapter would be able to make a contribution to the understanding of the use of the Tsallis distribution in high energy collisions. It is not meant as giving a final answer to the correct dynamical theory of heavy ion collisions.

4.4.1 The Analytic Form of Transverse Momentum Spectrum

The relevance of the equilibrium statistical mechanics remains on the significance of the experimental transverse momentum spectrum and the most stable charged particles (pions, kaons, protons and etc.) can be expressed within the equilibrium formalism.

Clearly, by assuming a purely thermal source with a Boltzmann distribution, the analytic expression for the transverse momentum spectrum can be shown to be as follows [129]:

$$\frac{dN}{p_T dp_T} = \frac{gV}{(2\pi)^2} m_T K_1(z) \ , \tag{4.78}$$

where $z = m_T/T$ and K_1 is the first order modified Bessel function.

Equation (4.78) has been used to fit the experimental transverse momentum spectra and provides an indication of a thermal energy distribution [130, 131].

The experimental slope parameter measures the particle energy, which contains both thermal (random) and collective flow contributions in heavy ion collisions. The thermal motion determines the thermal freeze-out temperature T, namely the temperature when particles cease to interact with each other.

4.4.2 Transverse Momentum Spectrum Expansion in (q-1)

Let us consider a different point of view and argue that the deviation from the Boltzmann slope at high p_T can be ascribed to the presence of non-extensive statistical effects in the steady state distribution of the hadron gas. Hence, we write the Tsallis-B transverse momentum spectrum in the following way

$$\begin{aligned} \frac{dN}{dy\, p_T dp_T} &= \frac{gVm_T}{(2\pi)^2} \cosh y \left[1 + xz\cosh y\right]^{-\frac{x+1}{x}}, \\ &= \frac{gVm_T}{(2\pi)^2} \cosh y \exp\left[-\left(\frac{1+x}{x}\right)\ln(1 + xz\cosh y)\right]. \end{aligned} \tag{4.79}$$

In order to have an analytical expression for transverse momentum spectrum, we consider here only small deviations ($x = q - 1 \approx 0$) for Eq.(4.79). Using Taylor series, we expand the Tsallis-B distribution function at $x \approx 0$ for first order approximation

$$\frac{dN}{dy\, p_T dp_T} = \frac{gVm_T}{(2\pi)^2} \cosh y \exp\left[-(1+x)\left(z\cosh y - \frac{x(z\cosh y)^2}{2}\right)\right], \tag{4.80}$$

where the approximation part is given by

$$\ln(1 + xz\cosh y) \approx xz\cosh y - \frac{(xz\cosh y)^2}{2}, \tag{4.81}$$

since the approximation is first order, thus in Eq.(4.80), we ignore the quadratic term, this shows that

$$\frac{dN}{dy\, p_T dp_T} = \frac{gVm_T}{(2\pi)^2} \cosh y \exp\left[-xz\cosh y + \frac{x(z\cosh y)^2}{2}\right] f(y,z), \tag{4.82}$$

where $f(y,z) = \exp(-z\cosh y)$ and again expand Eq.(4.82) for the exponential part at $x \approx 0$, it yields

$$\frac{dN}{dy\, p_T dp_T} = \frac{gVm_T}{(2\pi)^2} \cosh y \left[1 - xz\cosh y + \frac{x(z\cosh y)^2}{2}\right] f(y,z), \tag{4.83}$$

then, integrating w.r.t. y

$$\begin{aligned}\frac{dN}{p_T dp_T} &= \frac{gVm_T}{(2\pi)^2}\int_{-\infty}^{\infty} dy \cosh y \left[1 - xz\cosh y + \frac{x(z\cosh y)^2}{2}\right] f(y,z) \\ &= \frac{gVm_T}{(2\pi)^2}(T_1+T_2+T_3), \end{aligned} \tag{4.84}$$

where

$$\begin{aligned} T_1 &= \int_{-\infty}^{\infty} dy f(y,z)\cosh y, \\ &= 2K_1(z), \end{aligned} \tag{4.85}$$

$$\begin{aligned} T_2 &= -xz\int_{-\infty}^{\infty} dy f(y,z)\cosh^2 y, \\ &= -xzK_2(z), \end{aligned} \tag{4.86}$$

and

$$\begin{aligned} T_3 &= \frac{xz^2}{2}\int_{-\infty}^{\infty} dy f(y,z)\cosh^3 y, \\ &= \frac{xz^2(K_3(z)+3K_1(z))}{4}. \end{aligned} \tag{4.87}$$

Finally, by substituting Eqs.(4.85), (4.86) and (4.87) into (4.84), for a first order in $x = q-1$ the transverse momentum spectrum can be written as

$$\frac{dN}{p_T dp_T} = \frac{gVm_T}{2\pi^2}\left\{K_1(z) - \frac{(q-1)}{2} zK_2(z) + \frac{(q-1)}{8} z^2 \; [3\,K_1(z) + K_3(z)]\right\}, \tag{4.88}$$

where K_2 and K_3 are the modified Bessel functions of the second and third order. The result given in Eq.(4.88) is the analytic form of the first order in (q-1) transverse momentum spectrum. A similar derivation and analysis are found in [131, 132].

4.4.3 Tsallis Fit Details

The total number of particles is given by the integral version of Eq (4.44),

$$N = gV \int \frac{d^3p}{(2\pi)^3}\left[1+(q-1)\frac{E-\mu}{T}\right]^{q/(1-q)} . \tag{4.89}$$

The extra power q is necessary for thermodynamic consistency. The corresponding (invariant) momentum distribution is given by

$$E\frac{dN}{d^3p} = gVE\frac{1}{(2\pi)^3}\left[1+(q-1)\frac{E-\mu}{T}\right]^{q/(1-q)} , \tag{4.90}$$

which, in terms of the rapidity and transverse mass variables, becomes

$$\begin{aligned} \frac{dN}{dy\, p_T dp_T} &= gV\frac{m_T\cosh y}{(2\pi)^2} \\ &\times\left[1+(q-1)\frac{m_T\cosh y-\mu}{T}\right]^{q/(1-q)} . \end{aligned} \tag{4.91}$$

At mid-rapidity, $y = 0$ and for zero chemical potential reduces to the following expression

$$\left.\frac{dN}{p_T dp_T\; dy}\right|_{y=0} = gV\frac{m_T}{(2\pi)^2}\left[1+(q-1)\frac{m_T}{T}\right]^{q/(1-q)} , \tag{4.92}$$

or, with the transverse momentum:

$$\left.\frac{dN}{dp_T\; dy}\right|_{y=0} = gV\frac{p_T m_T}{(2\pi)^2}\left[1+(q-1)\frac{m_T}{T}\right]^{q/(1-q)} . \tag{4.93}$$

At mid-rapidity, the expressions for the integrated particle yield, dN/dy and average transverse momentum, $< p_T >$ using Tsallis-B distribution are defined by

$$\left.\frac{dN}{dy}\right|_{y=0} = a\int_0^\infty dp_T m_T p_T\left[1+(q-1)\frac{m_T}{T}\right]^{q/(1-q)} , \tag{4.94}$$

and

$$< p_T >= \frac{a\int_0^\infty dp_T m_T p_T^2\left[1+(q-1)\frac{m_T}{T}\right]^{q/(1-q)}}{\frac{dN}{dy}} , \tag{4.95}$$

respectively, where a is the normalization constant.

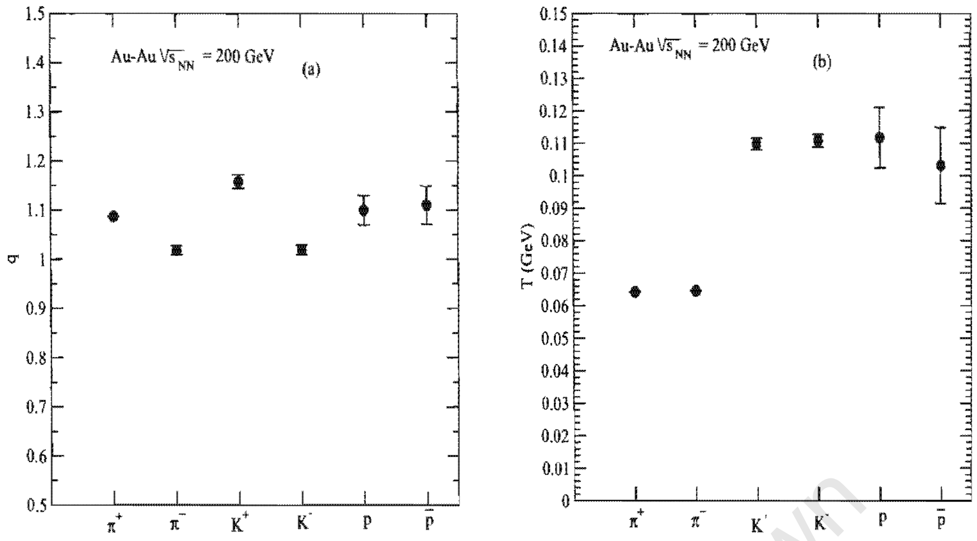

Figure 4.4: The calculated value of q, and temperature T in Au-Au collision at 200 GeV, for different hadron species.

Using the result of Au-Au collision at 200 GeV [23], we have analyzed with Tsallis-B distribution in order to obtain the q parameters and temperature, T for identified hadron species. These are shown in Table 4.1 as well as in Figs. 4.4 and 4.5.

Table 4.1: The calculated values of T and q for different hadron species measured by the STAR [23] in Au-Au collision at 200 GeV using the Tsallis-B form for the momentum distribution.

Particle	q	T (GeV)
π^+	1.0871 ± 0.0008	0.0642 ± 0.0001
π^-	1.0186 ± 0.0091	0.0647 ± 0.0001
K^+	1.1579 ± 0.0143	0.1099 ± 0.0018
K^-	1.0194 ± 0.0095	0.1109 ± 0.0019
p	1.0999 ± 0.0298	0.1118 ± 0.0093
$\bar{p}$	1.1100 ± 0.0388	0.1032 ± 0.0117

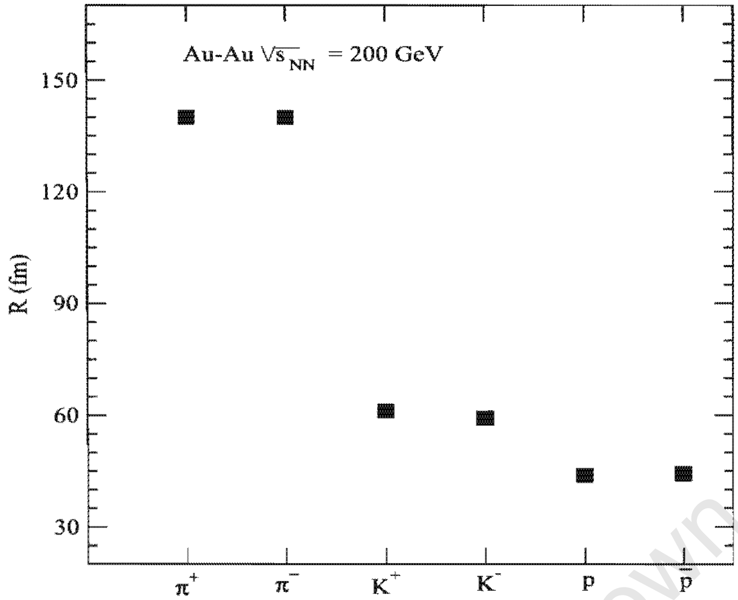

Figure 4.5: The calculated values of the radius, R in Au-Au collision at 200 GeV for different hadron species.

In Fig 4.4(a) the q values are consistent in the range of 1.05 - 1.2; this is also shown in Table 4.1. However, in Fig. 4.4(b) there are variations in temperature values between pions and other hadron species, in particular there is a high jump for the temperature, it rises from lower to higher values between pions and kaons. For the other hadrons, the temperature values are closer to each other compare to pions.

Fig. 4.6 presents the integrated particle yield, dN/dy and average transverse momenta, $\langle p_T \rangle$ for central collision with different hadron species. According to the results in Fig. 4.6 (a) the integrated particle yield decreases as the mass of hadrons increases. However, Fig. 4.6 (b) shows the average transverse momenta of the hadrons increase as the mass of hadrons increase. In addition, we have also compared Fig. 4.6 (a) and (b) Tsallis-B distribution results with STAR results [23]. Hence, most of the results are close to the STAR data; especially, the pions are much closer to the STAR data.

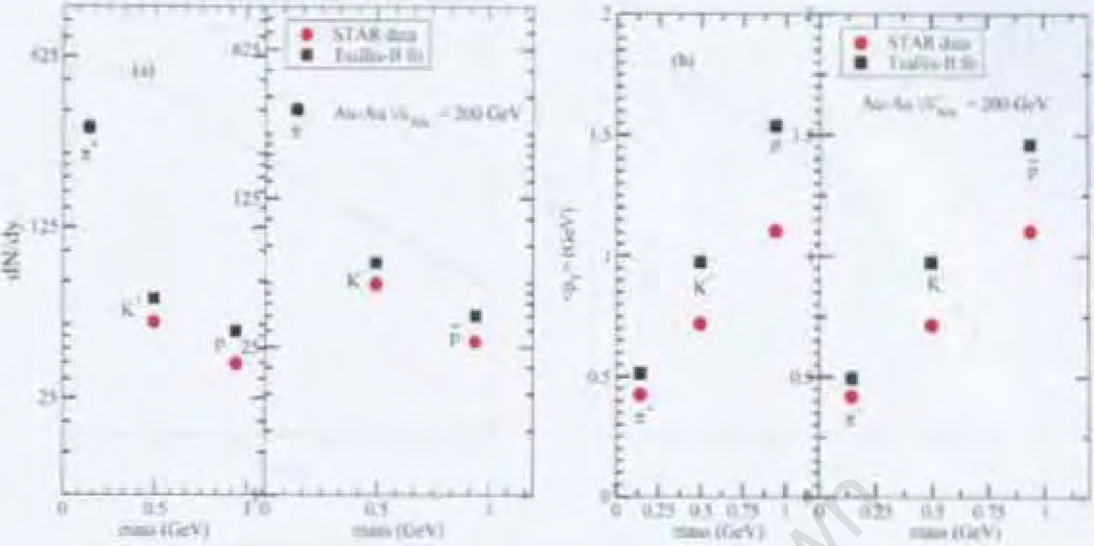

Figure 4.6: The particle yield at mid-rapidity dN/dy and the average transverse momentum, $\langle p_T \rangle$ for different hadron species. The results have been compared with STAR result [23].

The experimental measurements published by the STAR collaboration [23] for Au-Au collision at 200 GeV results and a fit are shown in Fig. 4.7. According to Fig. 4.7, the Tsallis-B distribution fitted the experimental data very well. In addition, the parameters obtained from the Tsallis-B distribution results are shown in Table 4.1 as well as Figs. 4.4 and 4.5.

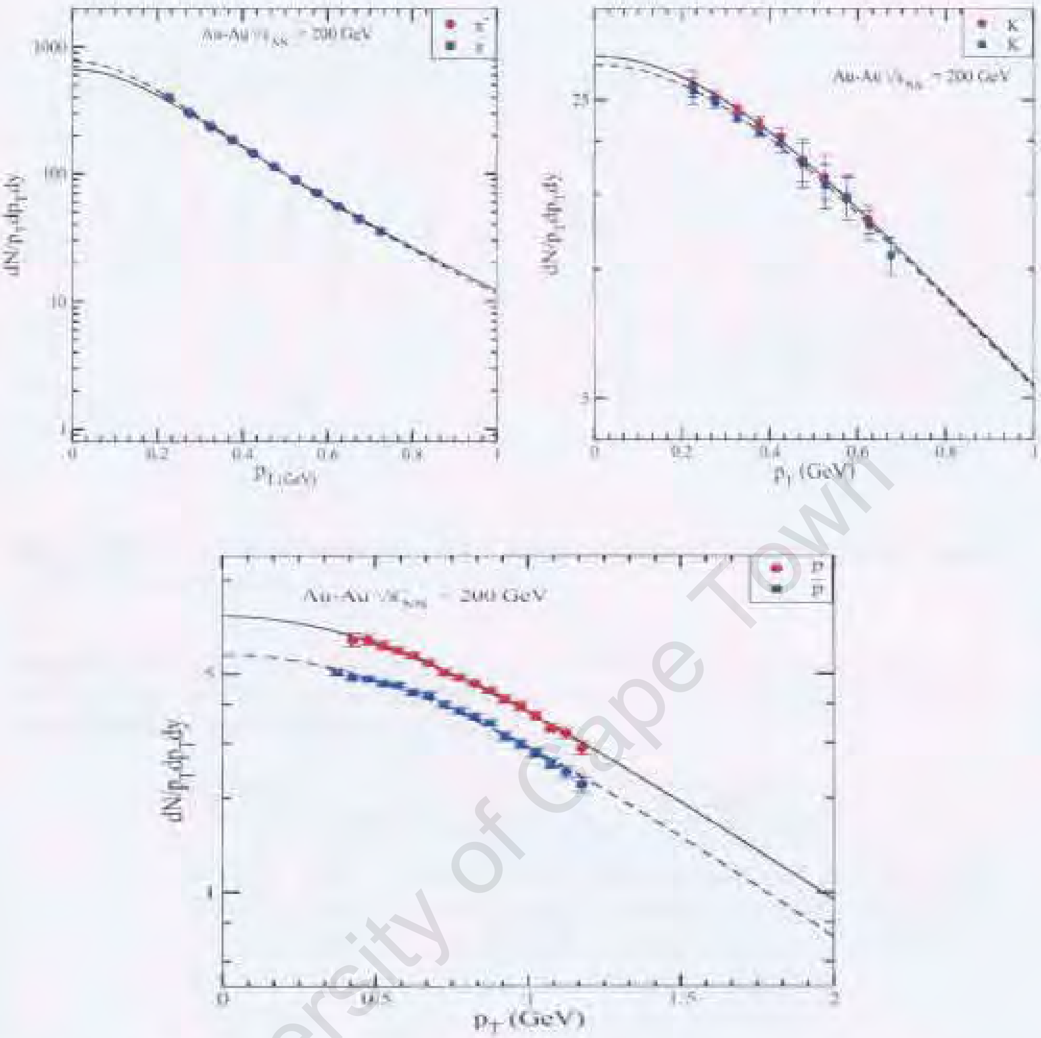

Figure 4.7: Comparison between the measured transverse momentum distribution for π^+ and π^-, K^+ and K^- as well as p and $\bar{p}$ measured by the STAR collaboration [23] in Au-Au collision at 200 GeV and the Tsallis-B distribution. The full and broken lines are fits using the parameterization Eq. (4.93) to the data with the parameters listed in table 4.1.

Similarly, the p-p collisions at 900 GeV and 7 TeV measured by the ALICE collaboration [11] presented in Figs. 4.8 and 4.9 show the relationship between the parameters obtained from the fit, which are the parameter, q, temperature, T and the radius, R for various hadron species. Those parameters were extracted from the fitted Tsallis-B momentum distribution.

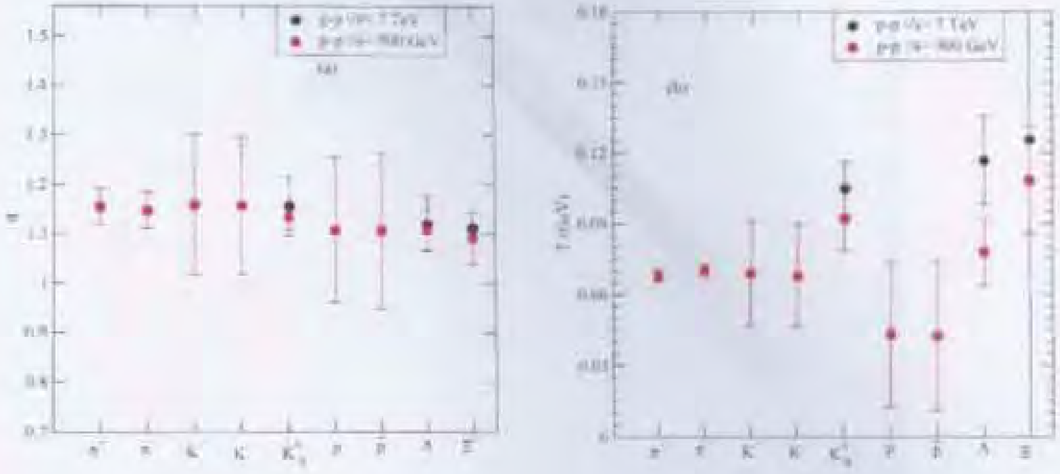

Figure 4.8: The calculated values of q and T in p-p collisions at 7 TeV and 900 GeV results for different hadron species.

Table 4.2: The calculated values of the T and q for different hadron species measured by the ALICE [11] and CMS collaborations [16] in p-p collisions at 900 GeV and 7 TeV using the Tsallis-B form for the momentum distribution.

Particle	q	T (GeV)
π^+ (0.9 TeV)	1.154 ± 0.036	0.0682 ± 0.0026
π^- (0.9 TeV)	1.146 ± 0.036	0.0704 ± 0.0027
K^+ (0.9 TeV)	1.158 ± 0.142	0.0690 ± 0.0223
K^- (0.9 TeV)	1.157 ± 0.139	0.0681 ± 0.0217
K^0_S(0.9 TeV)	1.134 ± 0.079	0.0923 ± 0.0139
K^0_S(7 TeV)	1.155 ± 0.061	0.1049 ± 0.0111
p (0.9 TeV)	1.107 ± 0.147	0.0730 ± 0.0425
$\bar{p}$(0.9 TeV)	1.106 ± 0.158	0.0764 ± 0.0464
Λ(0.9 TeV)	1.114 ± 0.047	0.0698 ± 0.0148
Λ(7 TeV)	1.119 ± 0.053	0.1169 ± 0.0188
Ξ^- (0.9 TeV)	1.110 ± 0.218	0.0440 ± 0.0752
Ξ^- (7 TeV)	1.112 ± 0.003	0.1622 ± 0.0379

We have compared results of the Tsallis-B distribution with the CMS and ALICE for the integrated particle yield dN/dy and average transverse momenta, $\langle p_T \rangle$ for central collision with various species of hadron, shown in Fig. 4.10 (a) and (b). According to Fig. 4.10 (a) and (b), most of the results are similar to

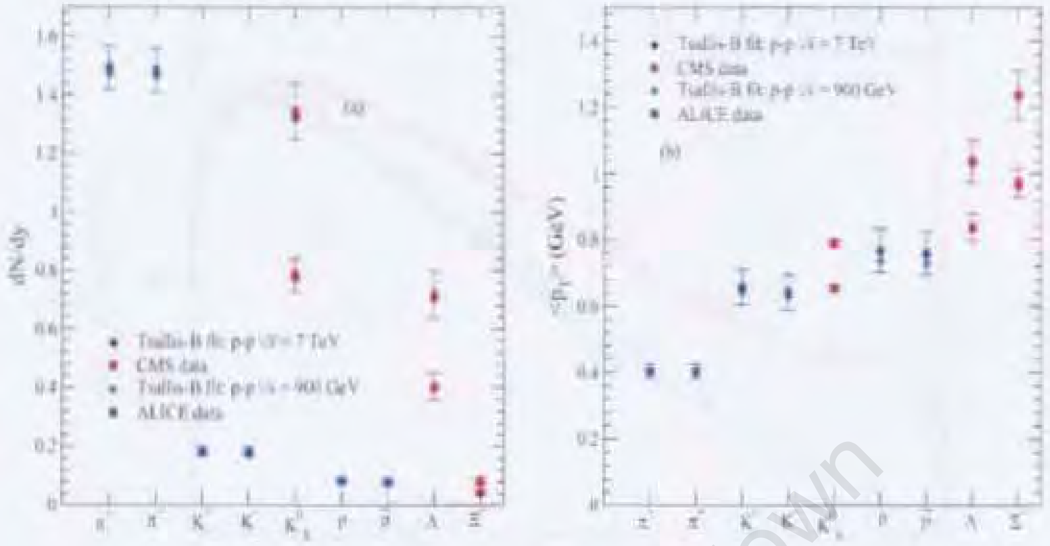

Figure 4.10: The particle yield at mid-rapidity, dN/dy and the average transverse momentum, $\langle p_T \rangle$ for different hadron species.

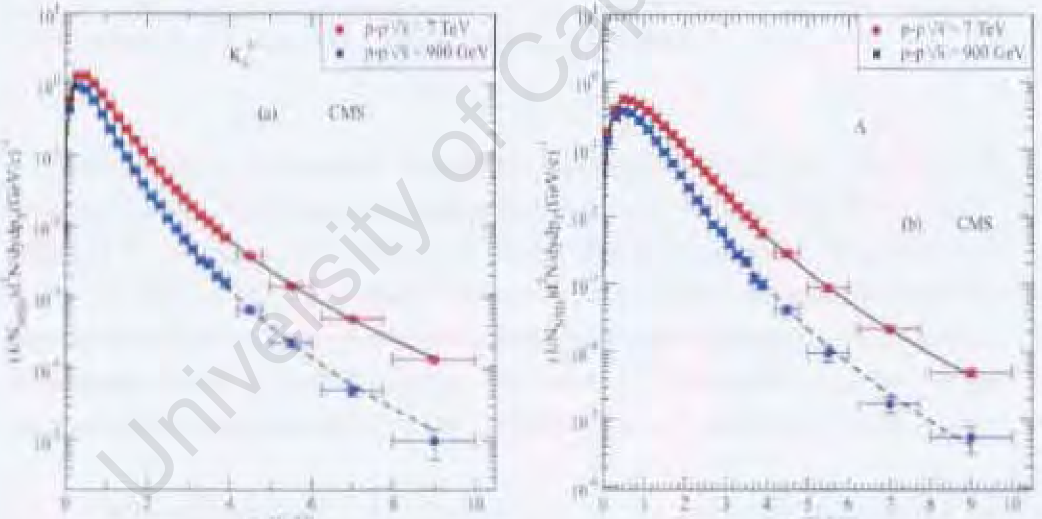

Figure 4.11: Comparison between the measured transverse momentum distribution for K^0_S and Λ as measured by the CMS collaboration [16] in p-p collision and the Tsallis-B distribution. The full and broken lines are fit using the parameterization Eq. (4.93) to the 7 TeV data while the dashed line is fit to the 0.9 TeV data with the parameters listed in Table 4.2.

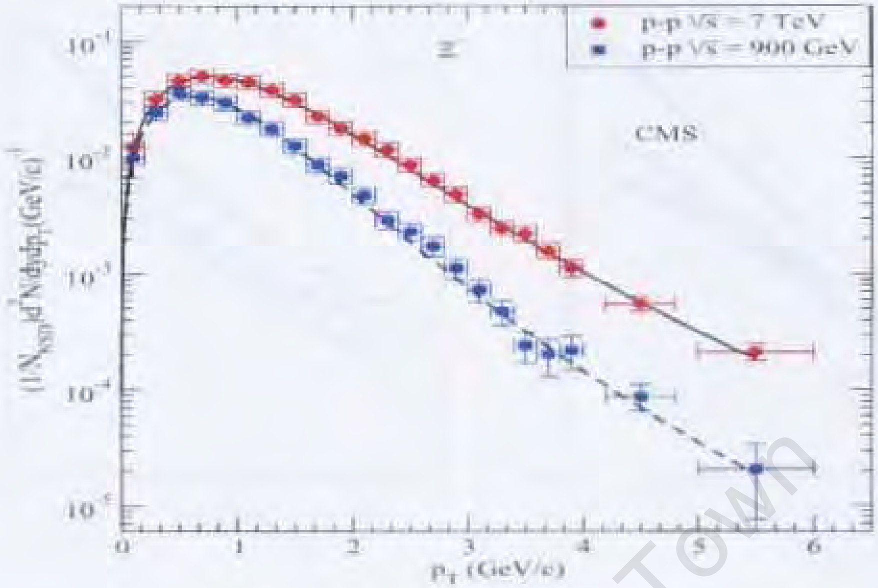

Figure 4.12: Comparison between the measured transverse momentum distribution for Ξ^- as measured by the CMS collaboration [16] in p-p collision and the Tsallis-B distribution. The full line is a fit using the parameterization Eq. (4.93) to the 7 TeV data while the dashed line is a fit to the 0.9 TeV data with the parameters listed in Table 4.2.

The calculated transverse momentum distribution using the Tsallis-B distribution for the experimental measurements from CMS and ALICE collaborations [11, 12, 16]: the p-p collisions at 0.9 and 7 TeV are presented in Figs 4.11, 4.12 and 4.13. The results are comparable with the ALICE collaboration results [11], but the resulting parameters are considerably different as presented in Table 4.2. Comparing Table 4.1 with Table 4.2, the values for q is slightly different for the same range of the q values (1.01 – 1.16) for both collisions considered in this chapter.

We have also presented the temperatures in p-p collisions in Table 4.2 for different hadron species. The temperature values are almost similar for various hadron species around 75 MeV with considerable deviations, it is however, well below the values quoted by the ALICE and CMS collaborations [11, 16].

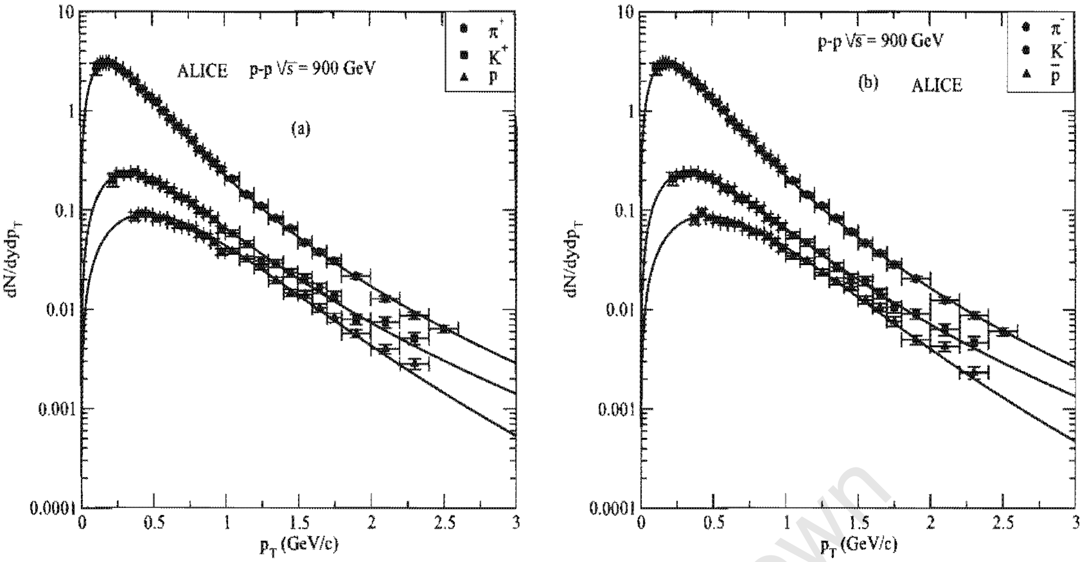

Figure 4.13: Comparison between the measured transverse momentum distribution for π^+, K^+, p, π^-, K^- and $\bar{p}$ as measured by the ALICE collaboration [11] in p-p collision and the Tsallis-B distribution. The full line is a fit using the parameterization Eq. (4.93) to the 0.9 TeV data with the parameters listed in Table 4.2.

The Pb-Pb collision at 2.76 TeV measured by the ALICE collaboration [12, 13] are presented in Figs. 4.14 and 4.15; these showed the relationship between the parameters obtained from the fit with parameter q, temperature, T and the radius factor, R for various hadron species. These parameters were extracted from the fitted Tsallis-B momentum distribution. The particle spectra results using Tsallis-B distribution in Pb-Pb collision at 2.76 TeV are presented in Figs.4.17 and 4.18.

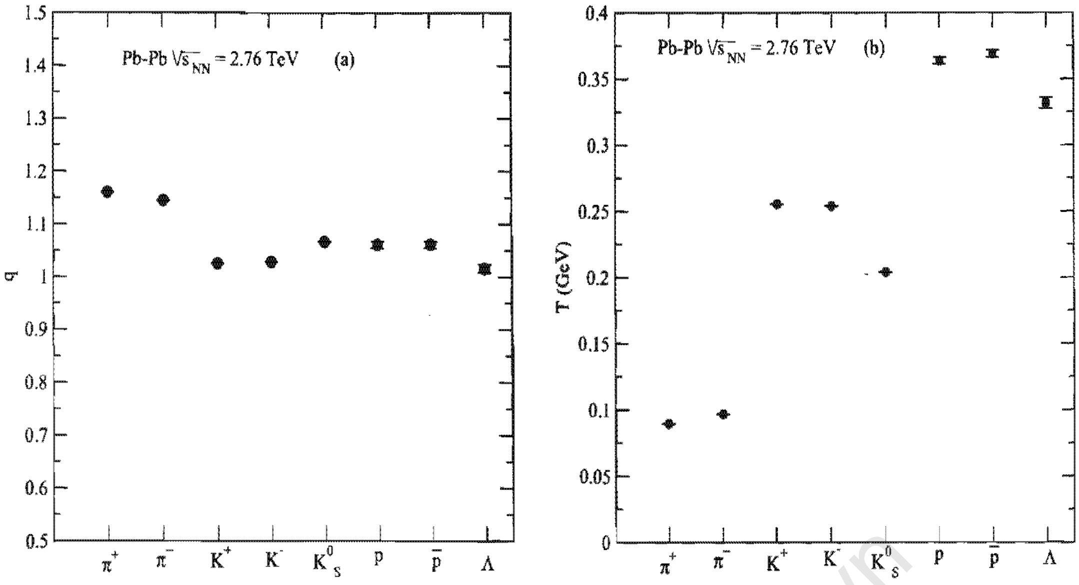

Figure 4.14: The calculated values for q and the temperature, T in Pb-Pb collision at 2.76 TeV results with different hadron species.

Table 4.3: Fitted values of the T and q for different hadron species measured by the ALICE [11, 12, 13] in Pb-Pb collision at 2.76 TeV using the Tsallis-B form for the momentum distribution.

Particle	q	T (GeV)
π^+	1.1609 ± 0.0002	0.0898 ± 0.0001
π^-	1.1452 ± 0.0002	0.0969 ± 0.0001
K^+	1.0255 ± 0.0015	0.2557 ± 0.0004
K^-	1.0276 ± 0.0015	0.2545 ± 0.0004
K^0_S	1.0666 ± 0.0008	0.2041 ± 0.0002
p	1.0605 ± 0.0065	0.3641 ± 0.0026
$\bar{p}$	1.0627 ± 0.0066	0.3691 ± 0.0026
Λ	1.0164 ± 0.0077	0.3318 ± 0.0042

Similarly, for various hadron species, Fig. 4.16 presents the integrated particle yield dN/dy and average transverse momenta, $\langle p_T \rangle$ for central collision $(0-5\%)$. According to the results in Fig. 4.16 (a) for the integrated particle yield dN/dy decrease as the mass of hadrons increases, however, Fig. 4.16 (b) for the average transverse momenta of the hadrons increase as the mass of hadrons increase.

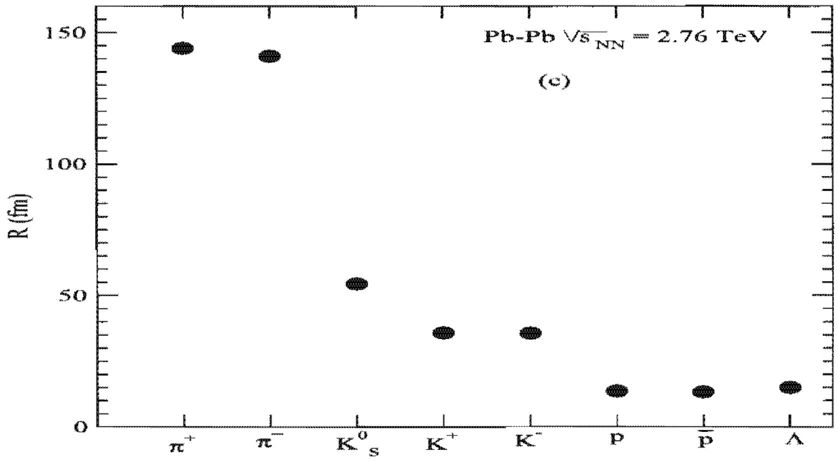

Figure 4.15: The calculated values for the radius, R in Pb-Pb collision at 2.76 TeV results with different hadron species.

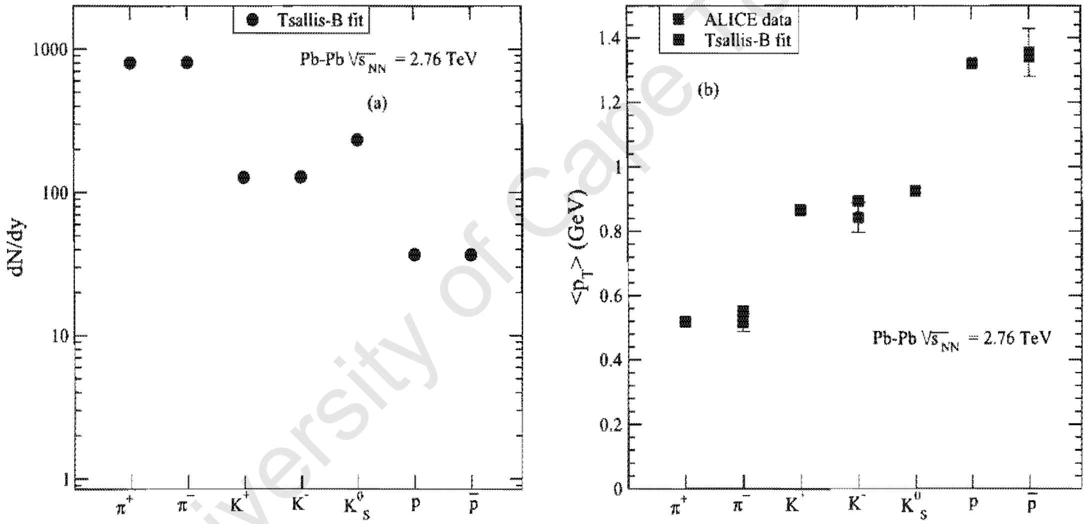

Figure 4.16: The particle yield at mid-rapidity, dN/dy and the average transverse momentum, $\langle p_T \rangle$ with different hadron species.

However, the Pb-Pb collision at 2.76 TeV presented in Table 4.3 which is the temperature values for various hadron species are higher than Au-Au and p-p collisions results, which are presented in Tables 4.1 and 4.2. Thus, we can deduce that the values of the temperature, T obtained from the fit in Pb-Pb collision are higher than the temperature, T values in Au-Au and p-p collision energies. The

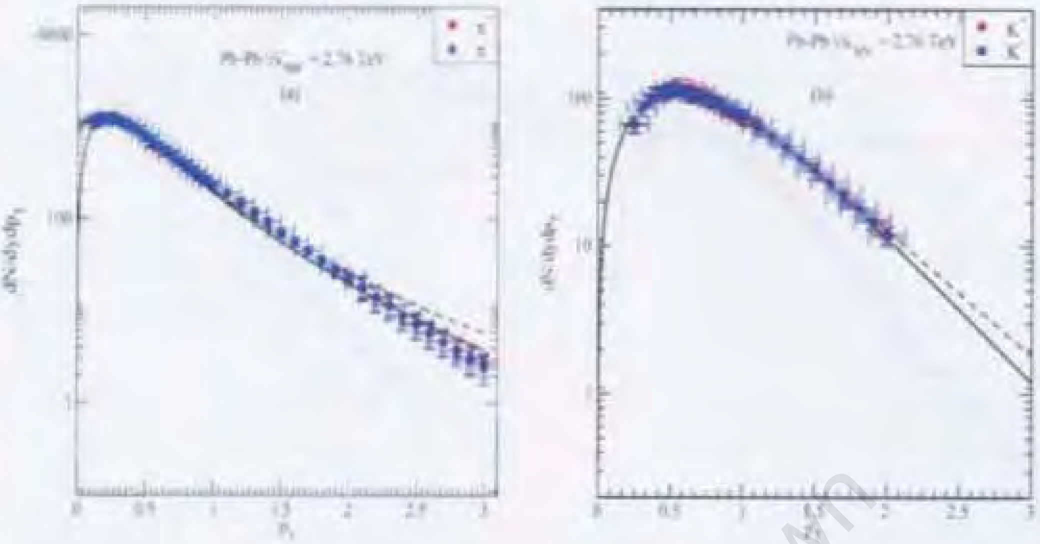

Figure 4.17: Comparison between the measured transverse momentum distribution for π^+ and π^- (left figure), K^+ and K^- (right figure) as measured by the ALICE collaboration [12] in Pb-Pb collision and the Tsallis-B distribution. The full and broken lines are a fit using the parameterization Eq. (4.93) to the 2.76 TeV data with the parameters listed in Table 4.3.

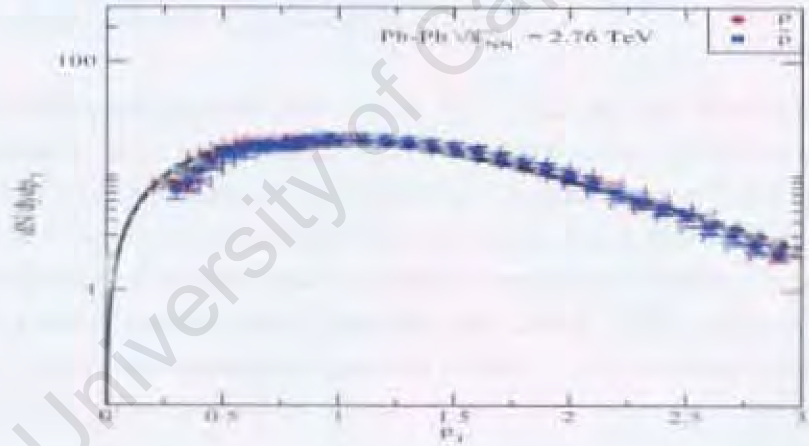

Figure 4.18: Comparison between the measured transverse momentum distribution for p and $\bar{p}$ as measured by the ALICE collaboration [12] in Pb-Pb collision and the Tsallis-B distribution. The full and broken lines are a fit using the parameterization Eq. (4.93) to the 2.76 TeV data with the parameters listed in Table 4.3.

possible reasons are due to higher values of particle spectra, average transverse momentum and the beam energy in Pb-Pb collision than Au-Au and p-p collisions.

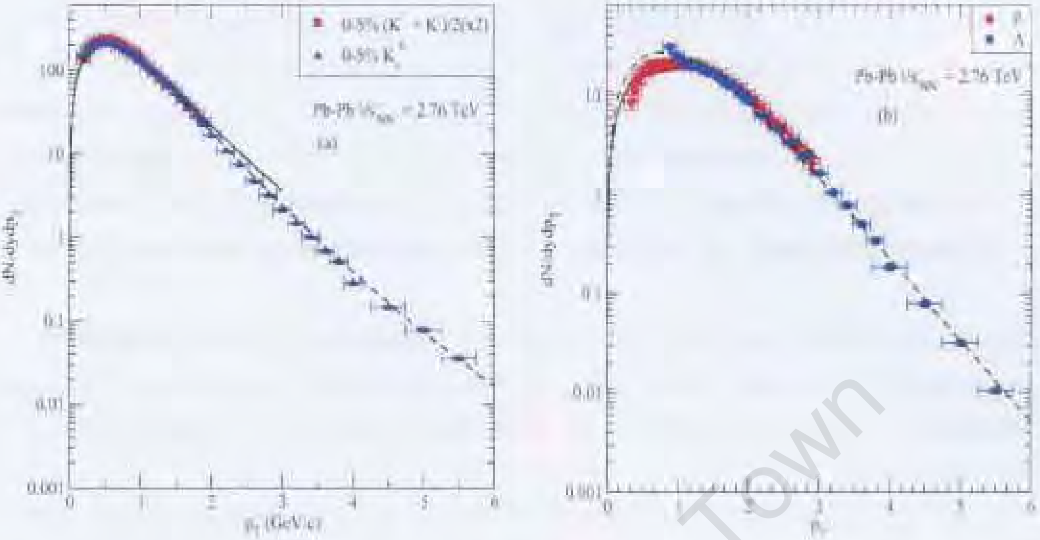

Figure 4.19: Comparison between the measured transverse momentum distribution for $(K^+ + K^-)/2$ and K_s^0, p and Λ as measured by the ALICE collaboration [12] in Pb-Pb collision and the Tsallis-B distribution. The full and broken lines are a fit using the parameterization Eq. (4.93) to the 2.76 TeV data with the parameters listed in Table 4.3.

The integrated particle yield dN/dy ($|y| < 0.5$) and the average transverse momentum, $< p_T >$ are obtained from the fits with various hadrons species measured by the ALICE collaboration [12] in Pb-Pb collision at 2.76 TeV using the Tsallis-B form for the momentum distribution. In Fig. 4.19(a) and (b) presents the comparison of the transverse momentum correlation between K^+ and K_s^0 as well as p and Λ particles that are emitted from central Pb-Pb collisions at $\sqrt{s_{NN}}$ = 2.76 TeV. These correlations have been studied by the NA49 experiment at the CERN SPS [133].

The most striking feature is that the values of the parameter q are fairly stable in the range 1.01 to 1.2 with the error bars for various hadron species which are considered at various collision energies (0.2 TeV, 0.9 TeV, 2.76 TeV and 7 TeV); the results are presented in Figs. 4.4(a), 4.8(a) and 4.14(a). The same cannot be said about the temperature T in the range 70 MeV - 150 MeV with considerable deviations. The values of T cannot be determined very accurately for all hadrons, but are consistent with a value around 70 MeV (mostly) and with maximum value up to 370 MeV in Pb-Pb collision energy.

For clarity we will show the results in Figs. 4.4, 4.5, 4.8, 4.9, 4.14 and 4.15 for the values of the parameters q, the temperature, T and the radius, R with different hadron species. In most cases, the temperature values are well below the values quoted by the STAR, CMS and ALICE collaborations [11, 12, 13, 16, 23]. The radius factor R as shown in Figs. 4.5, 4.9 and 4.15 can be interpreted as the radius of the system as one expects contributions from the decays of resonances.

According to the experimental results by the CMS and ALICE collaborations [11, 12, 16] in p-p collisions at 900 GeV and 7 TeV as well as Pb-Pb collision at 2.76 TeV results which were fitted using the Tsallis-B distribution are shown in Figs. (4.11 - 4.13) and (4.17 - 4.19) respectively. In general, our results are similar with those shown by the STAR, CMS and ALICE results [11, 13, 14, 16]. However, the resulting parameters are considerably different from those obtained from Eq. (4.73) and we have collected those parameter results for each collision in Tables 4.1, 4.2 and 4.3.

In most cases, the χ^2 value is used to compare between the experimental data and the model. If $x_1, \ldots, x_N$ and $y_1, \ldots, y_N$ are values of the model and measured variables respectively. χ^2 is defined by the sum of variables

$$\chi^2 = \sum_{i=1}^{N} \left(\frac{x_i - y_i}{\sigma_i} \right)^2 \tag{4.96}$$

where σ_i is the error on the measured value y_i and N is number of samples.

We present the χ^2 analysis for Au-Au collision at 200 GeV, p-p collisions at 900 GeV and 7 TeV as well Pb-Pb collision at 2.76 TeV. The values for χ^2/ndf at different beam energies for various hadron species are found in Tables 4.4 and 4.5.

When estimating parameters using the method of least squares, one tries to obtain the minimum value of the quantity χ^2 Eq. (4.96). This quantity provides a measure of the significance of the discrepancy between the data and the hypothesized functional form used in the fit, we have presented in Tables 4.4 and 4.5 for Au-Au, p-p and Pb-Pb collisions respectively. Note that, in the χ^2 calculations,

Table 4.4: The calculated values of χ^2/ndf with the Tsallis-B distribution for different hadron species in Au-Au collision at 200 GeV measured by the STAR collaboration [14].

Particle	χ^2/ndf (Tsallis-B)
π^+	0.604/8
π^-	2.382/8
K^+	0.641/7
K^-	0.574/7
p	0.305/13
$\bar{p}$	9.526/13

the difference between N and number of fit parameters is called number of degrees of freedom (ndf).

One aspect in analyzing the experimental results is to apply the χ^2 calculation to compare with the model. The χ^2/ndf is a measure of how good is the agreement between theory and experiment. According to the parameters shown in Tables 4.1, 4.2 and 4.3, the χ^2 analysis show that the p_T spectra is best described in the specified range as shown in Tables 4.4 and 4.5. Further, the results of Tsallis-B distribution for χ^2/ndf have been compared with [11, 16] in p-p collisions which is listed in Table 4.5. Thus, The χ^2/ndf is smaller than unity because the point-to-point errors are not included in the fit and are estimated only based on the data points but most of the fits at different collisions were within the error bar; these were presented in Figs. 4.7, 4.11, 4.12, 4.13, 4.17, 4.18 and 4.19. If the χ^2/ndf is scaled such that the minimum is unity, then somewhat smaller statistical errors on the fit parameters are obtained.

In general, for various hadron species the increment of the average transverse momentum is higher in heavy ion collisions than the elementary collisions as shown in Figs. 4.6 (b), 4.10 (b) and 4.16 (b). The transverse momentum spectra for identified particles in Au-Au, p-p and Pb-Pb collision results at mid-rapidity have been presented. These spectra are inspired by using a Tsallis-B distribution in order to fit the spectra of identified hadrons to give a freeze-out temperature, the average transverse momentum and particle yield at mid-rapidity.

Table 4.5: The comparison between the calculated values of χ^2/ndf using the Tsallis-B distribution with the CMS and ALICE collaborations result for p-p collisions at 900 and 7000 GeV as well Pb-Pb collision at 2.76 TeV [11, 13, 16] for strange and nonstrange particles.

p-p collisions $\sqrt{s} = 900$ GeV and 7 TeV Particle	χ^2/ndf (Tsallis-B)	χ^2/ndf (CMS)
K_S^0 (900 GeV)	14.41/21	19/21
K_S^0 (7TeV)	7.19/21	50/21
Λ(900 GeV)	8.45/21	32/21
Λ (7 TeV)	5.98/21	128/21
Ξ^- (900 GeV)	10.09/19	19/19
Ξ^- (7 TeV)	3.71/19	21/19

p-p collision $\sqrt{s} = 900$ GeV Particle	χ^2/ndf (Tsallis-B)	χ^2/ndf (ALICE)
π^+	12.01/30	14.23/30
π^-	13.28/30	12.46/30
K^+	16.25/24	12.71/24
K^-	7.06/24	6.23/24
p	14.77/21	13.79/21
$\bar{p}$	13.18/21	13.46/21

Pb-Pb collision $\sqrt{s_{NN}} = 2.76$ TeV Particle	χ^2/ndf (Tsallis-B)
π^+	13.72/38
π^-	13.62/38
K^+	3.92/23
K^-	2.98/23
K_s^0	14.73/29
p	17.55/31
$\bar{p}$	17.95/31
Λ	14.41/22

The spectra and hadronic yield fit to Tsallis-B statistical model show that the chemical freeze-out temperature, average transverse momentum and particle yield are dependent on the system size and energy for Au-Au collision at 200 GeV, p-p collisions at 900 GeV and 7 TeV as well as Pb-Pb collision at 2.76 TeV.

Chapter 5

Conclusions

In conclusion, the statistical thermal models have been successful in describing particle yields at different beam energies in elementary and heavy ion collisions [5, 104, 134]. These models assume the formation of a system, which is in thermal and chemical equilibrium in the hadronic phase, and is characterized by a set of thermodynamic variables. The most important among these are the chemical freeze-out temperature and baryon chemical potential. The time evolution of the deconfined quarks and gluons remains hidden: full equilibration generally washes out and destroys large amounts of information about the early deconfined phase.

In this thesis we have made a new analysis of the number of hadronic resonances using the latest information from the Particle Data Group [9]. This leads to a temperature which is consistent with the most recent results based on lattice QCD estimates of the phase transition temperature [71, 78] and also the chemical freeze-out temperature at zero baryon density [22, 63, 64]. We have extended the calculations of the speed of sound to non-zero baryon and strangeness chemical potentials keeping s/n fixed [74]. This is done for both the hadronic resonance gas model (HRGM) and the extended hadronic resonance gas model (EHRGM) which includes the exponentially increasing spectrum of hadrons following the Hagedorn parametrization. The EHRGM shows that the speed of sound goes to zero at the phase transition point while the HRGM shows a smooth dip followed by an increase in temperatures and baryon chemical potentials.

The purpose of EHRGM is to confront the results of recent lattice calculations performed with light quark masses with the prediction of the HRGM and EHRGM and determine its range of applicability. As we saw, the HRGM and EHRGM describe thermodynamic quantities quite well up to unexpectedly high temperatures [19].

Furthermore, we managed to extend the previous particle data table (2002 particle data table [24]) constructed by S. Wheaton and implemented in THERMUS [22]. Mostly charm and bottom particles are included in the 2008 particle data table, created their decay elements and used the grand-canonical ensemble to analyze the results. We also explained how to implement THERMUS with the extended particle data table; and compared some results with [22]. In addition, we presented the study of particle yields and particle ratios for various collision energies along the freeze-out curve [4, 5].

We have analyzed and discussed the hadronic abundances measured in Au-Au, p-p and Pb-Pb collisions at RHIC and LHC experiments using THERMUS. The results were obtained with two particle data tables, and their differences were explained. In particular, the data from the RHIC experiment for Au-Au collisions at 130 GeV and 200 GeV were discussed and analyzed. Similarly, using the preliminary particle yield results of p-p collisions at 0.9 TeV and 7 TeV as well as Pb-Pb collision at 2.76 TeV [11, 12, 13] particle yield calculations were presented and the thermodynamic parameters were obtained from the fits.

The thermal parameters obtained from THERMUS were used to fit the preliminary experimental results from p-p and Pb-Pb collisions at the LHC. The freeze-out temperature was found to be between 150 MeV and 175 MeV. This occurred within a wide range of beam energies (i.e., 0.2, 0.9, 2.76 and 7) TeV, different type of collisions (i.e., p-p, Au-Au and Pb-Pb) and parameters. The parameters such as the freeze-out temperature, strangeness saturation factor, fireball radius, baryon chemical potential and strangeness chemical potential were well parameterized to within small uncertainties. They were also compared with [5, 109] as a function of energy.

Finally, we have presented a detailed derivation of the quantum form of the

Tsallis distribution and considered the thermodynamic consistency of the resulting distribution in detail. We emphasized that an additional power of q is needed to achieve consistency with the laws of thermodynamics [113]. The resulting distribution, called Tsallis-B distribution, was compared with recent measurements from STAR [14] at the RHIC as well as the ALICE [11] and CMS [16] collaborations at the LHC and good agreement was obtained. Based on the Tsallis-B distribution, we have determined from the fit; the estimates of the parameter q, the temperature T and the radius factor R that comes from the volume factor V. Hence, the resulting parameter q which is a measure for the deviation from a standard Boltzmann distribution was found to be around 1.11. The resulting values of the temperature show a wider spread around 100 MeV [17, 18].

Appendix A

Hadron mass spectrum data table

The hadron masses can be expressed in terms of mass spectrum (MS) and its logarithmic form of MS. This is arranged in table A1 up to mass 2 GeV.

Mass(GeV)	MS	ln(MS)	Mass(GeV)	MS	ln(MS)
0.13957	3	1.09861	1.58	372	5.91889
0.493677	5	1.60944	1.594	375	5.92693
0.497614	7	1.94591	1.6	439	6.08450
0.54785	8	2.07944	1.617	444	6.09582
0.67	12	2.48491	1.63	460	6.13123
0.775	21	3.04452	1.639	465	6.14204
0.78259	24	3.17805	1.647	474	6.16121
0.89166	30	3.40120	1.65	494	6.20254
0.896	36	3.58352	1.66	506	6.22654
0.938272	40	3.68888	1.662	515	6.24417
0.939656	44	3.78419	1.667	522	6.25767
0.95766	45	3.80666	1.67	589	6.37843
0.98	46	3.82864	1.6724	604	6.40357
0.9847	49	3.89182	1.67245	612	6.41673
1.01946	52	3.95124	1.675	636	6.45520
1.11568	56	4.02535	1.68	663	6.49677
1.17	59	4.07754	1.6888	684	6.52796
1.18937	63	4.14313	1.69	692	6.53959
1.19264	67	4.20469	1.7	756	6.62804

1.19745	71	4.26268	1.71	764	6.63857
1.2295	80	4.38203	1.717	776	6.65415
1.23	89	4.48864	1.72	801	6.68586
1.232	121	4.79579	1.724	802	6.68711
1.271	133	4.89035	1.732	817	6.70564
1.2751	138	4.92725	1.75	829	6.72022
1.2818	141	4.94876	1.756	830	6.72143
1.294	142	4.95583	1.773	850	6.74524
1.3	145	4.97673	1.775	886	6.78672
1.31486	149	5.00395	1.776	914	6.81783
1.3183	164	5.09987	1.8	926	6.83087
1.32171	168	5.12396	1.81	934	6.83948
1.35	169	5.12990	1.815	939	6.84482
1.351	178	5.18178	1.816	961	6.86797
1.3828	186	5.22575	1.82	993	6.90073
1.3837	194	5.26786	1.83	1009	6.91672
1.386	197	5.28320	1.842	1014	6.92166
1.3872	205	5.32301	1.854	1021	6.92854
1.403	211	5.35186	1.86484	1022	6.92952
1.406	215	5.37064	1.86962	1024	6.93147
1.4098	216	5.37528	1.8751	1030	6.93731
1.412	220	5.39363	1.89	1106	7.00851
1.414	232	5.44674	1.9	1122	7.02287
1.425	235	5.45959	1.903	1127	7.02731
1.4256	245	5.50126	1.905	1175	7.06902
1.4264	248	5.51343	1.909	1178	7.07157
1.4324	258	5.55296	1.91	1210	7.09838
1.44	270	5.59842	1.915	1246	7.12769
1.453	275	5.61677	1.92	1316	7.18235
1.46	279	5.63121	1.93	1422	7.25982
1.465	288	5.66296	1.94	1446	7.27656
1.474	291	5.67332	1.944	1451	7.28001
1.476	292	5.67675	1.945	1455	7.28276
1.505	293	5.68017	1.95	1519	7.32581
1.518	298	5.69709	1.96	1567	7.35692

1.5195	306	5.72359	1.96849	1569	7.35819
1.52	322	5.77455	1.973	1573	7.36074
1.525	327	5.78996	1.982	1594	7.37400
1.5318	335	5.81413	1.992	1595	7.37463
1.535	347	5.84932	2.001	1622	7.39142
1.562	352	5.86363			

Table A1. The list of hadron masses, Mass Spectrum (MS) and their logarithmic form of MS for hadron masses from pion mass until 2 GeV data.

Appendix B

Energy Density for a Hadron Gas

The partition function for HRGM using the Boltzmann distribution is given by

$$\ln Z = \frac{gV}{2\pi^2} \int_0^\infty p^2 dp \; e^{\left(\frac{-E+\mu}{T}\right)}. \tag{B.1}$$

Taking $E = \sqrt{p^2 + m^2}$, $p = m\sinh(y), E = m\cosh(y), dp = m\cosh(y)dy$ and defining $\frac{m}{T} = l$, we have

$$\ln Z = \frac{gVT^3 l^3}{2\pi^2} e^{\left(\frac{\mu}{T}\right)} \int_0^\infty \sinh^2(y)\cosh(y) \exp\left(\frac{-m\cosh(y)}{T}\right) dy. \tag{B.2}$$

Using the definitions $\cosh(y) = \frac{e^y + e^{-y}}{2}$ and $\sinh(y) = \frac{e^y - e^{-y}}{2}$, we have

$$\sinh^2(y) = \frac{e^{2y} + e^{-2y} - 2}{4}. \tag{B.3}$$

now for the integrand

$$\sinh^2(y)\cosh(y) = \frac{e^{3y} + e^{-3y} - e^y - e^{-y}}{8} \quad = \quad \frac{1}{4}[\cosh(3y) - \cosh(y)]. \tag{B.4}$$

substituting this back into Eq. $(B.2)$ gives

$$\ln Z = \frac{gVT^3 l^3}{2\pi^2}\frac{1}{4}\left[\int_0^\infty (\cosh(3y) - \cosh(y)) \; e^{-l\cosh(y)} dy\right] e^{\left(\frac{\mu}{T}\right)} \tag{B.5}$$

Using the following definitions for the modified Bessel functions

$$K_\nu(z) = \int_0^\infty e^{-z\cosh(t)}\cosh(\nu t)dt, \tag{B.6}$$

$$K_{\nu+1}(z) = \frac{2\nu}{z}K_\nu(z) + K_{\nu-1}(z), \tag{B.7}$$

and

$$\frac{\partial K_2}{\partial T} = \frac{1}{T}[2K_2 + \frac{m}{T}K_1], \tag{B.8}$$

we have

$$\ln Z = \frac{gVT^3l^3}{2\pi^2}\frac{1}{4}[K_3(l) - K_1(l)] \tag{B.9}$$

but from Eq. $(B.7)$

$$[K_3(l) - K_1(l)] = \frac{4}{l}K_2(l). \tag{B.10}$$

thus the partition function is given by

$$\ln Z = \frac{gVTm^2}{2\pi^2}K_2(\frac{m}{T})e^{\frac{\mu}{T}}. \tag{B.11}$$

The energy density is defined by [19]

$$\varepsilon = \frac{T^2}{V}\frac{\partial \ln Z}{\partial T} + \frac{\mu T}{V}\frac{\partial \ln Z}{\partial \mu} \tag{B.12}$$

We can define A and B as follows:

$$A = \frac{T^2}{V}\frac{\partial \ln Z}{\partial T}, \quad B = \frac{\mu T}{V}\frac{\partial \ln Z}{\partial \mu}. \tag{B.13}$$

For the first part A

$$\begin{aligned} \frac{\partial \ln Z}{\partial T} &= \frac{\partial}{\partial T}\left[\frac{gVTm^2}{2\pi^2}K_2\left(\frac{m}{T}\right)\exp\left(\frac{\mu}{T}\right)\right] && \text{(B.14)} \\ &= \frac{gVm^2}{2\pi^2}\left[K_2 - \frac{\mu}{T}K_2 + T\frac{\partial K_2}{\partial T}\right]\exp\left(\frac{\mu}{T}\right) && \text{(B.15)} \\ \text{using } \frac{\partial K_2}{\partial T} &= \frac{1}{T}\left[2K_2 + \frac{m}{T}K_1\right] \text{ gives} && \text{(B.16)} \\ A &= \frac{gT^2m^2}{2\pi^2}\left[3K_2 + \frac{m}{T}K_1 - \frac{\mu}{T}K_2\right]\exp\left(\frac{\mu}{T}\right) && \text{(B.17)} \end{aligned}$$

Now for the second part (B)

$$\frac{\mu T}{V}\frac{\partial \ln Z}{\partial \mu} = \frac{\mu T}{V}\left(\frac{gVTm^2}{2\pi^2}K_2\right)\frac{1}{T}\exp\left(\frac{\mu}{T}\right) \tag{B.18}$$

$$= \mu\left(\frac{gTm^2}{2\pi^2}K_2\right)\exp\left(\frac{\mu}{T}\right) \tag{B.19}$$

To obtain the energy density, we add A and B to get after simplifying

$$\varepsilon = \frac{gT^2m^2}{2\pi^2}\left(3K_2 + \frac{m}{T}K_1\right)\exp\left(\frac{\mu}{T}\right) \tag{B.20}$$

Appendix C

Derivation of Non-extensive Formalisms

C.1 Tsallis Entropy

The postulated form of the generalized entropy [44] is:

$$S_q \equiv \frac{1 - \sum_{i=1}^{W} \exp(q \ln P_i)}{q-1}, \; (q \in \Re; \; \sum_{i=1}^{W} P_i = 1), \tag{C.1}$$

This Tsallis form of entropy can be written in the form BG entropy, S_{BG}. This happens when the limit q tends to 1. Which is

$$S_{BG} = \lim_{q \to 1} S_q \equiv \lim_{q \to 1} - \sum_{i=1}^{W} \ln(P_i) \exp(q \ln P_i), \tag{C.2}$$

then,

$$S_{BG} = \lim_{q \to 1} S_q \equiv - \sum_{i=1}^{W} P_i \ln(P_i). \tag{C.3}$$

We define function $\exp_q(x)$, for $q > 1$ as

$$\exp_q(x) \equiv \begin{cases} [1 + (q-1)x]^{1/(q-1)} & \text{if} \quad x > 0 \\ [1 + (1-q)x]^{1/(1-q)} & \text{if} \quad x \leq 0. \end{cases} \tag{C.4}$$

Using similar method given in Eq. (C.2), we can derive the function $\exp_q(x)$ in the limit where q tends to 1, which is

$$\lim_{q\to 1}\exp_q(x) = \exp(x) \equiv \begin{cases} \lim_{q\to 1}\left[1+(q-1)x\right]^{1/(q-1)} & \text{if} \quad x > 0 \\ \lim_{q\to 1}\left[1+(1-q)x\right]^{1/(1-q)} & \text{if} \quad x \leq 0, \end{cases} \tag{C.5}$$

we rewrite Eq. (C.5) in the following form

$$\ln\left(\exp(x)\right) \equiv \begin{cases} \lim_{q\to 1}\frac{\ln[1+(q-1)x]}{(q-1)} & \text{if} \quad x > 0 \\ \lim_{q\to 1}\frac{\ln[1+(1-q)x]}{(1-q)} & \text{if} \quad x \leq 0, \end{cases} \tag{C.6}$$

since Eq. (C.6) satisfies L'Hospital's limit rule [135], then

$$\ln\left(\exp(x)\right) \equiv \begin{cases} \lim_{q\to 1}\frac{x}{1+(q-1)x} & \text{if} \quad x > 0 \\ \lim_{q\to 1}\frac{-x}{1+(1-q)x} & \text{if} \quad x \leq 0, \end{cases} \tag{C.7}$$

finally, by rearranging Eq. (C.7) can give us the usual form of exponential;

$$\exp(x) \equiv \begin{cases} \exp(x) & \text{if} \quad x > 0 \\ \exp(-x) & \text{if} \quad x \leq 0. \end{cases} \tag{C.8}$$

C.2 q-Exponential and q-Logarithm Functions

Let us be more detailed about the above definitions stated in chapter 4. For $q < 1$, the q-exponential function vanishes for $x \leq -1/(1-q)$ and continuous and monotonically increases from 0 to ∞ when x increases from $-1/(1-q)$ to ∞. For $q > 1$, the q-exponential function continuous and monotonically increases from 0 to ∞ when x increases from $-\infty$ to $1/(q-1)$, remaining divergent for $x > 1/(q-1)$ [112]. See Fig. 4.1. The following property is satisfied:

$$\left[e_{1/q}^{-qx}\right]^{1/q} = \frac{1}{e_q^x} \quad (\forall x; \forall q), \tag{C.9}$$

or, equivalent and more symmetrically,

$$\left[e_q^{x/q^{1/2}}\right]^{q^{1/2}} e_{1/q}^{-q^{1/2}x^{1/q^{1/2}}} = 1 \quad (\forall x; \forall q). \tag{C.10}$$

Other interesting properties are:

$$e_q^{x+y+(-q)xy} = e_q^x e_q^y \quad (\forall(x,y);\forall q), \tag{C.11}$$

and

$$\ln_q(xy) = \ln_q x + \ln_q y + (1-q)(\ln_q x)(\ln_q y) \quad (\forall(x,y);\forall q) \tag{C.12}$$

as well as, the following expansions are useful in a variety of applications:

$$\frac{d}{dx} e_q^x = \left(e_q^x\right)^q \quad (\forall x;\forall q), \tag{C.13}$$

$$\frac{d}{dx} \ln_q x = \frac{1}{x^q} \quad (\forall x;\forall q), \tag{C.14}$$

$$\ln_q\left(\frac{x}{y}\right) = \frac{1}{y^{1-q}}\left[\ln_q x - \ln_q y\right] \quad (\forall(x,y);\forall q), \tag{C.15}$$

$$\ln_q \frac{1}{x} = -\frac{1}{x^{1-q}} \ln_q x \quad (\forall x;\forall q). \tag{C.16}$$

References

[1] R. Hagedorn. Statistical thermodynamics of strong interactions at high-energies. *Nuovo Cim. Suppl.*, 3:147–186, 1965.

[2] R. Hagedorn. *Riv. Nuovo Cimento*, **6**(10), 1984.

[3] R. Hagedorn. Hadronic matter near the boiling point. *Nuovo Cim.*, 56A:1027–1057, 1968.

[4] J. Cleymans and K. Redlich. Chemical and thermal freeze-out parameters from $1A$ to $200A$ GeV. *Phys. Rev. C*, 60:054908, Oct 1999.

[5] J. Cleymans, H. Oeschler, K. Redlich, and S. Wheaton. Comparison of chemical freeze-out criteria in heavy-ion collisions. *Phys. Rev.*, C73:034905, 2006.

[6] S. Chatterjee, R. M. Godbole, and Sourendu Gupta. Stabilizing hadron resonance gas models. *Phys. Rev.*, C81:044907, 2010.

[7] Wojciech Broniowski, Wojciech Florkowski, and Leonid Ya. Glozman. Update of the Hagedorn mass spectrum. *Phys. Rev. D*, 70(11):117503, Dec 2004.

[8] S. Wheaton, J. Cleymans, and M. Hauer. THERMUS: A Thermal model package for ROOT. *Comput.Phys.Commun.*, 180:84–106, 2009, http://www.phy.uct.ac.za/courses/staffwebsites/wheaton/THERMUS/thermus_index.html.

[9] Claude Amsler et al. Review of particle physics. *Phys. Lett.*, B667:1–1340, 2008.

[10] J. Manninen and F. Becattini. Chemical freeze-out in ultra-relativistic heavy ion collisions at $\sqrt{s_{NN}} = 130$ and 200 GeV. *Phys. Rev.*, C78:054901, 2008.

[11] K. Aamodt and others (ALICE Collaboration). Production of pions, kaons and protons in p-p collisions at $\sqrt{s}$= 900 GeV with ALICE at the LHC. *Eur. Phys. J.*, C71:1655, 2011.

[12] M. Floris and for the ALICE Collaboration. Identified particles in p-p and Pb-Pb collisions at LHC energies with the ALICE detector. *J.Phys.G*, G38:124025, 2011.

[13] A. Kalweit (ALICE Collaboration). Global properties of strange particle production in p-p and pb-pb collisions with the alice detector. *Talk presented at SQM2011, Cracow, Poland.*

[14] B. I. Abelev et al. Strange particle production in p-p collisions at $\sqrt{s} = 200$ GeV. *Phys. Rev.*, C75:064901, 2007.

[15] A. Adare *et al.* [PHENIX Collaboration]. Identified charged hadron production in p-p collisions at $\sqrt{s} = 200$ and 62.4 GeV. *Phys. Rev. C*, 83:064903, June 2011.

[16] Vardan Khachatryan et al. Strange Particle Production in p-p Collisions at $\sqrt{s} = 0.9$ and 7 TeV. *JHEP*, 05:064, 2011.

[17] J. Cleymans and D. Worku. The Tsallis Distribution and Transverse Momentum Distributions in High-Energy Physics. arXiv:hep-ph/1106.3405 2011.

[18] J. Cleymans and D. Worku. The Tsallis Distribution in Proton-Proton Collisions at $\sqrt{s} = 0.9$ TeV at the LHC. *Journal of Physics G: Nuclear and Particle Physics*, 39(2):025006, 2012, eprint:arXiv:hep-ph/1110.5526, 2011.

[19] J. Cleymans and D. Worku. The Hagedorn temperature Revisited. *Mod. Phys. Lett.*, A26:1197–1209, 2011.

[20] J. I. Kapusta and E. S. Bowman. Multiple Critical Points in the QCD Phase Diagram. *PoS*, CPOD2009:018, 2009.

[21] J.I. Kapusta and E.S. Bowman. Critical points in the QCD phase diagram with two flavors of quarks. *Nuclear Physics A*, 830(1-4):721c – 724c, 2009.

Quark Matter 2009 - The 21st International Conference on Ultrarelativistic Nucleus-Nucleus Collisions.

[22] S. Wheaton. The development and application of `THERMUS- a Statistical-Thermal Model Analysis Package for ROOT`. *Ph.D. thesis, University of Cape Town*, Cape Town, South Africa, 2005.

[23] B. I. Abelev *et al.* [STAR Collaboration]. Systematic Measurements of Identified Particle Spectra in p-p, d^+-Au and Au-Au Collisions from STAR. *Phys.Rev.*, C79:034909, 2009.

[24] K. Hagiwara et al. Review of Particle Properties. *Phys. Rev. D*, 66(1):010001, Jul 2002.

[25] J.I. Kapusta. *Finite-temperature field theory.* Cambridge monographs on mathematical physics. Cambridge University Press, 1989.

[26] A. Andronic and P. Braun-Munzinger. Ultrarelativistic nucleus nucleus collisions and the quark-gluon plasma. *Lect. Notes Phys.*, 652:35–68, 2004.

[27] Ramona Vogt. *Ultrarelativistic Heavy-Ion Collisions.* Elsevier: Linacre House, Jordan Hill, Oxford OX2 8DP, UK, 2007.

[28] Edward V. Shuryak. *The QCD Vacuum, Hadrons and Superdense Matter.* World Scientific Lecture Notes in Physics - Vol. 71, second edition, 2004.

[29] W. Florkowski. *Phenomenology of Ultra-Relativistic Heavy-Ion Collisions.* World Scientific Pub Co Inc, 2010.

[30] J. Cleymans and H. Satz. Thermal hadron production in high-energy heavy ion collisions. *Z. Phys.*, C57:135–148, 1993.

[31] P. Braun-Munzinger, J. Stachel, J. P. Wessels, and N. Xu. Thermal Equilibration and Expansion in Nucleus-Nucleus Collision at the AGS. *Phys. Lett. B*, 344:43, 1995.

[32] J. Cleymans, D. Elliott, H. Satz, and R. L. Thews. Thermal hadron production in Si-Au collisions. *Z. Phys.*, C74:319–324, 1997.

[33] J. Cleymans and K. Redlich. Unified description of freeze-out parameters in relativistic heavy ion collisions. *Phys. Rev. Lett.*, 81:5284–5286, 1998.

[34] F. Becattini, J. Cleymans, A. Keranen, E Suhonen, and K. Redlich. Features of particle multiplicities and strangeness production in central heavy ion collisions between 1.7-A- `GeV`/c and 158-A-`GeV`/c. *Phys. Rev.*, C64:024901, 2001.

[35] Wojciech Florkowski, Wojciech Broniowski, and Mariusz Michalec. Thermal analysis of particle ratios and p_T spectra at RHIC. *Acta Phys. Polon.*, B33:761–769, 2002.

[36] K. Huang. *Quarks, Leptons and Gauge fields, 2nd edition.* World Scientific, Singapore, 1992.

[37] D.J. Griffiths. *Introduction to Elementary Particles.* John Wiley and Sons, 1987.

[38] D. H. Perkins. *Introduction to High Energy Physics.* Cambridge Univ. Press, Cambridge, 2000.

[39] Jean Letessier and Johann Rafelski. *Hadrons and Quark-Gluon Plasma.* Cambridge University Press, second edition, 2004.

[40] Siegfried Bethke. Experimental tests of asymptotic freedom. *Prog. Part. Nucl. Phys.*, 58:351–386, 2007.

[41] P. Braun-Munzinger, K. Redlich, and J. Stachel. Particle Production in Heavy Ion Collisions, arXiv:nucl-th/0304013, 2003.

[42] P. Braun-Munzinger, J. Stachel, J. P. Wessels, and N. Xu. Thermal and Hadrochemical Equilibration in Nucleus-Nucleus Collisions at the SPS. *Phys. Lett. B*, 365:1, 1996.

[43] P. Braun-Munzinger, D. Magestro, K. Redlich, and J. Stachel. Hadron production in Au-Au collisions at RHIC. *Phys. Lett.*, B518:41–46, 2001.

[44] C. Tsallis. Possible Generalization of Boltzmann-Gibbs Statistics. *Journal of Statistical Physics*, 52:479, 1988.

[45] I. Arsene et al. Centrality dependent particle production at y = 0 and y ≈ 1 in Au-Au collisions at $\sqrt{s_{NN}}$ = 200 `GeV`. *Phys.Rev.*, C72:014908, 2005.

[46] R. Hagedorn and J. Ranft. Inclusive single particle spectra and the strong thermodynamic bootstrap solution. *Nucl. Phys.*, B48:157–190, 1972.

[47] N. Cabibbo and G. Parisi. Exponential Hadronic Spectrum and Quark Liberation. *Phys. Lett.*, B59:67–69, 1975.

[48] G. Veneziano. Construction of a crossing-simmetric, Regge-behaved amplitude for linearly rising trajectories. *Il Nuovo Cimento A*, 57, 1968.

[49] K. Bardakci and S. Mandelstam. Analytic solution of the linear-trajectory bootstrap. *Phys. Rev.*, 184:1640–1644, 1969.

[50] S. Fubini and G. Veneziano. Level structure of dual-resonance models. *Nuovo Cim.*, A64:811–840, 1969.

[51] Kerson Huang and Steven Weinberg. Ultimate Temperature and the Early Universe. *Phys. Rev. Lett.*, 25(13):895–897, Sep 1970.

[52] H. Satz. Critical behavior of hadronic matter: Critical-point exponents. *Phys. Rev. D*, 19(6):1912–1916, Mar 1979.

[53] Philippe Blanchard, Santo Fortunato, and Helmut Satz. The Hagedorn temperature and partition thermodynamics. *Eur. Phys. J.*, C34:361–366, 2004.

[54] R. V. Gavai and A. Gocksch. Velocity of sound in SU(3) lattice gauge theory. *Phys. Rev. D*, 33(2):614–616, Jan 1986.

[55] K. Redlich and H. Satz. Critical behavior near deconfinement. *Phys. Rev. D*, 33(12):3747–3752, Jun 1986.

[56] F. Karsch, E. Laermann, and A. Peikert. The pressure in 2, 2+1 and 3 flavour QCD. *Phys. Lett.*, B478:447–455, 2000.

[57] C. Caso et al. Review of particle physics. *Eur. Phys. J.*, C3:1–794, 1998.

[58] Wojciech Broniowski. Distinct Hagedorn temperatures from particle spectra: A higher one for mesons, a lower one for baryons. *Presented at Miniworkshop Bled 2000: Few Quark Problems, Bled, Slovenia. Published in Bled 2000, Few-quark problems 3*, 2000.

[59] Mikolaj Chojnacki, Wojciech Florkowski, and Tamas Csorgo. On the formation of Hubble flow in Little Bangs. *Phys. Rev.*, C71:044902, 2005.

[60] Mikolaj Chojnacki and Wojciech Florkowski. Temperature dependence of sound velocity and hydrodynamics of ultra-relativistic heavy-ion collisions. *Acta Phys. Polon.*, B38:3249–3262, 2007.

[61] Wojciech Broniowski and Wojciech Florkowski. Different Hagedorn temperatures for mesons and baryons from experimental mass spectra, compound hadrons, and combinatorial saturation. *Phys.Lett.B*, 490:223, 2000.

[62] A. Andronic, P. Braun-Munzinger, and J. Stachel. Thermal hadron production in relativistic nuclear collisions: The hadron mass spectrum, the horn, and the QCD phase transition. *Physics Letters B*, 673(2):142 – 145, 2009.

[63] A. Andronic, P. Braun-Munzinger, and J. Stachel. Hadron production in central nucleus nucleus collisions at chemical freeze-out. *Nucl. Phys.*, A772:167–199, 2006.

[64] F. Becattini, J. Manninen, and M. Gaździcki. Energy and system size dependence of chemical freeze-out in relativistic nuclear collisions. *Phys. Rev. C*, 73(4):044905, Apr 2006.

[65] J. Noronha-Hostler, H. Ahmad, J. Noronha, and C. Greiner. Particle ratios as a probe of the QCD critical temperature. *Phys. Rev. C*, 82(2):024913, Aug 2010.

[66] J. Noronha-Hostler, M. Beitel, C. Greiner, and I. Shovkovy. Dynamics of chemical equilibrium of hadronic matter close to T_c. *Phys. Rev. C*, 81(5):054909, May 2010.

[67] P. Castorina, K. Redlich, and H. Satz. The phase diagram of hadronic matter. *The European Physical Journal C - Particles and Fields*, 59:67–73, 2009. 10.1140/epjc/s10052-008-0795-z.

[68] Jacquelyn Noronha-Hostler, Jorge Noronha, and Carsten Greiner. Transport Coefficients of Hadronic Matter Near *Tc*. *Phys. Rev. Lett.*, 103(17):172302, Oct 2009.

[69] P. Castorina, J. Cleymans, D. E. Miller, and H. Satz. The Speed of Sound in Hadronic Matter. *Eur. Phys. J.*, C66:207–213, 2010.

[70] Roger Dashen, Shang-keng Ma, and Herbert J. Bernstein. s-matrix formulation of statistical mechanics. *Phys. Rev.*, 187:345–370, Nov 1969.

[71] F. Karsch, K. Redlich, and A. Tawfik. Hadron resonance mass spectrum and lattice QCD thermodynamics. *Eur. Phys. J.*, C29:549–556, 2003.

[72] F. Karsch, K. Redlich, and A. Tawfik. Thermodynamics at non-zero baryon number density: A comparison of lattice and hadron resonance gas model calculations. *Phys. Lett.*, B571:67–74, 2003.

[73] A. Tawfik. The QCD phase diagram: A comparison of lattice and hadron resonance gas model calculations. *Phys. Rev.*, D71:054502, 2005.

[74] L. D. Landau and E. M. Lifshitz. *Course Of Theoretical Physics - Volume VI - Fluid Mechanics.* Butterworth-Heinemann, 1987.

[75] Azwinndini Muronga. Relativistic Dynamics of Non-ideal Fluids: Viscous and heat-conducting fluids. I. General Aspects and 3+1 Formulation for Nuclear Collisions. *Phys.Rev.*, C76:014909, 2007.

[76] G.J. Van Wylen and R.E. Sonntag. *Fundamentals of Classical Thermodynamics.* John Wiley and Sons, Inc., New York. Library of Congress Calatog Card Number: 65-19470, 1965. Read more: http://www.answers.com/topic/isentropic-process.

[77] N. Bilic, J. Cleymans, E. Suhonen, and D. W. von Oertzen. Indications for a detonating quark - gluon plasma. *Phys. Lett.*, B311:266–272, 1993.

[78] Szabolcs Borsanyi et al. The QCD equation of state with dynamical quarks. *JHEP*, 11:077, 2010.

[79] Wolfgang Soldner. Chiral Aspects of Improved Staggered Fermions with 2+1- Flavors from the HotQCD Collaboration. *PoS*, LATTICE2010:215, 2010.

[80] P. Braun-Munzinger and J. Stachel. Probing the Phase Boundary between Hadronic Matter and the Quark-Gluon-Plasma in Relativistic Heavy Ion Collisions. *Nucl.Phys.A*, 606:320, 1996.

[81] Dariusz Prorok and Ludwik Turko. The sound velocity in an equilibrium hadron gas. eprint arXiv:hep-ph/0101220, 2001.

[82] Szabolcs Borsanyi et al. Transition temperature and the equation of state from lattice QCD, Wuppertal-Budapest results. *Acta Phys.Polon.Supp.*, 4:593–602, 2011.

[83] J. Adams *et al.* [STAR Collaboration]. Kaon Production and Kaon to Pion Ratio in Au-Au Collisions at $\sqrt{s_{NN}} = 130\texttt{GeV}$. *Phys. Lett. B*, 595:143, 2004.

[84] J. Adams *et al.* [STAR Collaboration]. Rapidity and centrality dependence of proton and antiproton production from Au-Au collisions at $\sqrt{s_{NN}} = 130\texttt{GeV}$. *Phys. Rev. C*, 70(4):041901, Oct 2004.

[85] J. Adams *et al.* [STAR Collaboration]. Identified Particle Distributions in p-p and Au-Au Collisions at $\sqrt{s_{NN}} = 200$ GeV. *Phys. Rev. Lett.*, 92(11):112301, Mar 2004.

[86] J. Adams *et al.* [STAR Collaboration]. Scaling Properties of Hyperon Production in Au-Au Collisions at $\sqrt{s_{NN}} = 200$ GeV. *Phys. Rev. Lett.*, 98(6):062301, Feb 2007.

[87] R. Brun and F. Rademakers. ROOT-An Object Oriented Data Analysis Framework, ROOT web page, `http://root.cern.ch/`. *Nucl. Inst. & Meth. in Phys. Res. A*, 389:81, 1997.

[88] W. Broniowski W. Florkowski J. Letessier G. Torrieri, S. Steinke and J. Rafelski. SHARE: Statistical hadronization with resonances. *Comput. Phys. Commun.*, 167, 2005.

[89] Adam Kisiel, Tomasz Taluc, Wojciech Broniowski, and Wojciech Florkowski. Therminator: Thermal heavy-Ion generator. *Comput. Phys. Commun.*, 174:669, 2006.

[90] J. Cleymans and K. Redlich. Unified description of freeze-out parameters in relativistic heavy ion collisions. *Phys. Rev. Lett.*, 81:5284–5286, 1998.

[91] P Braun-Munzinger and J Stachel. Particle ratios, equilibration and the QCD phase boundary. *Journal of Physics G: Nuclear and Particle Physics*, 28(7):1971, 2002.

[92] A Tawfik. Influence of strange quarks on the QCD phase diagram and chemical freeze-out. *Journal of Physics G: Nuclear and Particle Physics*, 31(6):S1105, 2005.

[93] J. Cleymans, M. Stankiewicz, P. Steinberg, and S. Wheaton. The origin of the difference between multiplicities in e^+e^- annihilation and heavy ion collisions. eprint:nucl-th/0506027, 2005.

[94] A. Tawfik. On the conditions driving the chemical freeze-out. *Europhys. Lett.*, 75:420, 2006.

[95] V. Magas and H. Satz. Conditions for confinement and freeze-out. *The European Physical Journal C - Particles and Fields*, 32:115–119, 2003. 10.1140/epjc/s2003-01375-1.

[96] K. Redlich, J. Cleymans, H. Oeschler, and A. Tounsi. Particle production and equilibration in heavy ion collisions. *Acta Phys. Polon.*, B33:1609–1628, 2002.

[97] F. Becattini, J. Cleymans, A. Keranen, E. Suhonen, and K. Redlich. Features of particle multiplicities and strangeness production in central heavy ion collisions between 1.7A and 158A `GeV`/c. *Phys.Rev.C*, 64:024901, 2001.

[98] P. Braun-Munzinger, I. Heppe, and J. Stachel. Chemical Equilibration in Pb-Pb Collisions at the SPS. *Phys.Lett.B*, 465:15, 1999.

[99] P. Braun-Munzinger, J. Stachel, J. P. Wessels, and N. Xu. Thermal Equilibration and Expansion in Nucleus-Nucleus Collision at the AGS. *Phys.Lett.B*, 344:43, 1995.

[100] Wojciech Broniowski and Wojciech Florkowski. Strange particle production at RHIC in a single-freeze-out model. *Phys. Rev. C*, 65:064905, 2002.

[101] M. Kaneta and N. Xu. On chemical equilibrium in high-energy heavy-ion collisions. *J. Phys. G: Nucl. Part. Phys.*, 27:589, 2001.

[102] M. Kaneta (for the NA44 Collaboration). Particle ratios from central Pb-Pb collisions at the CERN SPS. *J. Phys. G:Nucl. Part. Phys.*, 23:1865, 1997.

[103] Jean Letessier, Johann Rafelski, and Ahmed Tounsi. Gluon production, cooling and entropy in nuclear collisions. *Phys.Rev.C*, 50:406, 1994.

[104] F. Becattini, J. Manninen, and M. Gazdzicki. Energy and system size dependence of chemical freeze-out in relativistic nuclear collisions. *Phys.Rev.*, C73:044905, 2006.

[105] J. Cleymans, B. Kampfer, M. Kaneta, S. Wheaton, and N. Xu. Centrality dependence of thermal parameters deduced from hadron multiplicities in Au-Au collisions at $\sqrt{s_{NN}} = 130$ GeV. *Phys.Rev.C*, 71:054901, 2005.

[106] Nu Xu and Masashi Kaneta. Hadron freeze-out conditions in high energy nuclear collisions. *Nucl. Phys. A*, 698:306, 2002.

[107] B. I. Abelev *et al.* [STAR Collaboration]. Partonic Flow and ϕ-Meson Production in Au-Au Collisions at $\sqrt{s_{NN}} = 200$ GeV. *Phys. Rev. Lett.*, 99(11):112301, Sep 2007.

[108] J. H. Chen. System size and energy dependence of ϕ meson production at RHIC. *J. Phys. G*, 35:104053, 2008.

[109] A. Andronic, P. Braun-Munzinger, and J. Stachel. Thermal hadron production in relativistic nuclear collisions: The Hadron mass spectrum, the horn, and the QCD phase transition. *Phys.Lett.*, B673:142–145, 2009.

[110] C. Tsallis. Nonextensive Statistics: Theoretical, experimental and computational Evidences and connection. *Brazilian Journal of Physics*, 29:479, 1999.

[111] F. H. Jackson. Generalization of the Differential Operative Symbol with an Extended Form of Booles Equation , Messenger of Mathematics. *Mess. Maths. 38*, 57:479, 1909.

[112] Yuko Okamoto (Eds.) Sumiyoshi Abe. *Nonextensive Statistical Mechanics and Its Applications (Lecture Notes in Physics).* Springer, 2001.

[113] J. M. Conroy, H. G. Miller, and A. R. Plastino. Thermodynamic Consistency of the q-Deformed Fermi-Dirac Distribution in Nonextensive Thermostatics. *Phys.Lett.*, A374:4581–4584, 2010.

[114] F. Buyukkilic and D. Demirhan. A fractal approach to entropy and distribution functions. *Phys.Lett.*, A181:24, 1993.

[115] F. Pennini, A. Plastino, and A. R. Plastino. Tsallis entropy and quantal distribution functions. *Physics Letters A*, 208(4-6):309 – 314, 1995.

[116] A. M. Teweldeberhan, A. R. Plastino, and H. G. Miller. On the cut-off prescriptions with power-law generalized thermostatistics. *Phys.Lett.*, A343:71, 2004.

[117] C. M. Justin and H. G. Miller. Color Superconductivity and Tsallis Statistics. *Phys.Rev.*, D78:054010, 2008.

[118] Jincan Chen, Zhipeng Zhang, Guozhen Su, Lixuan Chen, and Yaogen Shu. q-generalized bose-einstein condensation based on tsallis entropy. *Physics Letters A*, 300(1):65 – 70, 2002.

[119] J. Cleymans, G. Hamar, P. Levai, and S. Wheaton. Near-thermal equilibrium with Tsallis distributions in heavy ion collisions. *J.Phys.G*, G36:064018, 2009.

[120] C. Tsallis. Possible Generalization of Boltzmann-Gibbs Statistics. *J.Statist.Phys.*, 52:479–487, 1988.

[121] C. Tsallis, R. S. Mendes, and A. R. Plastino. The role of constraints within generalized nonextensive statistics . *Physica*, A261:534, 1998.

[122] T.S. Biro and G. Purcsel. Non-extensive Boltzmann equation and hadronization. *Phys.Rev.Lett.*, 95:162302, 2005.

[123] A.M. Teweldeberhan, H.G. Miller, and R. Tegen. Generalized statistics and the formation a quark gluon plasma. *Int.J.Mod.Phys.*, E12:395–406, 2003.

[124] A.R. Plastino, A. Plastino, H.G. Miller, and H. Uys. Foundations of Nonextensive Statistical Mechanics and its Cosmological Applications. *Astrophys.Space Sci.*, 290:275, 2004.

[125] Ch. G. van Weert S. R. de Groot, W. A. van Leeuwen. *Relativistic kinetic theory : principles and applications.* Elsevier North-Holland.

[126] G. Wilk and Z. Wlodarczyk. On the interpretation of nonextensive parameter q in Tsallis statistics and Levy distributions. *Phys.Rev.Lett.*, 84:2770, 2000.

[127] F.I.M. Pereira, R. Silva, and J.S. Alcaniz. Nonextensive effects on the relativistic nuclear equation of state. *Phys.Rev.*, C76:015201, 2007.

[128] F.I.M. Pereira, R. Silva, and J.S. Alcaniz. Nonextensive effects on the phase structure of QHD. *Phys.Lett.*, A373:4214–4218, 2009.

[129] W.M. Alberico, A. Lavagno, and P. Quarati. Nonextensive statistics, fluctuations and correlations in high-energy nuclear collisions. *Eur.Phys.J.*, C12:499–506, 2000.

[130] A. Lavagno. Relativistic nonextensive thermodynamics. *Phys.Lett.*, A301:13, 2002.

[131] W. M. Alberico, P. Czerski, A. Lavagno, M. Nardi, V. Soma', Henryk Niewodniczanski, and Ricerche E. Fermi. Signals of non-extensive statistical mechanics in high energy nuclear collisions. *Physica A-statistical Mechanics and Its Applications*, 387:467–475, 2008.

[132] W.M. Alberico, A. Lavagno, and P. Quarati. Nonextensive statistics effects in quark gluon plasma and in relativistic heavy ion collisions. *Nucl.Phys.*, A680:94–97, 2000.

[133] T. Anticic et al. Proton – Lambda Correlations in Central Pb-Pb Collisions at $\sqrt{s_{NN}} = 17.3\ \mathtt{GeV}$. *Phys. Rev.*, C83:054906, 2011.

[134] A. Andronic, P. Braun-Munzinger, and J. Stachel. Hadron production in central nucleus nucleus collisions at chemical freeze-out. *Nucl. Phys.*, A772:167–199, 2006.

[135] M. Abramowitz and I. A. (Eds.) Stegun. *Handbook of Mathematical Functions with Formulas, Graphs, and Mathematical Tables.* New York: Dover Books on Mathematics, 1972.

Acknowledgments

First of all, I would like to thank the Almighty God who brought me into this world. Secondly, I would like to truly express my deepest gratitude to my supervisor Prof. Jean Cleymans for his non-stop guidance, exposure to a blend of numerous areas in physics, assistance and follow up during my thesis work. I really admire him for his friendly approach with inmeasurable and valuable contribution throughout the whole period of the research work.

I am very pleased to thank the DAAD-AIMS PhD scholarship and the National Institute of Theoretical Physics (NiTheP) for their financial support.

It is my heartfelt desire to address with enormous pleasure to Masimba Paradza, Tshilidzi Thovhogi, Fhumulani Nemulodi and Preshin Moodley for their discussions, ideas and for proof reading my thesis.

I am also grateful to Prof. Azwinndini Muronga, Prof. Andre Peshier and Dr. Spencer Wheaton for their support on the discussions during my study and their constructive criticisms and encouragement.

Last but not least, my family should take their share of my boundless gratitude. I have special heart for my wife and my daughter who were patient with me during the busy time and encouraged me throughout the thesis work. Finally, thanks to all UCT Physics department staff and fellow post graduate students who have shown me the spirit of friendship, support and encouragement during my tenure in the department.

Finally, I would like to thank the external examiners for the valuable contributions, comments, suggestions and questions in my PhD thesis.